TYNER

SERI/TR-252-2884
DE87001117

October 1986

Direct Absorption Receiver Experiments and Concept Feasibility

Mark S. Bohn
H. J. Green
George Yeagle
James Siebarth
Solar Energy Research Institute

O. David Asbell
C. Thomas Brown
Georgia Tech Research Institute

SERI

Direct Absorption Receiver Experiments and Concept Feasibility

Mark S. Bohn
H. J. Green
George Yeagle
James Siebarth
Solar Energy Research Institute

O. David Asbell
C. Thomas Brown
Georgia Tech Research Institute

October 1986

PREFACE

The research and development described in this document was conducted within the U.S. Department of Energy's Solar Thermal Technology Program. The goal of this program is to advance the engineering and scientific understanding of solar thermal technology and to establish the technology base from which private industry can develop solar thermal power production options for introduction into the competitive energy market.

Solar thermal technology concentrates the solar flux using tracking mirrors or lenses onto a receiver where the solar energy is absorbed as heat and converted into electricity or incorporated into products as process heat. The two primary solar thermal technologies, central receivers and distributed receivers, employ various point- and line-focus optics to concentrate sunlight. Current central receiver systems use fields of heliostats (two-axis tracking mirrors) to focus the sun's radiant energy onto a single, tower-mounted receiver. Point-focus concentrators up to 17 meters in diameter track the sun in two axes and use parabolic dish mirrors or Fresnel lenses to focus radiant energy onto a receiver. Troughs and bowls are line-focus tracking reflectors that concentrate sunlight onto receiver tubes along their focal lines. Concentrating collector modules can be used alone or in a multimodule system. The concentrated radiant energy absorbed by the solar thermal receiver is transported to the conversion process by a circulating working fluid. Receiver temperatures range from $100^{\circ}C$ in low-temperature troughs to over $1500^{\circ}C$ in dish and central receiver systems.
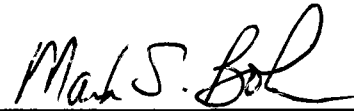
The Solar Thermal Technology Program is directing efforts to advance and improve each system concept through solar thermal materials, components, and subsystems research and development and by testing and evaluation. These efforts are carried out with the technical direction of DOE and its network of field laboratories that works with private industry. Together they have established a comprehensive, goal-directed program to improve performance and provide technically proven options for eventual incorporation into the Nation's energy supply.

To successfully contribute to an adequate energy supply at reasonable cost, solar thermal energy must be economically competitive with a variety of other energy sources. The Solar Thermal Technology Program has developed components and system-level performance targets as quantitative program goals. These targets are used in planning research and development activities, measuring progress, assessing alternative technology options, and developing optimal components. These targets will be pursued vigorously to ensure a successful program.

Research described in this report addresses a novel concept for the tower-mounted receiver in a central receiver system. The concept involves directly exposing a falling molten-salt film to the flux from the heliostat field. Since the molten-salt working fluid is not contained in complicated

tube manifolds, the receiver design should be simpler than a conventional tube-type receiver, for example, resulting in a lower cost and a more reliable receiver. Prior to this work, very little experimental data were available that would allow one to determine if this concept is feasible.

We wish to acknowledge the careful reviews of this report by Tibor Buna, SPECO, Inc.; John Holmes, Sandia National Laboratories; Reiner Köhne, DFVLR; Ralph Seban, University of California; Craig Tyner, Sandia National Laboratories; Raymond Viskanta, Purdue University; and S. F. Wu, Foster Wheeler, S. D. C.

_____
Mark S. Bohn

Approved for

SOLAR ENERGY RESEARCH INSTITUTE

_____
David H. Johnson, Manager
Thermal Sciences Research Branch

_____
L. J. Shannon, Director
Solar Heat Research Division

SUMMARY

Objective

The objective of this work is to experimentally determine the technical feasibility of the direct absorption receiver (DAR) concept.

Discussion

Direct absorption receivers can significantly reduce the cost of delivered solar thermal energy. However, before this work very little experimental data were available that would enable one to determine if the concept is feasible. Earlier work on the DA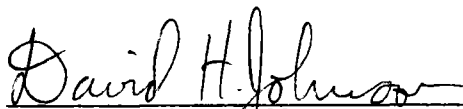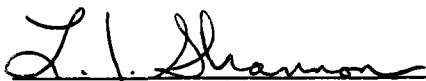R concept at SERI was aimed at assessing technical feasibility based on information available in the existing literature. Although these efforts proved fruitful, they pointed out certain deficiencies in the existing literature that called for experimental data.

Additional work at SERI involved developing an analytical model that could predict the heat transfer behavior of a liquid-working-fluid receiver. This model can predict absorber-plate temperatures, thermal efficiency, effect of working fluid dopants, etc., but required experimental data for validation.

This report describes an experimental program carried out by SERI using the concentrated solar flux at the Advanced Components Test Facility at the Georgia Tech Research Institute in Atlanta, Ga. Included are a description of the tests, the data obtained, the analysis of the data and comparisons to analytical predictions, and an assessment of the technical feasibility of the DAR concept.

Conclusions

Data were gathered that support analysis of the film stability at high and low flow rates, thermal efficiency, and heat transfer (between the salt and the absorber plate). Comparisons with the analytical predictions of thermal efficiency and heat transfer were favorable and suggest: thermal efficiency in the range 80% to 90%, depending on operating temperature and flux, and heat transfer coefficients (for the undoped salt operating in the laminar flow regime) of about 3000 W/m^2 $^\circ$C. We did not find any flow instabilities at high flow rates (up to about 14.9 m^2/h, flow rate per unit width); however, we did find a dry-out problem for flow rates below about 8.9 m^2/h, which is subject to further experimental work but is most likely attributable to experimental artifacts. Based on the analysis of all available information, we judged the DAR concept technically feasible.

TABLE OF CONTENTS

TABLE OF CONTENTS (Concluded)

LIST OF FIGURES

LIST OF FIGURES (Concluded)

LIST OF TABLES

NOMENCLATURE

a,b	constants in salt pump calibration curve
A, A_{active}	area of absorber wetted by salt (m^2)
C_s	salt specific heat (W s/kg ^oC)
C_v	discharge coefficient
g	acceleration of gravity (m/s^2)
H,h	height of liquid above weir (m)
h_{as}	convective heat transfer coefficient at air/salt interface
h_{fg}	heat of vaporization of salt (W s/kg)
h(x)	local absorber-to-salt heat transfer coefficient (W/m^2 ^oC)
k	thermal conductivity of salt (W/m ^oC)
L	length of absorber exposed to flux (m)
$\dot{m}_s$	mass flow rate of salt (kg/s)
PS	pump speed (%)
Pr	Prandtl number
Q	volumetric flow rate of salt (m^3/s)
$\dot{Q}$	heat input to absorber (W)
q	average total flux incident on absorber (W/m^2)
q(x)	local flux on absorber (W/m^2)
q_{cu}	flux indicated by transducer CU (W/m^2)
q_{in}	total flux incident on absorber (W/m^2)
q_{IR}	contribution of infrared wavelengths ($>2\mu$) to flux incident on absorber (W/m^2)
$q_{rake,cu}$	average of all six flux transducers when rake is at height of transducer cu
q_w	wall heat flux (W/m^2)
Re	salt film Reynolds number = Γ/μ, or $4\Gamma/\mu$
R	air-to-salt density ratio
T	temperature (^oC)
t	time (s)
T_a	ambient temperature
T_s	average salt temperature on the absorber (^oC)
T_{so}	absorber salt outlet temperature (^oC)
T_{si}	absorber salt inlet temperature (^oC)
$T_s(x)$	temperature at a given longitudinal location on absorber (^oC)
$T_a(x)$	local absorber temperature (^oC)

NOMENCLATURE (Concluded)

U	ratio of air velocity to salt velocity
W	width of absorber (m)
x	dimensionless longitudinal distance from top of absorber
x_o	distance from inlet where temperature profile is fully developed

Greek

α	solar absorptance
Γ	mass flow per unit width, $\dot{m}_s/W$ (kg/m s)
ΔT_s	$T_{si} - T_{so}$ ($^{\circ}$C)
δ	film thickness (m)
δ_{min}	critical film thickness
δ_o	inlet film thickness $(3\Gamma\mu/\rho^2 g \sin \theta)^{1/3}$
ΔT_p	$T_a(x) - T_s(x)$ ($^{\circ}$C)
ΔT_f	temperature difference from absorber to air/salt interface ($^{\circ}$C)
ϵ	infrared emittance
η	thermal efficiency (Eq. 6-2)
θ	angle of absorber from horizontal (deg)
θ_f, θ_k	normalized temperatures (Eq. 6-5)
θ_o	contact angle of salt on absorber (deg)
μ	dynamic viscosity of salt (kg/m s)
ν	kinematic viscosity of salt (m^2/s)
ρ	density of liquid salt (kg/m^3)
ρ_s	solar wavelength reflectance at the air/salt interface
ρ	density of vapor from heated salt (kg/m^3)
σ	surface tension (N/m)
τ	time constant for cavity cool-down (s)

CONVERSION TABLE

Measurements	International System of Units (SI)		English Units
Flow rate	$0.227 \; m^3/h$	=	1 gal/min
	$1.0 \; m^3/h$	=	4.40 gal/min
Flow per unit width	$0.75 \; m^2/h$	=	1 gal/min ft
	$1.0 \; m^2/h$	=	1.33 gal/min ft
Temperature	^oC	=	$(^oF - 32)0.55$
	$^oC \times 1.8 + 32$	=	^oF
Pressure	6891 Pa	=	1 psi
	101,300 Pa	=	1 atm
Viscosity	1.49 kg/m s	=	1.00 lbm/ft s
	1 kg/m s	=	0.671 lbm/ft s
Density	$1 \; kg/m^3$	=	$0.0623 \; lbm/ft^3$
	$16.05 \; kg/m^3$	=	$1.0 \; lbm/ft^3$
Specific heat	1 W s/kg K	=	$2.388 \times 10^{-4} \; Btu/lbm \; ^oF$
	4187 W s/kg K	=	$1 \; Btu/lbm \; ^oF$
Thermal conductivity	1 W/m K	=	$0.5777 \; Btu/h \; ft \; ^oF$
	1.731 W/m K	=	$1.00 \; Btu/h \; ft \; ^oF$
Length	1 mm	=	0.03937 in.
	25.4 mm	=	1 in.

SERI☀

1.0 INTRODUCTION

The concept of a direct absorption receiver (DAR) is based on the working fluid absorbing concentrated solar flux without a containment surface separating them. In practice the working fluid flows by gravity in a film or a curtain in a cavity (or possibly external) receiver. In a conventional receiver the working fluid is contained in tubes, and the radiation impinging on the tube's outer surface is absorbed and transferred to the working fluid by conduction through the tube wall.

This DAR arrangement has several potential advantages over a conventional receiver. First, without an intervening tube wall to cause a temperature drop, the working fluid is at the highest temperature in the system. This arrangement reduces materials problems and receiver reradiation losses. Second, the receiver cost could be lower and its reliability could be higher because of its simpler design and reduced thermal stress and cycling problems. Finally, the receiver can tolerate much higher flux levels since the flux is absorbed directly in the working fluid. This results in a smaller and less costly receiver.

In addition to a molten-salt working fluid, researchers have investigated several DAR concepts using solid particles of various sizes (Hunt 1979 and 1983; Hruby and Steele 1985). This report focuses on a system using a falling molten-salt film.

1.1 Background

Brumleve (1974) points out the potential advantages of this concept, develops preliminary cost estimates for a DAR system, and discusses some of the research needs. In 1978, he presented data that showed that if one adds a dopant to a normally transparent salt, very high fluxes can be tolerated. For a 2-mm film thickness exposed to a flux of 6 MW/m^2, the substrate temperature exceeded the salt temperature by less than 3°C. In this case the salt was doped with a 0.1% by weight cobalt oxide suspension.

Wang and Copeland (1984) developed a model for the heat transfer processes in a falling liquid film exposed to incident flux. The model allows one to predict the thermal efficiency of the film, the temperature of the substrate, the distribution of temperature in the salt-film, and the effect of dopants used to darken the salt. The issue of salt-film stability was treated by Wang et al. (June 1985) and Newell et al. (1985, 1986). They covered film stability at both low and high flow rates, formation of dry areas in the film caused by the thermocapillary effect, film thickness correlations, and interaction with airflow.

Systems analysis studies of this concept show some of its potential cost benefits, especially at high flux levels (Lewandowski et al. 1984).

Copeland (forthcoming) describes a conceptual design configuration for a process plant using a direct absorption receiver. His report provides design details and discusses some of the technical issues one must deal with in a commercial application.

1.2 Objective of the Present Research

To further establish the merits of the DAR concept, a systematic experimental effort was needed that would provide data for substantiating the heat transfer and film stability models and that would address the technical feasibility of DAR concepts under actual solar flux. This report describes such an effort.

1

The experimental effort in this report provides data that could be compared with existing heat transfer models, particularly those developed by Wang and Copeland (1984). These data include thermal efficiency of the salt film and the heat transfer coefficient between the salt film and the substrate under a wide range of operating conditions. This effort also provides data on the stability of the salt film over a wide range of flow rates in the presence of a wide range of solar flux levels. It also provides operational experience with the receiver under solar flux that would lead to design/operation criteria for DAR development.

If these goals are realized, one could then use the heat transfer model to predict receiver performance under conditions not easily achievable experimentally (e.g., high flux), predict the performance of a commercial receiver and thus its economic feasibility, and determine potential materials problems caused by excessive temperatures.

To test the concept under solar conditions, we fabricated and tested a small-scale absorber panel (152-mm by 610-mm active area, see Figure 2-3) inclined at 5 deg from vertical (85 deg from horizontal) with salt inlet temperatures of 450°-700°C without solar flux. These preliminary tests allowed us to check the behavior of the salt flow on the plate, to make film-thickness measurements, and to observe low-flow film stability. For these tests the plate was heated with electrical resistance heaters only.

We then designed and fabricated a loop to test a wide range of flow rates and salt temperatures with solar flux. To provide solar flux the test loop was designed to interface with the focal zone of the Advanced Components Test Facility (ACTF) of the Georgia Tech Research Institute (GTRI) in Atlanta, Ga. The loop was tested there from August to November 1985. We originally planned to test with doped salt to provide increased absorption of solar wavelengths; however, excessive complexity and the attendent cost and scheduling impacts led us to confine this initial series of tests to clear salt.

This report describes in Section 2.0 the experimental apparatus, including the absorber panel, test loop, flux redirector/cavity receiver, and instrumentation and controls. Section 3.0 describes the ACTF. Section 4.0 describes the first series of tests carried out at the ACTF, the ground tests. These tests provided system checkout/calibration before the test loop was placed on the tower. Sections 5.0 and 6.0 discuss the actual tower tests, which used solar flux, and present the results. In Section 7.0 we present conclusions concerning concept feasibility and recommend future research and development. Appendices include background test information, materials test data, error analyses, and a tabulation of all data from the solar flux tests.

1.3 Research Teams

Solar Energy Research Institute (SERI) staff members fabricated and tested the absorber plate. SERI subcontracted the test loop design to GTRI; that work was completed in the fall of 1984. Industrial Welding and Supply (IWS) of Sterling, Colo., completed the final design and fabricated the test loop. It was completed and transported to the ACTF by IWS in August 1985. ACTF personnel designed and fabricated the cavity/flux redirector and had prime responsibility for the testing. SERI developed the test plan; had prime responsibility for ensuring that the necessary data would be collected to support the goals of the program; and coordinated the work of all parties involved in the design, fabrication, installation, testing, and reporting.

K. Y. Wang (SERI), who originally developed the model and associated computer programs, calculated the DAR heat transfer.

2.0 DESCRIPTION OF THE DAR TEST APPARATUS

The direct absorption receiver test apparatus consists of a molten-salt circulating loop and an absorber panel. The absorber panel is mounted in a cavity lined with highly reflective slip-cast fused silica (see Appendix D for optical properties of the silica). This cavity redirects solar flux from mirrors below the apparatus onto the nearly vertical absorber panel. The apparatus is mounted on a skid to facilitate transportation and make it easier to place on the ACTF tower for testing.

The molten-salt loop supplies molten carbonate salt to the absorber panel at temperatures between 500^0 and 900^0C and at flow rates between 0.15 and 15 m^2/h.* To maintain constant supply temperatures to the absorber panel, the molten salt in Tank 1 can be cooled. The salt flows down the surface of the absorber panel in a thin film, allowing incident solar energy to be directly absorbed. The molten salt is a eutectic of sodium, potassium, and lithium carbonates (see Appendix D for salt property data). The nominal composition of this eutectic is 43.5% Li_2CO_3, 31.5% Na_2CO_3, and 25% K_2CO_3, by mole.

2.1 General Layout and Operation

Figure 2-1 shows a schematic of the molten-salt circulating loop. The loop has two tanks, so two operating modes are available. In the pumped salt flow mode, salt from tank 1 is pumped through flow control valve 1 to the absorber panel and is returned by gravity flow to tank 1. This mode allows continuous operation with salt flow rates between 0.45 and 2.27 m^3/h. The second mode, pressurized salt flow, is a batch operation. Salt is transferred by gravity flow from tank 1 into tank 2 through the drain valve. The drain valve is then closed, and tank 2 is pressurized to a maximum of 123 kPa. One of the two available valves, flow control valve 2 or 3, is then opened, and salt flows to the absorber panel. From the panel the salt drains by gravity into tank 1 where it accumulates. In this mode, salt can be delivered to the absorber panel at flow rates from 0.023 to 0.45 m^3/h. Flow rates between 0.45 and 2.27 m^3/h can also be obtained in this mode for short periods of time to calibrate the salt flowmeter. The rate of salt-level change in tank 2 is determined with a bubbler and provides an absolute measure of volumetric flow rate.

The circulating loop is mounted on a skid 7.3 m long, 3.9 m wide, and 3.2 m high. The total weight is approximately 5000 kg. An additional 680 kg of carbonate salts are required to charge the storage tanks. The skid is constructed primarily of steel I-beams with a work platform constructed of steel grating. Six removable legs of I-beam construction support the skid for ground testing. These legs were removed for the tower testing. OSHA-approved railings and a stairway were added to the skid to facilitate ground testing. Removable rubber-tired dollies make it easy to transport the skid short distances.

The apparatus, mounted on a custom-designed air-bag cushion platform, was transported to GTRI by truck.

---

*Salt flow rate will be expressed in this report as the volumetric flow per unit absorber width. Experimental results in this report are for a 0.152-m absorber width. See p. xiii for conversion factor.
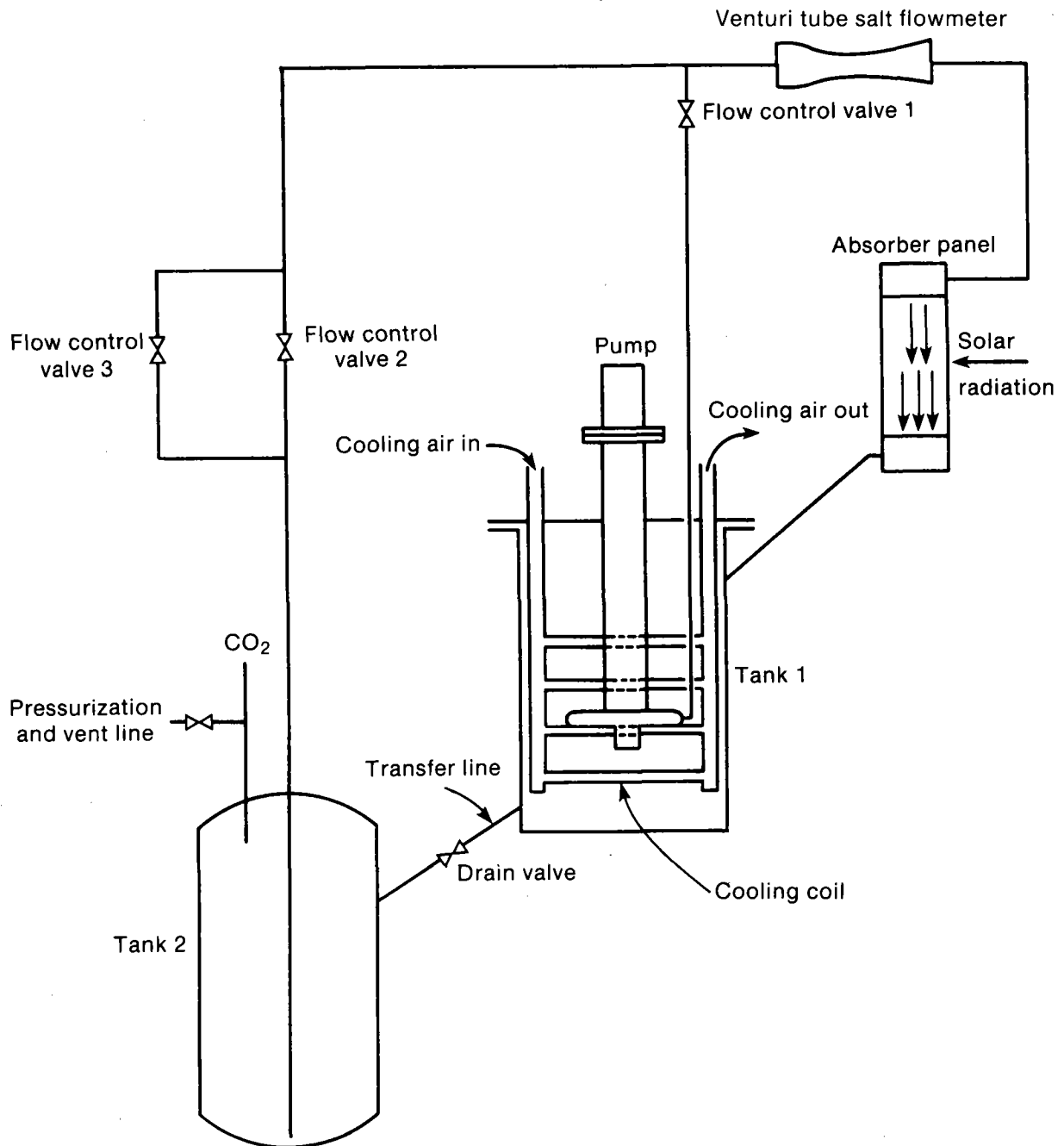
Figure 2-1. 900°C Test Loop

2.2   Salt Tanks, Pump, and Bellows Valves

The apparatus uses two storage tanks constructed of Inconel 600. Tank 1 is a flat-bottomed, nonpressurized tank with a 0.96 cm wall thickness. A cantilevered, molten-salt pump is mounted on this tank along with a cooling coil. Tank 2 is a pressurized vessel with domed ends and is also constructed of 0.96-cm-thick Inconel 600. The maximum tank operating pressure is 114 kPa. The tanks hold approximately 342 L each. Both are solution treated and designed to operate at temperatures up to 900°C.

The molten-salt pump is a centrifugal pump fabricated from Inconel 600 and was manufactured by Lawrence Pumps, Inc.* The cantilever design prevents the process fluid from contacting bearings and allows pumping of molten salt at temperatures up to 900°C. A Louis Allis motor with a speed control unit provides continuously variable speed control from 0 to 900 rpm.

Table 2-1. Bellows Valve and Flow Coefficients

Valve	Discharge Coefficient, C_v
Flow control valve 1	6
Flow control valve 2	10
Flow control valve 3	0.4
Drain valve	10

Four 2.54-cm valves are used in the system; three control flow from the storage tanks, and one, the drain valve, acts as a shut-off valve in the between-tanks transfer line. The valve bodies are constructed of Inconel 600. The stem is sealed with Inconel 600 welded bellows, which have a double-walled design with each wall 0.15 mm thick. Pneumatic actuators provide remote-control valve settings. Table 2-1 shows the valve flow coefficients.

2.3 Trace Heating

All tanks, valves, and pipes use double-sheath, tubular trace heaters designed by Chromolox Corp. The outer sheath is Inconel 600 and the inner sheath is mild steel. The bonnets of each of the bellows valves were individually trace-heated to ensure that the temperature of the bellows was above the salt freezing point. The absorber panel is trace-heated with cartridge heaters manufactured by Watlow. These heaters have a single-layer Inconel 600 sheath. Both heater types were tested at 900°C before the apparatus was fabricated.

The trace heaters on the tanks and the piping to the absorber panel are controlled by PID (proportional-integral-derivative) temperature controllers. The controllers have a remote option that allows trace-heater temperatures to be set from a control panel separate from the skid. Overtemperature sensing units provided a redundant protection against overheating. To avoid excessive thermal cycling of the heating elements, one-second cycle times were used. A rheostat controls the trace heaters on the drain lines from the absorber panel to tank 1 and from tank 1 to tank 2 as well as the valve bonnet trace heaters. Trace heating to the inlet manifold, absorber plate, and outlet manifold was turned off during experiments that involved heat balances on the salt, i.e., experiments to determine efficiency and the heat transfer coefficient.

Tie wires hold the trace heating to the pipes. A stainless steel foil radiation shield covers the trace heating (see Figure 2-2). This shield also prevents insulation from working between the pipe and trace heater. As shown in Figure 2-2, redundant trace heaters were installed in all locations (except the absorber panel) to reduce downtime in the event of a heater failure.

---

*Products mentioned in this report do not constitute an endorsement by SERI.

Cross section   Section through elevation
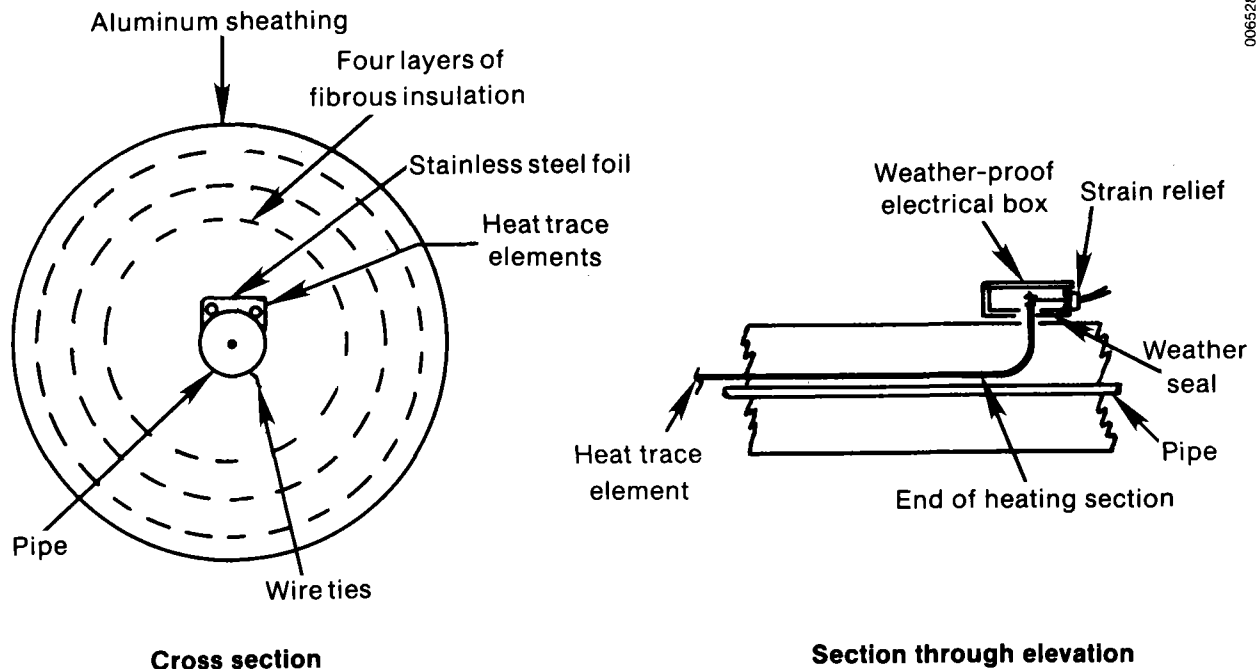
Figure 2-2. Trace Heater Installation

2.4 Absorber Panel Assembly and Cavity

The absorber panel assembly consists of an inlet manifold, the absorber panel, and a drain trough (see Figure 2-3). Its overall dimensions are 114 cm in length and 17.8 cm in width. The assembly is heated with 33 cartridge heaters with a total capacity of 12.5 kW. Salt enters the inlet manifold and flows through a bed of Inconel 600 packing rings, which provide an evenly distributed flow of salt over a weir and onto the absorber panel (see Figure 2-3). The absorber panel has a 15.2-cm-wide channel for the flowing salt film. A 60.1-cm length of this panel is exposed to insolation. The assembly is mounted to the apparatus skid using a space frame truss with a slope 85 deg from horizontal. Special treatment of the absorber edges that enhance containment is discussed in Section 4.2.

The absorber cavity shown in Figure 2-4 and 2-5 consists of an aperture cooling plate (see Figure 2-5), a fused-silica cavity, and a weather shell. The aperture cooling plate has a 152 cm outside diameter with a 66-cm aperture. A 22-mm aluminum cooling coil is supplied with approximately 2 m^3/h of cooling water. The fused-silica cavity housing is 56 cm in diameter and 76 cm high. The weather shell is a rectangular aluminum box housing the absorber assembly and cavity. Sufficient clearance is provided to insulate the absorber assembly and cavity with ceramic fiber insulation. This assembly is discussed in more detail in Section 2.7.

2.5 Balance of System

All salt supply lines leading from the storage tanks to the absorber assembly are 1-in., schedule 40, Inconel 600 pipe. A 1-in. salt transfer line with a shutoff valve connects tanks 1 and 2 to allow the salt to transfer by gravity flow from tank 1 to tank 2. The drain line from the absorber panel to tank 1 is a 2-in., schedule 40 pipe. All lines are
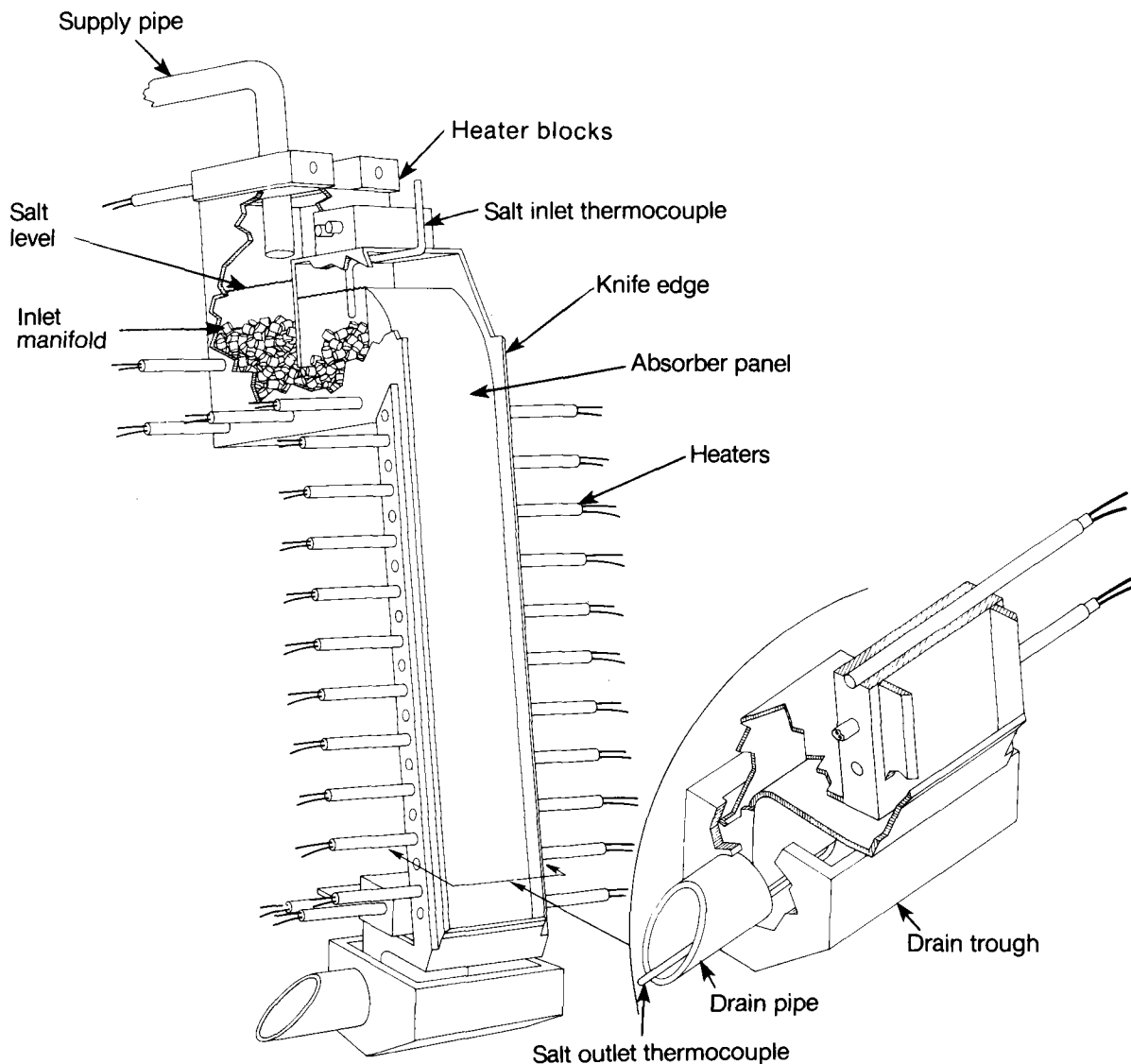
Figure 2-3. Absorber Panel with Manifold Details

heat traced, and all tanks, valves, plumbing lines, and the absorber assembly are insulated with approximately 15 cm of a ceramic fiber insulation. Rigid block insulation was used on both tank bases to support the tanks in their mounting structures.

The cooling coil housed in tank 1 provides up to 41 kW of cooling. Construction is of 0.75-in. schedule 40, Inconel 600 pipe with the headers made from $\frac{1}{2}$-in. schedule 80 pipe. The total surface area available for heat transfer is 14,200 cm^2. Cooling air is supplied at 861 kPa and 0.12 m^3/s from an external compressor. An air-actuated, remote-controlled valve provides manual control of the airflow rate and thus the cooling rate. Exhaust noise levels are moderated with a large automotive-style muffler.
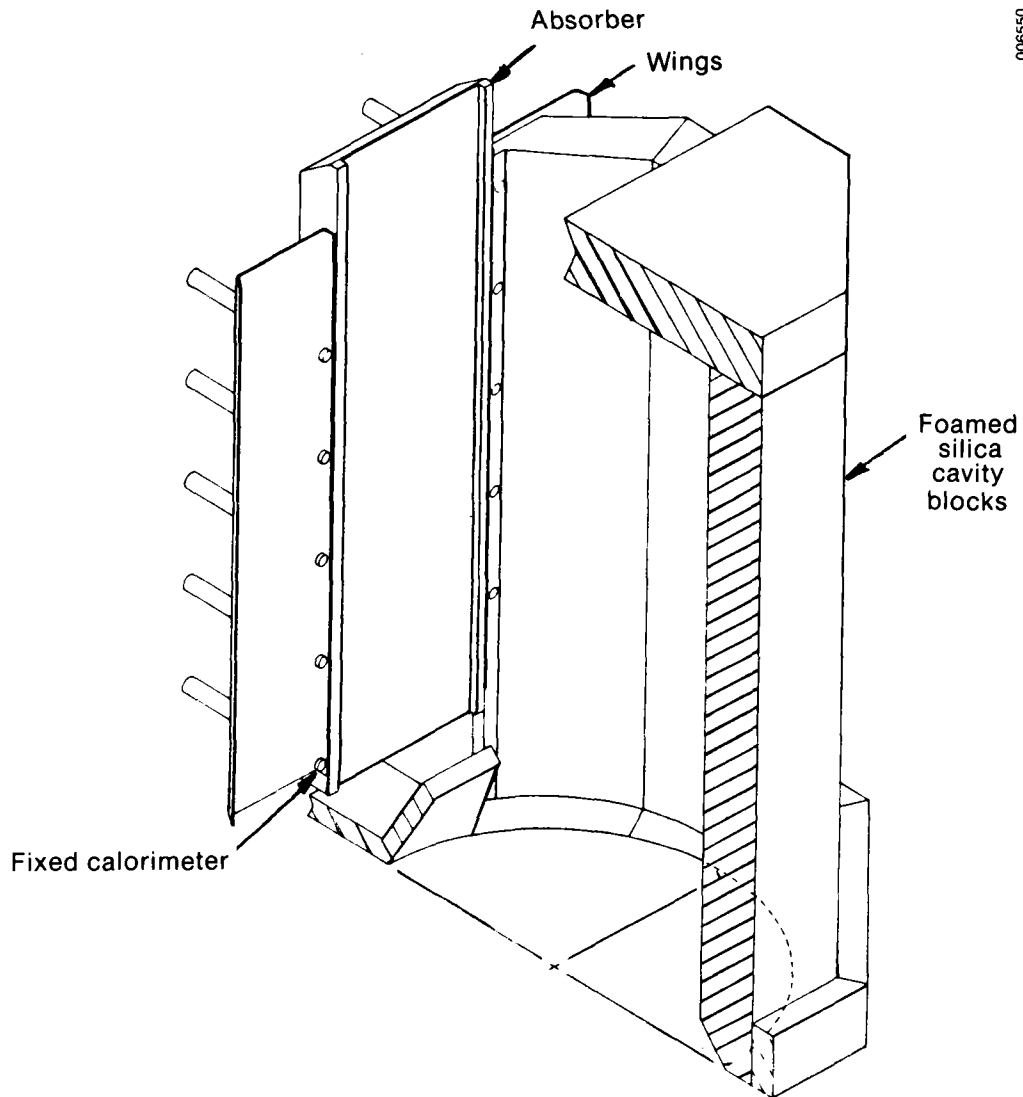
Figure 2-4. DAR Cavity and Flux Redirector

Separate from the main apparatus skid is a CO_2 gas skid. This skid provides gas to bubbler level gauges in tanks 1 and 2, purge gas to tank 1, pressurization gas for tank 2, and purge gas to the absorber cavity. The skid includes five CO_2 bottles, a central manifold, and valves, regulators, and flowmeters as required for these functions.

2.6 Instrumentation and Control

Fifty-two Type K ungrounded thermocouples are used to monitor storage tank, plumbing line, valve body, and absorber assembly temperatures. Fourteen are located in the absorber assembly to monitor salt-inlet temperatures, temperatures along the absorber plate, and salt-outlet temperature. The thermocouples on the absorber panel and their
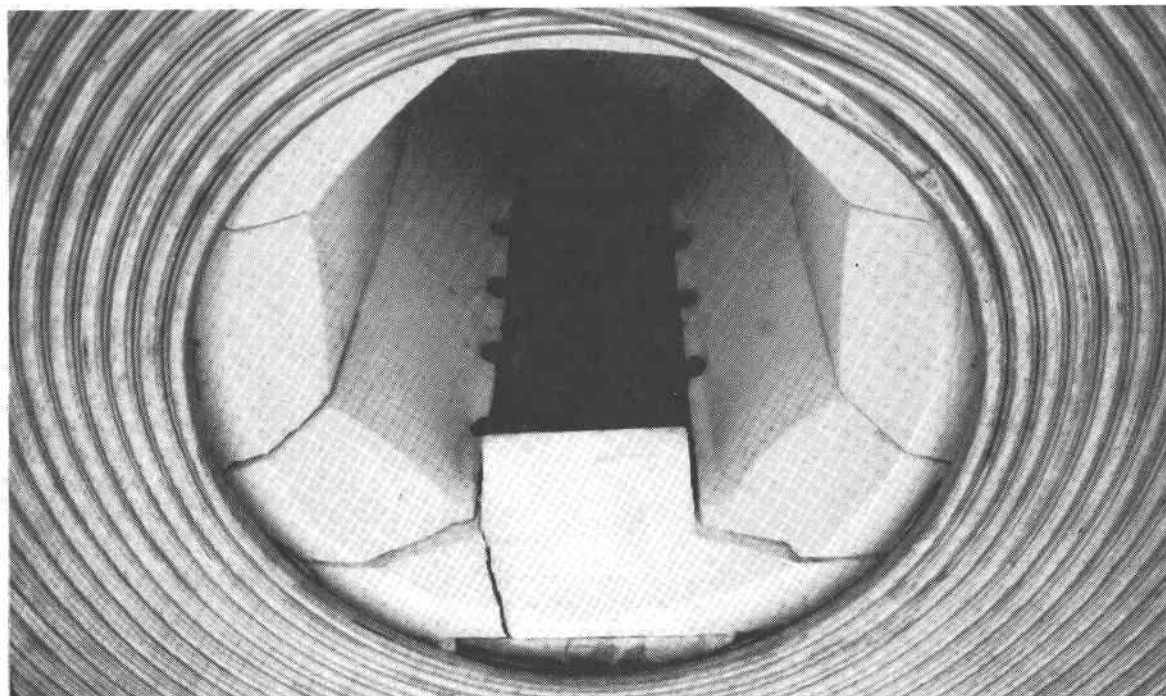
Figure 2-5. Absorber Installed in Cavity

names are shown in Figure 2-6. These thermocouples are inserted into holes drilled from the back of the absorber panel to 3.3 mm below the front surface of the absorber.

Air inlet and outlet temperatures to the tank 1 cooling coil were also monitored. Specially fabricated thermocouples were used for the salt supply and return temperatures to make sure the temperature rise was measured accurately across the absorber. Appendix F discusses these thermocouples further.

Pressure transducers (Validyne model P305D) monitor tank 1 pressure, tank 2 pressure, upstream pressure at the cooling airflow meter, and differential pressure at the cooling airflow meter. A bubbler system (Computer Instruments Corp. Model 7600) provides continuous liquid level measurement in storage tanks 1 and 2. The device measures liquid depth by measuring the pressure required to force a gas with a very low flow rate through a tube. When the end of the tube is situated near the bottom of the tank, changes in liquid level are given as changes in pressure as indicated by the bubbler. The salt-flow rate was to have been measured with a venturi flowmeter. Pressure transducers with pressure diaphragms facing the molten salt (Kaman model KP 1911) were placed to measure upstream and venturi throat pressures. The salt flow rate calibration is discussed further in Section 4.2. Data from all the thermocouples and transducers were recorded by the ACTF data acquisition system.

A control panel provides a remote station (located on the ground during tower tests) to control every major function of the test apparatus. All trace heating except drain lines and valves were controlled from this station. Other control functions available on the control panel include settings for the four molten-salt valves and the cooling airflow control valve, molten-salt pump start and stop buttons and speed setting, and controls for pressurizing and venting tank 2. The face of the control panel displays the
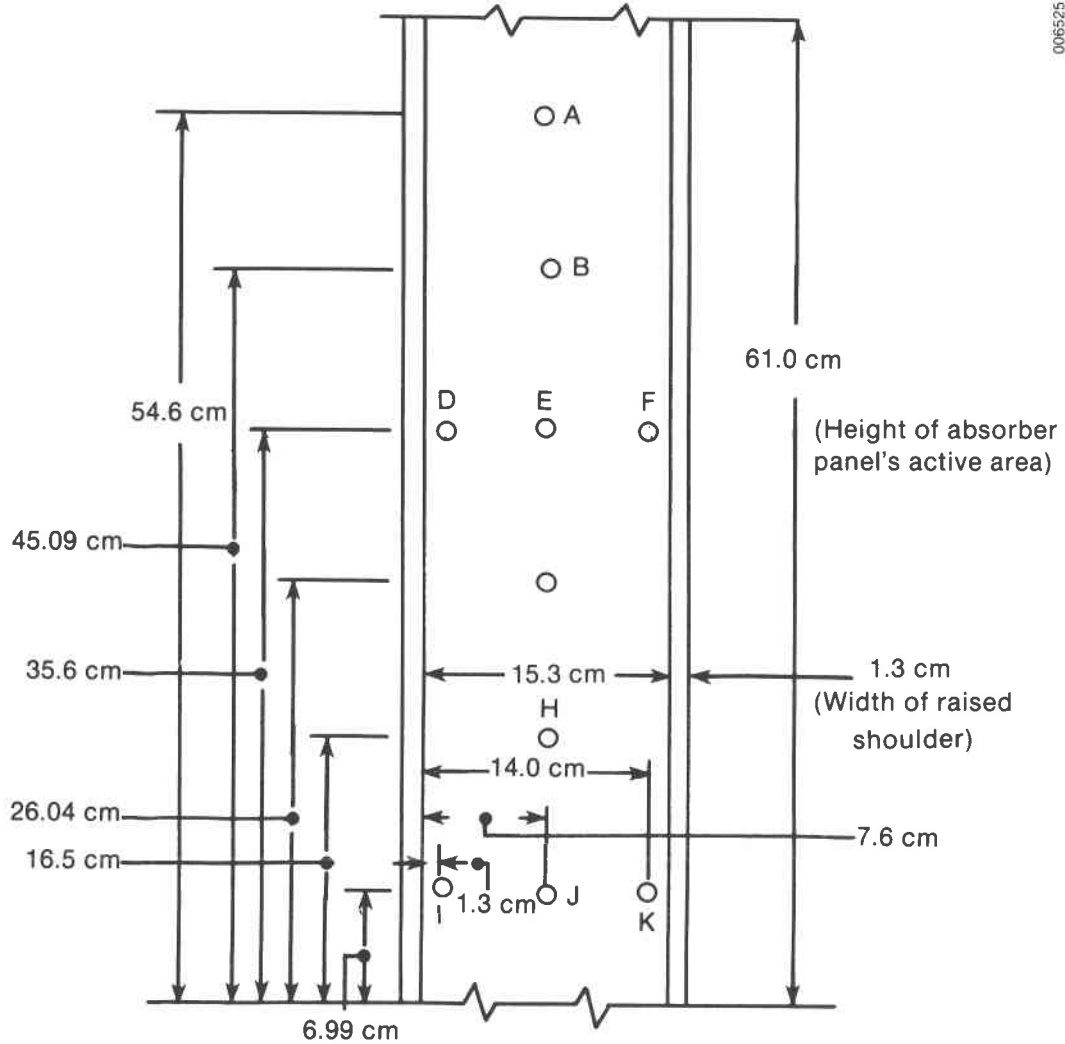
Figure 2-6. Absorber Panel Dimensions

plumbing, storage tank, and absorber assembly locations in diagram form. Heater, pump, and valve controls are located in their proper location in the diagram to help identify the control function desired.

2.7 Receiver

The DAR assembly tested at the ACTF included all components near the optical focus: the absorber panel, optical cavity, water-cooled shield, cabinet, instrumentation, spill tray, insulation, and structural supports. This receiver assembly is shown in Figure 2-4.

2.7.1 Functions

The receiver and its components perform the following functions:

- The cavity redirects the upward-directed flux from the mirror field. Diffuse reflection from the cavity's interior surface provides a relatively uniform flux distribution on the absorber panel.

- The receiver assembly minimizes heat loss from convection, conduction, and re-radiation and provides protection from the weather.

- Space frames support the absorber and permit leveling.

- The cavity and water-cooled shield protect vulnerable components from the solar beam.

- The fixed calorimeters and the flux rake measure the flux distribution on the absorber.

- The tray beneath the trough catches small salt spills.

2.7.2 Assembly Procedure

The assembly procedure heavily influenced the receiver design. We planned to install the absorber and all the piping and perform ground tests before installing the rest of the receiver. This meant that the shield, cavity, and cabinet had to be installed around the absorber, its support frames, and piping. The assembly steps are listed in order:

- Stainless steel wings were welded to the absorber. These wings would help position the silica foam blocks composing the cavity and support the fixed calorimeters along each edge (see Figure 2-7).

- An Inconel space frame was welded to the back of the absorber. A mating frame was assembled on the skid.

- The absorber was positioned, and the two frames were pinned together and adjusted.

- The back of the absorber was insulated.

- The water-cooled shield was positioned and installed. The shield is rigidly attached to the 12.7-cm channels around the focal zone by six short angles. The shield, like the rest of the receiver, is tilted back 5 deg. The angles join the level skid to the tilted receiver.

- The fixed calorimeters were installed and cooling water piping connected.

- Foamed silica slabs were placed on top of the shield and under and behind the absorber. The slabs insulate the cooled shield from the hot interior of the receiver. A 316 stainless tray was placed over the slabs to prevent spilled salt from saturating and attacking the foam.

- A shaped block of foamed silica was placed on the shield just in front of the trough to protect the trough from the solar beam.

- The two cavity block retainers were attached to the absorber wings. These thin, stainless steel sheets encircle and stabilize the cavity blocks without damaging them. The circle is closed by four soft extension springs that keep the retainer snug around the blocks as it heats up (the retainer expands much more than the blocks do).
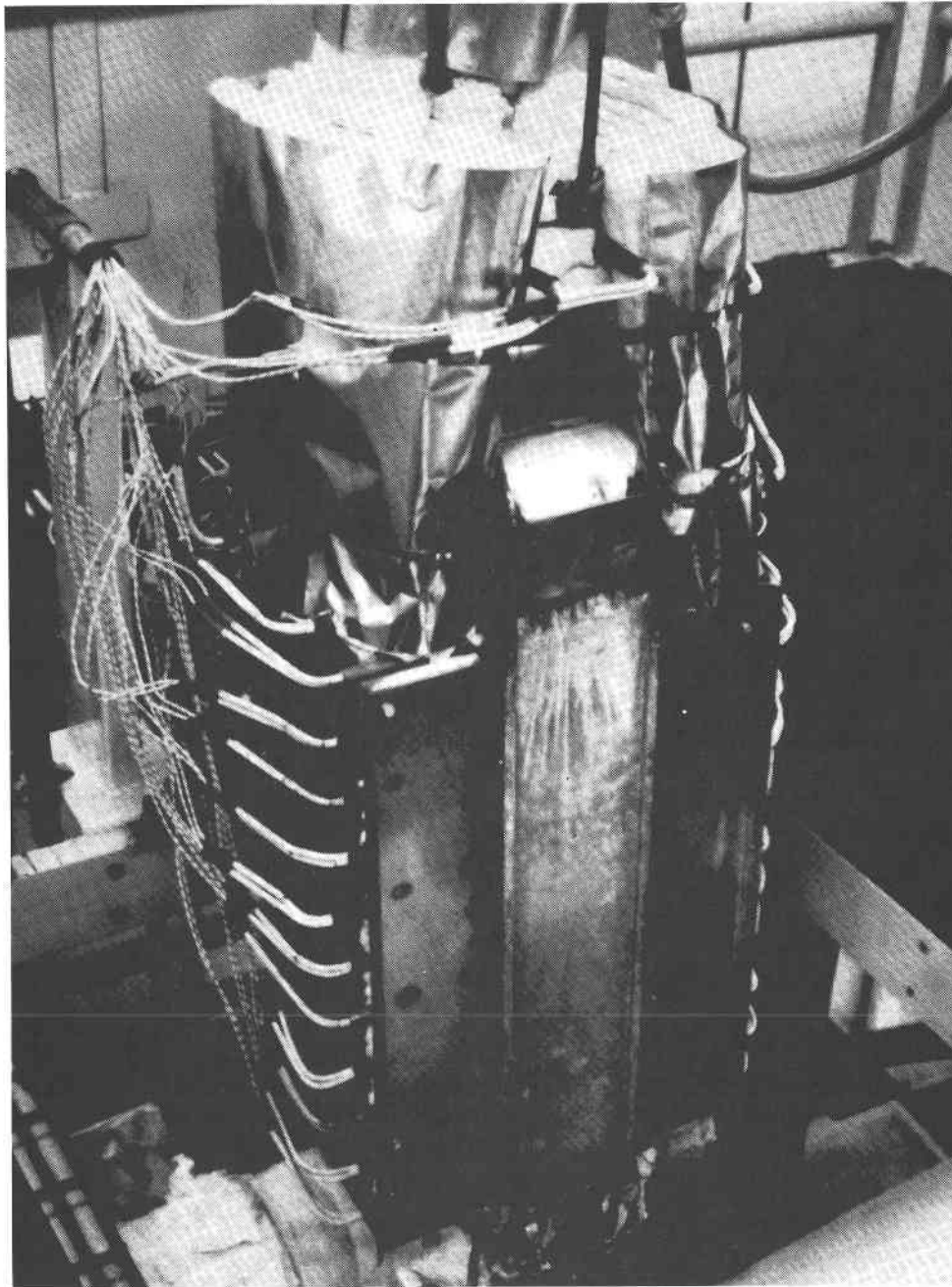
Figure 2-7. Absorber, Wings, and Insulation

- The foamed silica blocks that form the octagonal wall of the cavity were set in place. Their weight rests on the shield, while the retainer holds them in place. The two ceiling blocks were set in place last (see Figure 2-8).

- The cabinet was assembled around the absorber and cavity. The top surface of the shield has tapped holes for the screws that anchor the cabinet.

- Blanket and bulk Kaowool was packed around the pipes, cavity, and sides of the absorber. Insulation was installed through the easily removable cabinet roof.
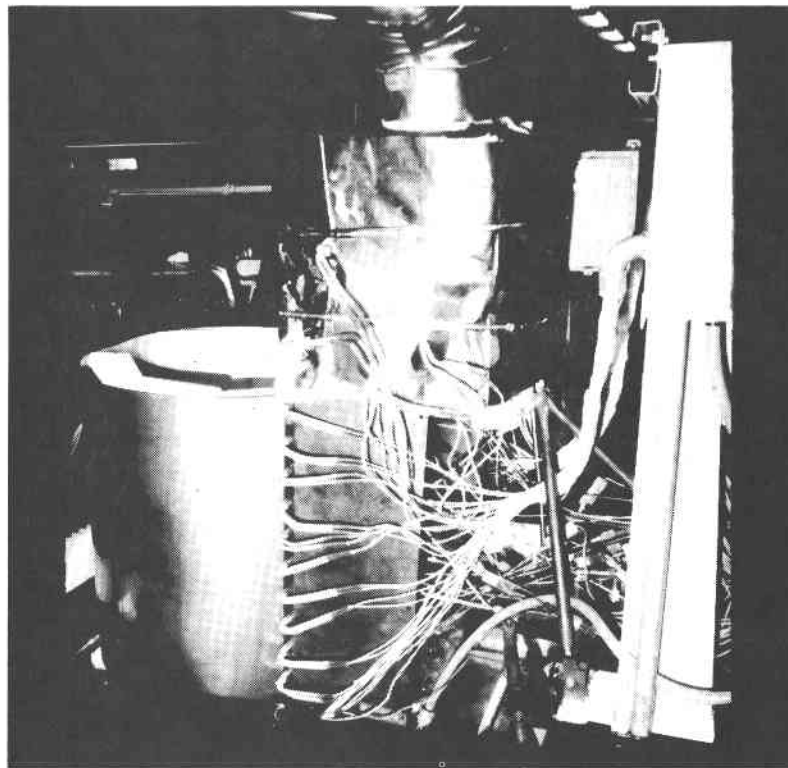
Figure 2-8. Cavity Assembly

2.7.3 Cavity Design

The optical design of the cavity is described in the GTRI final report, *Molten Salt Test Apparatus Design* (Asbell et al. 1984). The optimized cavity was to be a right circular cylinder with the cylinder and aperture having a 46-cm diameter. The absorber would replace part of the cylinder wall. The top of the cylinder, the cavity ceiling, was to be at the top of the absorber active zone, while the bottom of the active zone was to be no more than 10 cm above the aperture (focal) plane. The walls were to be insulated and uncooled and have a diffuse reflectivity greater than 85%. The predicted average solar flux on the absorber was 50 W/cm^2, and the predicted average wall temperature was 670°C. Measured performance is discussed in Section 2.8.

The mechanical design approximates the optical design. The cylinder became an octagon, 46 cm across corners. The octagon is formed of 7.6-cm-thick foamed silica blocks with the optical surfaces coated with silica slip. This offers excellent insulation, diffuse reflectivity (see Appendix D), resistance to high temperatures and thermal shock, and workability. The lower end of the octagon extends below the focal plane, allowing it to admit all the energy that would pass through a 46-cm circle at the focal plane. We used a conical template to establish the desired shape and a rasp to remove excess material. Figure 2-5 shows the final shape.

The foamed silica is quite delicate, and molten carbonate salts attack it. The cavity design held mechanical stresses to a minimum. The blocks' weight rests on the water-cooled shield, while the spring-loaded retainer gently holds the blocks together. As the

cavity heats and cools, the retainer expands and contracts while the size of the blocks remains virtually constant.

The retainer springs keep a steady pressure on the blocks. The wings are designed to prevent the molten salt from wicking from the absorber edge to the silica blocks. There is a 0.16-cm gap between the wings and absorber. The structural connection is made behind the absorber. There was no wicking to the blocks during testing, but under certain conditions salt vapor caused minor damage to the blocks' surfaces, and salt leaks heavily damaged the block directly in front of the trough. The damage was easily repaired using a thick mixture similar to the slip coating.

This cavity design differs from a commercial DAR in that the interior of the commercial unit would be substantially covered with salt film. Because of total power limitations, we restricted the experimental cavity design to one panel 15.2 cm wide. Since the rest of the cavity was highly reflective, the absorber plate was exposed primarily to solar wavelengths (see Section 6.1). Data on this single panel are applicable to the commercial receiver with the exception of one phenomenon we observed, which is discussed in Section 6.4.

2.7.4   Integration of the Cavity with the Test Loop and ACTF

The cavity is integrated with the test loop and ACTF optically, structurally, and electrically. We also had to plumb it and wire the instruments. Optical integration includes placing the center of the cavity's aperture at the focus of the mirror field and shaping the aperture to accept the full 90-deg cone of energy. Structurally, the cavity is integrated with the test loop through the water-cooled shield and absorber support frames. Electrical integration includes wiring for the resistance heaters in the absorber plate and on the manifold and trough. This wiring, like the instrumentation wiring and fixed calorimeter plumbing, leaves the cabinet in the back where the absorber space frames are joined and ends at the temperature controllers on the skid.

Cooling water for the shield and flux rake travels through rubber hoses from the connections on the tower. The faucets are equipped with flowmeters. The warm return water is routed into the large drain pipe on the tower. The plumbing for the fixed calorimeters is described in Section 2.8.

The absorber, trough, manifold, and piping contain many thermocouples. Four thermocouples are embedded in the silica block opposite the absorber about 38 cm below the top of the active zone (cavity ceiling level). These thermocouples are 1.3, 2.5, 3.8, and 5 cm from the reflective surface of the block. Their wiring is brought out through the back of the cabinet and connected to terminal strips in the junction box behind the cabinet.

Wiring for the fixed calorimeters terminates in the junction box. Wiring for the calorimeters in the flux rake runs directly to the back plane in the tower control room.

2.8 Flux Measurement

The flux incident on the absorber is measured with two sets of Gardon gauge calorimeters: one set fixed along the absorber edges, the other mounted in a vertically translating flux rake. The calorimeters are water cooled and produce a DC voltage corresponding to total incident energy flux (wavelength independent). Each gauge is
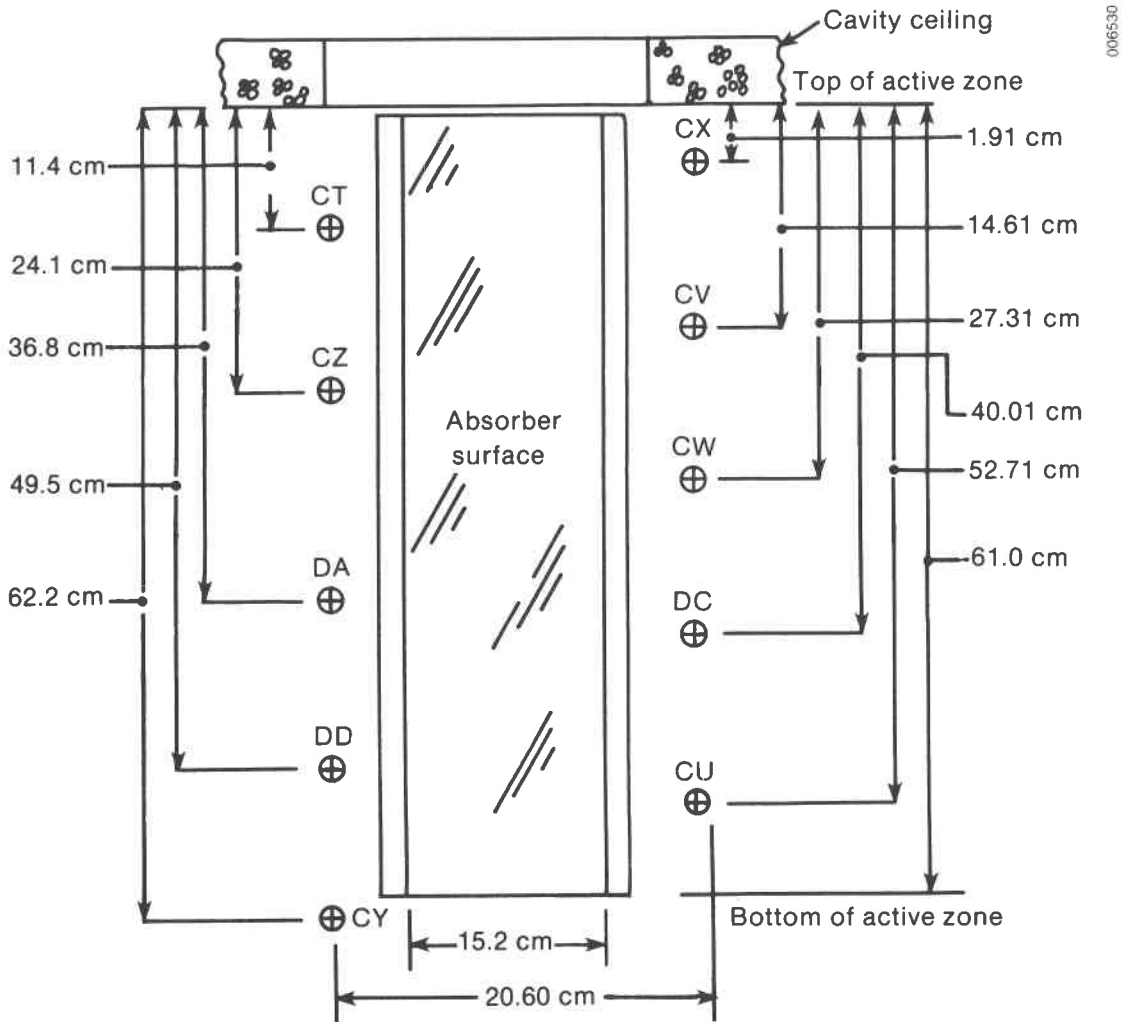
Figure 2-9. Locations of the Fixed Calorimeter

supplied with a calibration curve by the manufacturer, Hy-Cal (see Appendix E for a typical calibration curve). All wiring runs to the back plane in the tower control room; the wiring from the fixed calorimeters runs through the junction box behind the cabinet.

The intent was to have the fixed calorimeters be the primary source of flux data and the rake verify that the flux variation across the absorber was acceptably small (see Section 5.3 for results).

2.8.1 Fixed Calorimeters

The locations of the 10 fixed calorimeters are shown in Figure 2-9. The sensors are in the plane of the welded absorber edges 22 mm in front of the absorber surface, in two
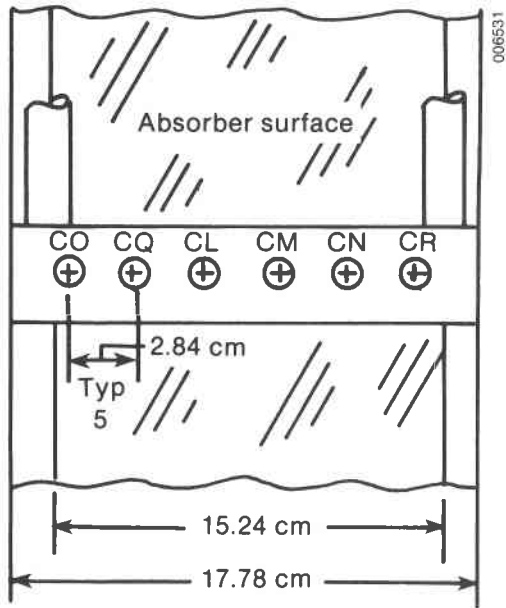
Figure 2-10. Flux Rake Calorimeter Location
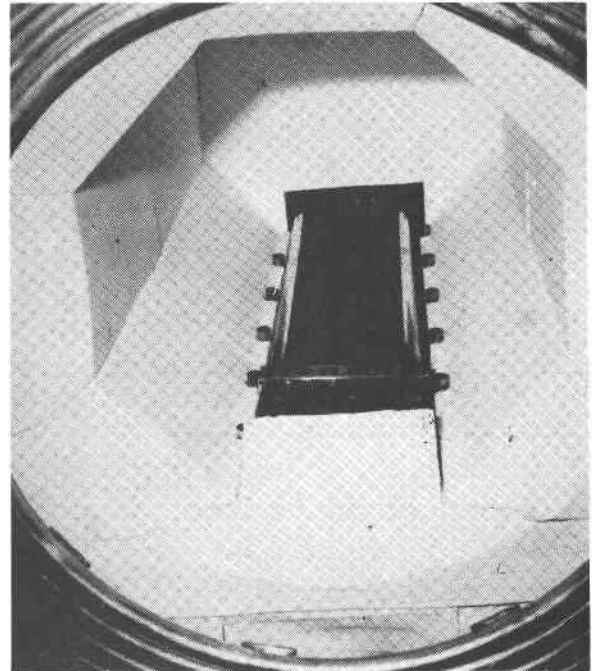
Figure 2-11. Flux Rake in Cavity
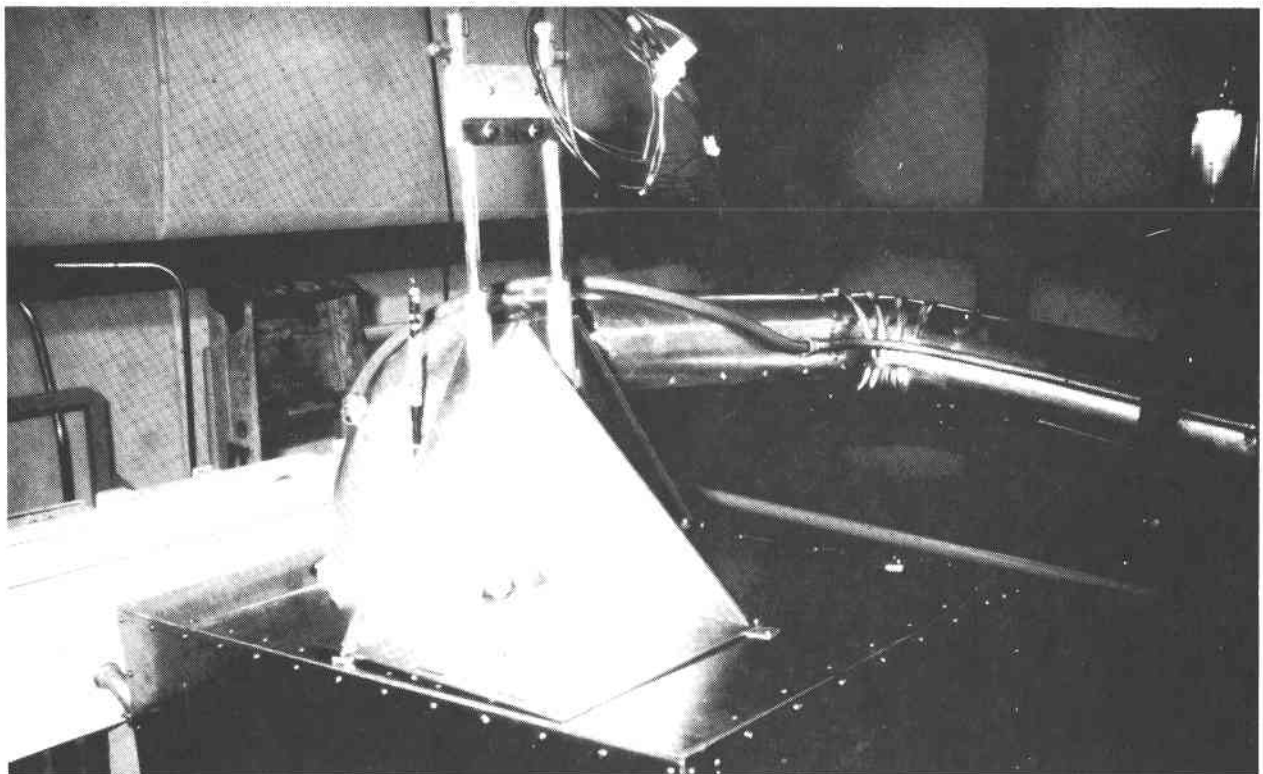
Figure 2-12. Flux Rake Mounted on Cabinet

vertical rows 20.6 cm apart. The calorimeters are secured in tubes welded to the absorber wings. Cooling water enters and leaves each calorimeter through two small-diameter stainless steel tubes. Soft copper tubing was soldered to these tubes to extend them. The supply water passes through a water filter (to remove contaminants that might clog a tube) and a hard-soldered copper manifold that feeds each calorimeter separately. The return tubes are kept separate all the way to the tower drain pipe, so proper flow through each calorimeter can be verified. The wiring is Teflon insulated and cannot tolerate the high temperature near the absorber. The wires for each calorimeter are routed with the cold-water tube and tightly wrapped with high-temperature tape; this keeps wiring temperatures low. The wiring terminates in the junction box behind the cabinet. Data from the fixed calorimeters were collected continuously during the tower tests.

2.8.2 Flux Rake

The flux rake has a horizontal array of six sensors that traverses the length of the absorber. The locations and names of the sensors are shown in Figure 2-10. The rake is shown installed in Figures 2-11 and 2-12. The calorimeters are mounted flush in a horizontal bar (Figure 2-13). The rake is adjusted so the bar has about 6.4 mm clearance from the absorber edges. This places the plane of the sensors 57 mm in front of the absorber face. Two vertical tubes that slide through plastic sleeves mounted above the cabinet carry the bar. Movement is manual, and the sensor position is determined by tape measurements made outside the cabinet. Both cooling water and wiring pass through the bar and vertical tubes (Figure 2-14). Hy-Cal manufactured the calorimeters to a custom design created by Hy-Cal and GTRI. The design features waterproof wiring. The rake is made of polished aluminum to minimize heat absorption and temperature gradients in the metal. Section 5.3 presents the results of the flux measurements.
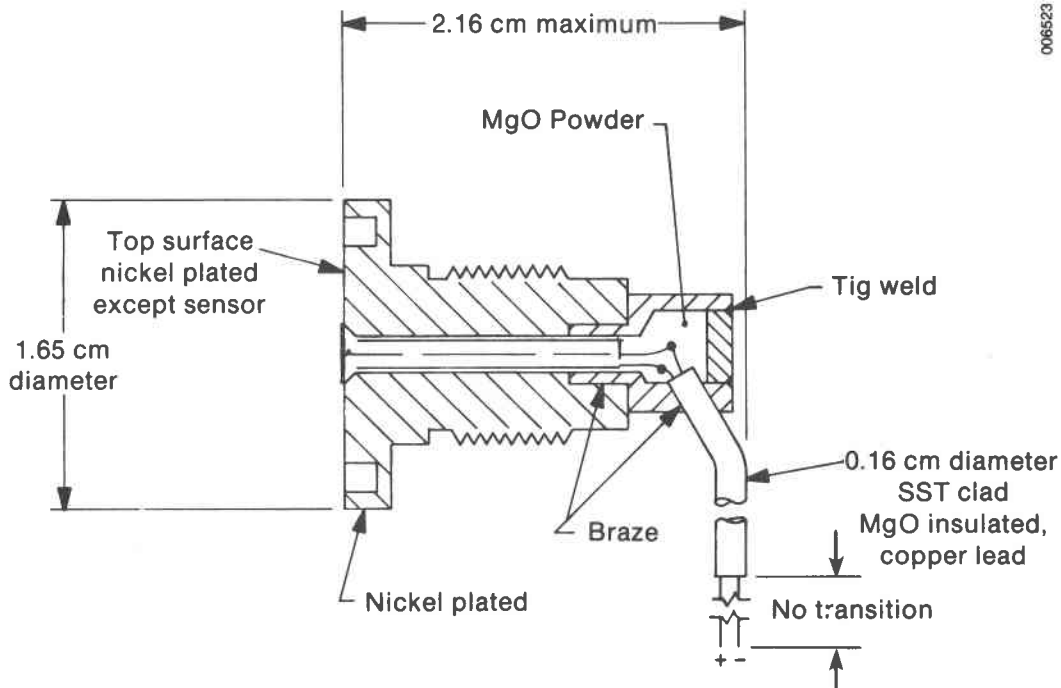
Figure 2-13. Custom-Designed Calorimeter as Used in Flux Rake

17
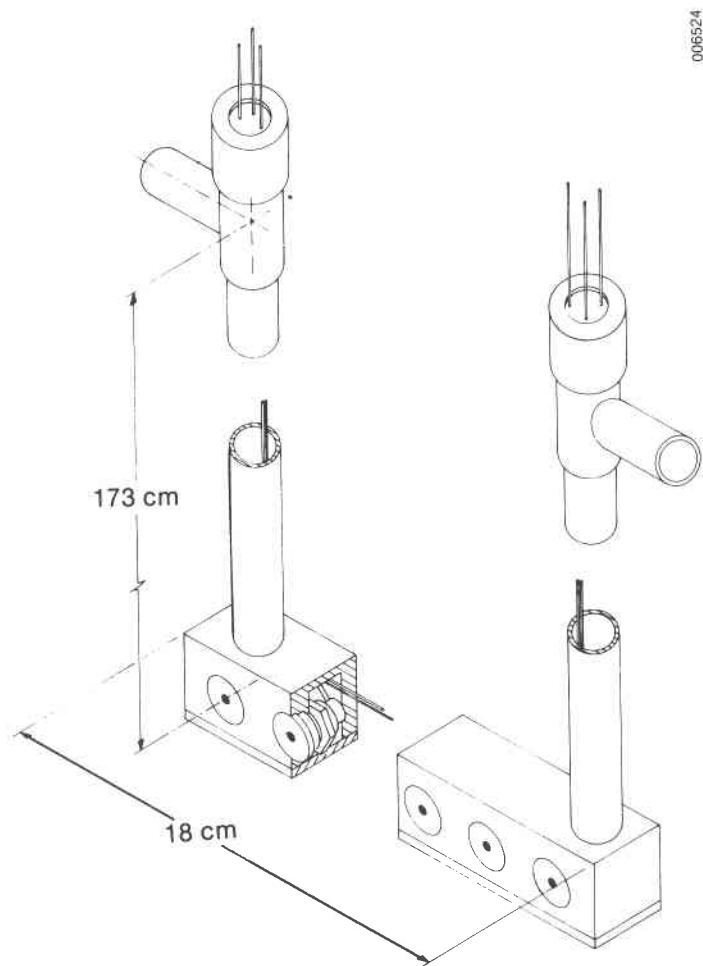
Figure 2-14. Flux Rake Bar and Vertical Tubes for Wiring

3.0 DESCRIPTION OF THE ADVANCED COMPONENT TEST FACILITY

3.1 Introduction

The GTRI Advanced Component Test Facility (ACTF) is a tracking-mirror solar concentrator system (see Figure 3-1). The facility is run by GTRI for the U.S. Department of Energy (DOE). Its primary purpose is to encourage research and development in high-temperature solar thermal technology. The facility is flexible, convenient, and accessible to all qualified research and development organizations, large and small, public and private.

The ACTF is particularly well suited for testing central receiver components and systems, high-temperature insulation and structural materials, direct energy conversion components and systems exposed to high heat flux, and total energy systems using solar energy alone or combined with fossil fuel energy (hybrid) systems.

Major elements of the facility include a solar concentrating mirror field, a rigid structural steel test tower located at the geometric center of the mirror field, an experiment support platform (tower deck) integrated in the tower, an instrument and control building, a computerized data collection system, and a heat-rejection system.

Since its construction in 1977, the facility has been used to test and evaluate several innovative concepts for converting high-temperature solar energy into other, more useful forms of energy. Specific examples of conversion hardware evaluated at the ACTF
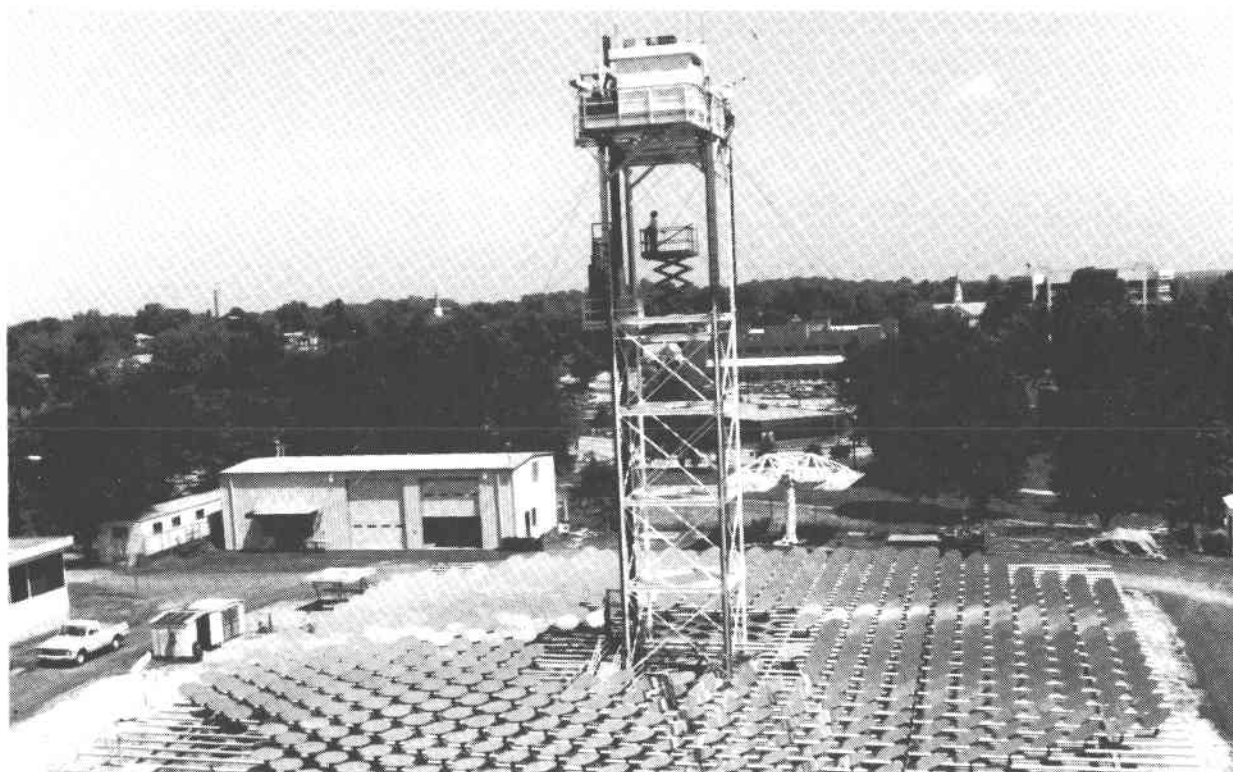
Figure 3-1. U.S. DOE Advanced Component Test Facility
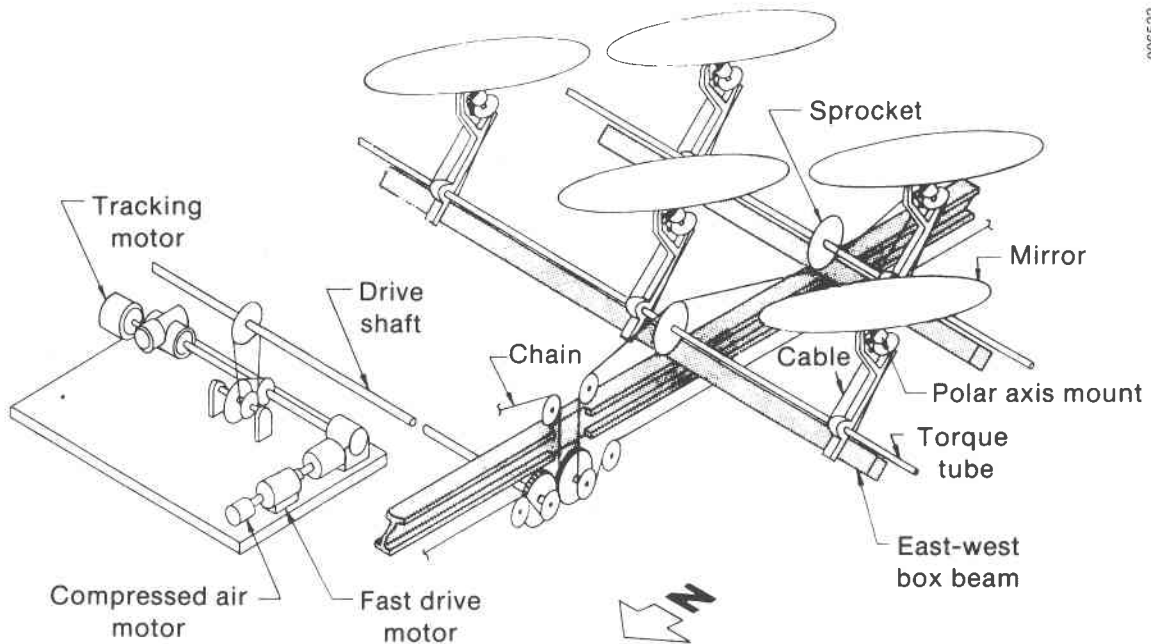
Figure 3-2. ACTF Mirror Field Drive Train

include a directly heated fluidized-bed solar receiver; a high-pressure, single-pass-to-superheat steam generator; a liquid sodium heat pipe receiver; a flash pyrolysis biomass gasifier; and a Stirling engine and electrical generator combination connected to a utility grid. Additionally, several materials have been tested to see if they can survive the concentrated solar beam. The facility is described in more detail in the ACTF *User's Manual* (GTRI 1981).

3.2 Mirror Field

The ACTF mirror field consists of 550 heliostats deployed in an octagonal array around a central experiment support tower. The mirrors are individually aimed and focused at the center of a 2.44-m × 2.44-m square aperture in the deck of the support tower. Each mirror is fastened to a polar mount that permits individual manual declination as well as collective tracking of the sun to maintain a stationary focus in the platform aperture. The maximum solar flux available at the focus is approximately 192 W/cm^2, representing a total power input of 325 kW. Fluxes depend on the time of day and year.

All heliostats are mechanically interconnected and are driven in unison with a multiple chain-sprocket-torque tube linkage (see Figure 3-2). The system drivers are two independent electric motors and a compressed-air-driven motor. One electric motor is used for slewing the mirrors to focus and unfocus the concentrated solar beam on the test object. The second electric motor drives the mirror field in tracking the sun. The compressed-air-driven motor is used to drive the mirror field to the sunrise limit when electric power is lost.

20

The mirrors are circular second-surface reflectors 111 cm in diameter and are made of 3-mm-thick glass. Each mirror is supported on a circular ring near its outer edge and is rigidly fastened to the polar axis mount at its center. The polar axis mount and support structure are shown in Figure 3-3. Each individual mirror is focused by applying a moment to the edge of the glass, warping the mirror into a spherical shape.

3.3 Tower

The central test tower, shown in Figures 3-4 and 3-5, is a rigid, guyed steel structure capable of supporting a 9100-kg experimental package. The mirror field's aim point is centered in the tower deck aperture. Two pins at diagonally opposite corners of the aperture locate the apparatus. We can alternately expose an experiment in the focal region to and protect it from the concentrated solar beam by adjusting a pair of pneumatically driven shutters.

The tower platform can be accessed by an elevator with a load capacity of 454 kg. A hydraulically operated scissors lift with similar lifting capacity provides access to the underside of hardware mounted in the deck opening. Hardware exceeding the weight or size limitations of the elevator is lifted to the tower deck with a mobile crane.

A small building on the south side of the tower deck houses the analog interface unit used for data collection and other support equipment required on the tower. Limited space is also available for hardware and instrumentation associated with the test program.

3.4   Control Building and Data Collection System

A 52.3-m^2 ground-level control building west of the mirror field provides a central location for the staff and users to monitor and control tests. The control building houses the
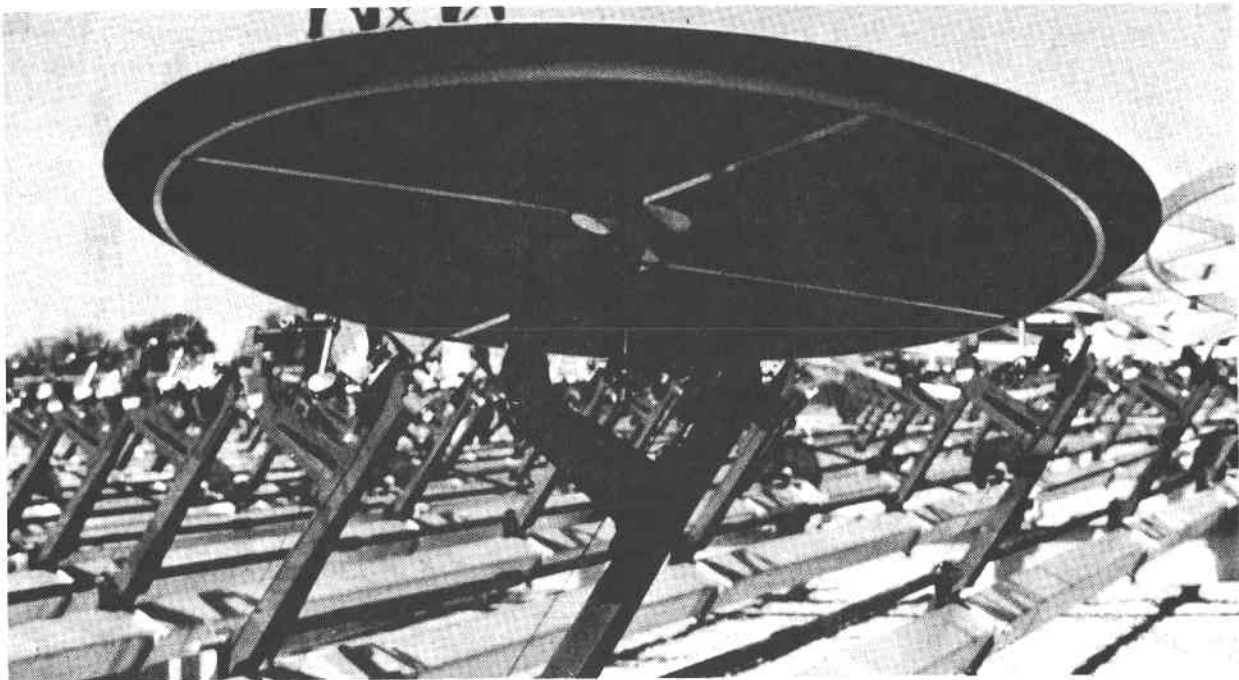
Figure 3-3. Close-Up View of Heliostat Mount

Focus is centered in opening. Clear opening in deck grating is 8.0 ft² (2.44 m²). Tower base is 14.0 ft × 14.0 ft (4.27 m) measured from column center to column center. Elevator is mounted on west face of tower.
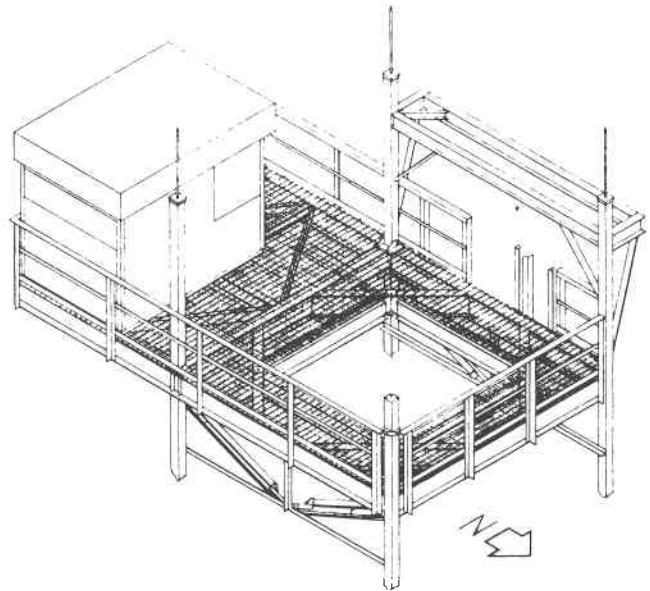
Figure 3-4. Isometric View of ACTF Tower Deck

ACTF computer data system, including various output devices for real-time inspection of the test data. Ample space and utilities are available for the users' control consoles and displays.

The data collection system can record, condition, display, and reduce user data. The system has an HP-1000 minicomputer, nine 16-bit multiplexed analog-to-digital (A-D) subsystems, several graphic's terminals to display data in real time, disk mass storage devices, and a four-color graphic's plotter. The computer is in the control building and serves as the master control for the system. The intelligent A-D subsystem in the tower deck building serves as an interface between the sensors and the minicomputer and operates unattended. The 128 channels can be scanned at up to 5800 channels per second; a single channel can be scanned 6000 times per second. The computer software controls all the scanning routines.

Each channel corresponds to a different transducer; i.e., thermocouple, level sensor, pressure sensor, valve status, etc. All channels may be digitized and stored on disk at any selected interval (typically once every second). The experiment can be monitored in real time from up to four independent video display monitors. Each video monitor output can be tailored to suit the individual experimenter's needs on station at that monitor. All monitors can display lists of channel values in real time, while one monitor can display these channel values against a graphical representation of the experiment. These monitors can be in the control room or at the test location. To help the experimenter control the experiment, individual set-point alarms may be assigned to each channel. A two-tier system of alarms has been implemented. The first-level alarm gives an advance warning of impending problems; the second-level alarm generally requires that the experiment be shut down. These alarms show up as reversed video output and flashing output, respectively, on the video monitors.
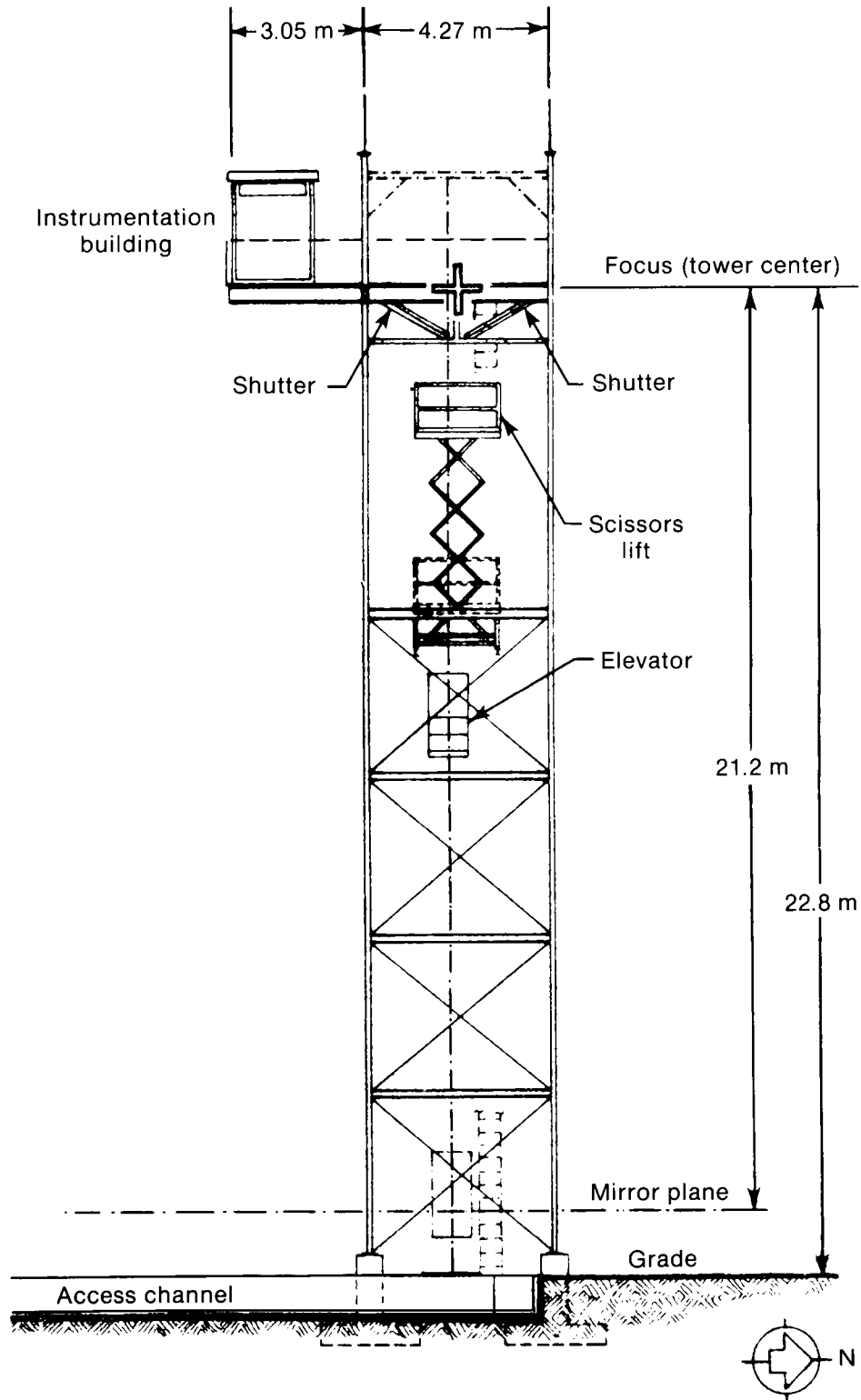
Figure 3-5. East Elevation View of Test Tower

A system of predefined events may also be specified to the data acquisition system; the analog channels are then continuously monitored for the occurrence of these events. When an "event" occurs (e.g., valve closure), it is automatically entered along with the time into a computer-generated log for that day's experiment.

Several computer programs are available to analyze the day's data off-line in tabular and graphical hard-copy forms. Typically, these analyses are available within two hours of daily shut down.

A scanning heat-flux calorimeter that is water cooled is available for measuring solar-radiation intensities at or near the mirror-field focal plane. The system can be mounted at various levels in the tower-deck aperture and can measure flux distribution and total energy incident on an aperture of an experiment.

3.5 Closed-Circuit Television System

The ACTF closed-circuit television (CCTV) system supports the solar testing at the facility. It includes three pan-and-tilt, auto-iris cameras mounted in protective housings to observe test activities on the tower. Two of these cameras can be relocated to support specific experimental needs. Additionally, the facility has two portable, nonhoused cameras that can be mounted on a tripod. The CCTV system also includes five TV monitors, a time/date generator, a standard video recorder, and several signal switching accessories. The time/date generator and video recorder combination allows a permanent record to be made of visual parameters. The time impressed on the recorded image is synchronized to the data system's clock to correlate TV-recorded data with computer-recorded data.

4.0 GROUND TESTS

We tested the apparatus in the ACTF shop assembly building before mounting it on the tower. With these ground tests we verified that the apparatus and data system were functioning properly, calibrated the instruments, and made modifications to the apparatus.

We preferred performing these shakedown tests on the ground rather than on the tower because the tower offered limited access to the apparatus and was exposed to the weather. The cavity was not installed around the absorber panel until after the ground tests so we could observe the salt flow on the panel.

4.1 Test Plan and Execution

We performed the following ground tests:

1. Verified that the the trace heaters, temperaure controllers, and over-temperature control units functioned properly
2. Tested the tank 1 cooling coil and measured cooling capacity
3. Leveled the weir in the absorber panel inlet manifold and set the absorber panel slope
4. Calibrated the salt flowmeter (described in Section 4.3)
5. Checked the data aquisition system
6. Determined salt-flow rates at which the salt film breakdown occurred
7. Videotaped the salt film flowing on the absorber panel.

In test 1 we turned on each of the trace heat zones one at a time and measured the current flowing to each heating element. Each zone was then monitored for a period of time to see how the temperature controllers operated. Each of the over-temperature control units was tested and their proper function confirmed.

In test 2 we calibrated the pressure transducer used to measure airflow rate (via pressure drop across an orifice) against a mercury manometer. Tank 1 was then filled with salt and heated to 600°C. The trace heaters to tank 1 were turned off, and the maximum airflow available to the cooling coil was run for a half hour. Based on the salt mass in tank 1 and the temperature drop over the test period, we found that the tank cooled at a rate of 41 kW.

In test 3 we used very low salt flow rates to observe the inlet manifold weir orientation. The salt distribution across the weir was very sensitive to this orientation. Threaded fittings in the absorber panel support structure were adjusted to set the weir horizontal. The slope of the absorber panel was then set at 5 deg from vertical using a bubble slope indicator.

In test 5 we verified the identity of each thermocouple on the apparatus by disconnecting each one individually and noting the open-circuit indication on the data system. Altering the signal wire grounding configurations was necessary to reduce electronic noise on several data channels.

In test 6 the salt-flow rate was gradually reduced until a dry spot appeared, which occurred at 0.34 m^2/h. This test was performed with a salt temperature of 611°C and corresponds to Re (Γ/μ) = 15.4.
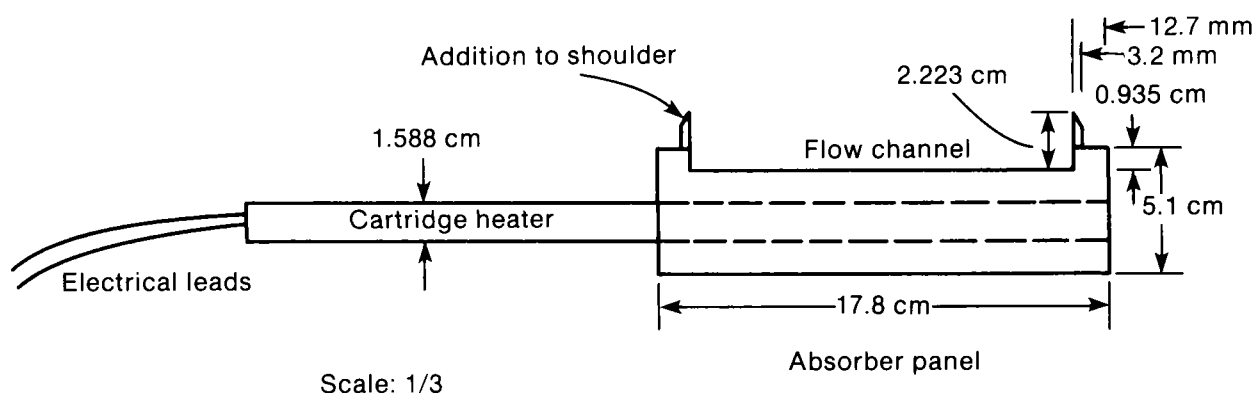
Figure 4-1. Absorber Cross Section

Test 7 was an approximately 15-min videotape of the salt flowing on the panel at 600°C at flow rates between 0.15 and 15 m²/h. The salt film had a distinct pattern of waves traveling down the panel at flow rates less than 3.01 m²/h. At higher flow rates the surface of the film was smooth with no discernable wave pattern. The most likely explanation of this behavior is the existence of waves in the inlet manifold at the lower flow rates.

4.2 Operational Problems and Solutions

At the beginning of the ground tests, we found that the 2-in.-diameter drain line from the absorber panel to tank 1 did not have an adequate capacity to carry the desired flow rates of salt. After removing the insulation from the pipe and inspecting it more closely, we saw that the pipe did not have the required slope to drain the salt. We then changed the slope of the pipe and reinsulated it. Subsequently, the drain line worked well for flow rates up to 2.7 m³/h.

Observations of salt flow on the absorber panel showed that for flow rates above 7.2 m²/h, the salt flow was not confined to the 9.65-mm-deep flow channel. The salt tended to climb the shoulders of the panel (see Figure 2-3) and run down the sides of the absorber. This loss of containment became more pronounced as flow rate increased. This behavior of the salt is caused by its low contact angle with oxidized Inconel 600 (estimated as 10 deg or less) and its high surface tension, which allows it to creep.

To confine the salt we increased the flow channel depth to 22.4 mm by adding 12.7-mm-wide strips of Inconel 600 down both sides of the panel (see Figure 4-1). This reduced the salt loss but did not eliminate it. We then sharpened the edge of both shoulders of the panel and found that the salt flow was well contained in the flow channel. The high surface tension of the salt prevents it from creeping around the sharp edge (see Figure 6-7a). It appears that the sharpened edge effectively controls the open salt flows; it is probably more effective than additional height for surfaces that are wetted by the salt. With the flow contained at the top 15 cm of the panel, the bottom 45 cm remained well behaved.

During the ground tests, minor modifications were made to many parts of the apparatus. Modifications to the gas supply lines used to pressurize tank 2 reduced the time required to pressurize the tank from 20 to 2 min. Rheostats were added to the trace heat circuits for the drain line from the absorber to tank 1 and for the transfer line

between the tanks to provide better temperature control on those lines. After completing the ground tests, we mounted the cavity, the cooling shield, and the weather housing around the absorber panel to prepare for the tower tests.

4.3 Salt Flowmeter Calibration

The test loop was designed with a venturi salt flowmeter with pressure taps upstream and at the venturi throat. Taps led to pressure transducers designed with pressure diaphragms facing the molten salt. Originally we were going to calibrate this flowmeter by flowing salt out of tank 2 and using the change in salt level in tank 2 versus time as an absolute measure of volumetric flow rate. This flowmetering technique was abandoned because the transducers failed. Freezing and remelting of the salt present on the diaphragms because of poor drainage during the first shutdown probably damaged the pressure diaphragms.

Because the pressure transducers failed, an alternative technique was devised for measuring the salt flow rate while pumping salt out of tank 1. This technique takes advantage of the variable-speed pump and requires a two-step calibration. The first step is to calibrate the height of the salt flowing over the weir (in the inlet manifold to the absorber panel) against the flow rate out of tank 2. The second step is to calibrate the pump speed against the height of the salt over the weir. These two steps combine to calibrate flow rate versus pump speed.

The height of a liquid flowing over a rectangular weir can be predicted as a function of flow rate (Streeter 1971):

$$Q = (2/3)(2g)^{1/2} c_v WH^{3/2} , \qquad (4\text{-}1)$$

where

Q = volumetric flow rate
g = acceleration of gravity
C_v = discharge coefficient = 0.6.
W = width of weir
H = height of upstream liquid surface above weir

C_v compensates for contraction of the flow over the weir. Because we measured the height of liquid over the weir h rather than the upstream height according to Streeter (1971), we set $C_v = 1$. The width of the weir W is 15.2 cm. With new units the equation reduces to

$$Q = 28.9h^{1.5} , \qquad (4\text{-}2)$$

where

Q = flow rate

h = height.

The apparatus used to measure the liquid height over the weir and thus determine the flow rate (shown in Figure 4-2) consisted of a micrometer with a long, pointed probe attached to isolate it from the hot salt. Because the molten salt conducted electricity
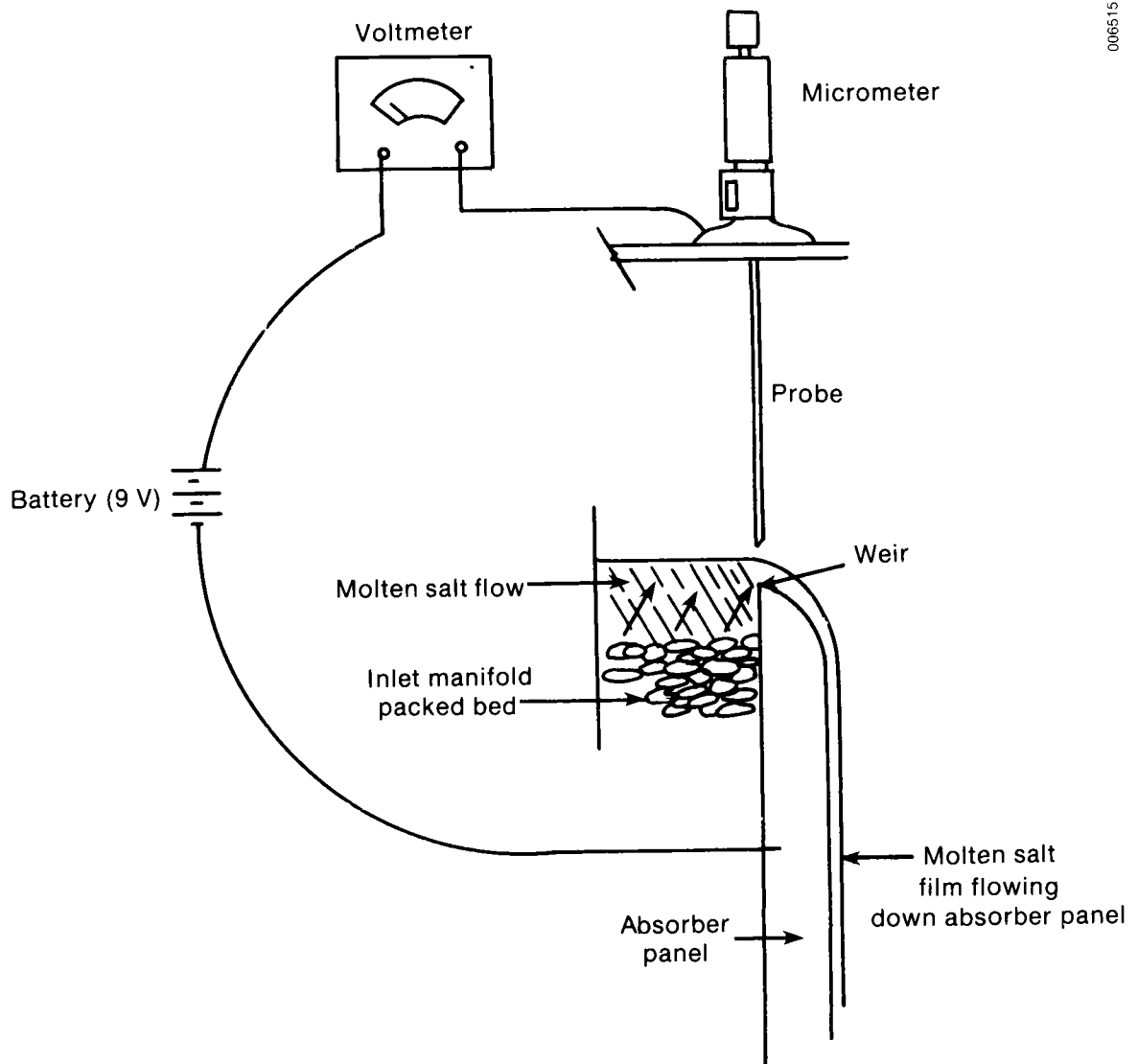
Figure 4-2. Film Thickness Measurement Apparatus

well, electrical continuity was used to indicate contact between the probe and the surface of the salt. Micrometer readings were taken at that point and when the probe bottomed out onto the lip of the weir. The difference between the two readings was the liquid height.

The first step of the calibration was to verify this prediction by flowing salt from tank 2 and comparing the flow rate to the measured height of the salt flowing over the weir. Data for this step were obtained at three temperatures during experiments on four different days (tabulated in Appendix E). The data are plotted in Figure 4-3 as height of
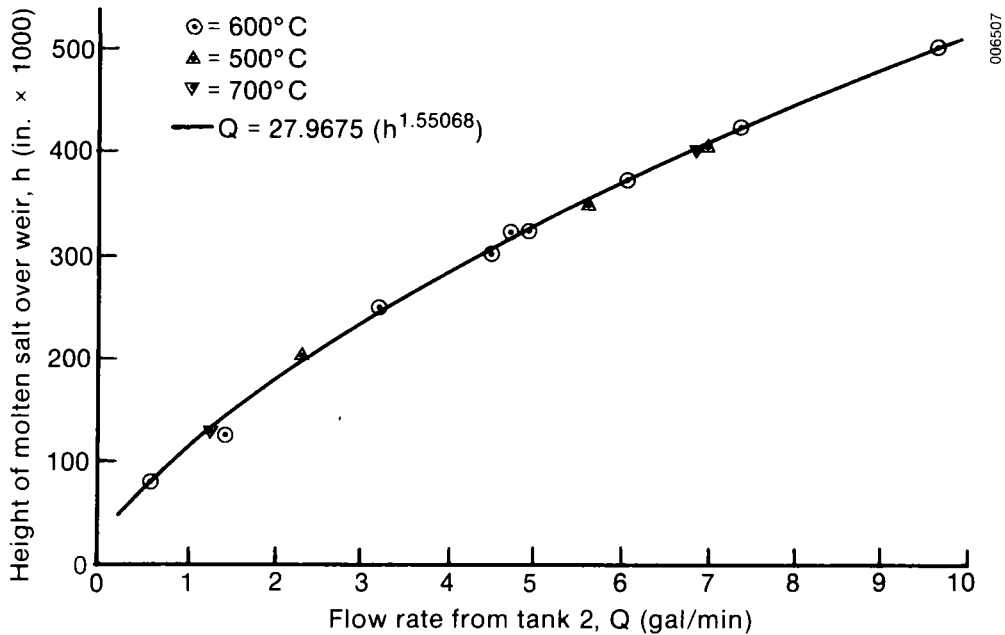
Figure 4-3. Correlation of Weir Film Thickness versus Volumetric Flow Rate

molten salt over the weir versus flow rate. Also plotted is a least-squares fit of an exponential curve to the data:

$$Q = 27.9675h^{1.55068} .$$
(4-3)

This fit is very similar to the predicted relationship for flow rate as a function of height (Eq. 4-2). In addition, the performance of the weir is the same for all three salt temperatures. This confirms that the flow over the weir is not affected by changes in fluid viscosity and can be used as a reliable measure of salt-flow rate.

The second step of the calibration was to flow salt out of tank 1 and to compare pump speed with the height of the salt over the weir. As previously stated, data were obtained at three temperatures during several experimental runs (see Appendix E). The data are plotted in Figure 4-4 as pump speed versus height of liquid over the weir. This figure clearly shows the effect of temperature on flow rate. This is expected because the salt viscosity changes with temperature and influences the performance of the centrifugal pump.

To get flow rate as a function of pump speed and temperature, we used a two-step analysis. First, least-squares fits to curves for flow rate as a function of pump speed were made to the data for each of the three temperatures.

The equations had the form

$$Q = a + b \ln PS ,$$
(4-4)

29
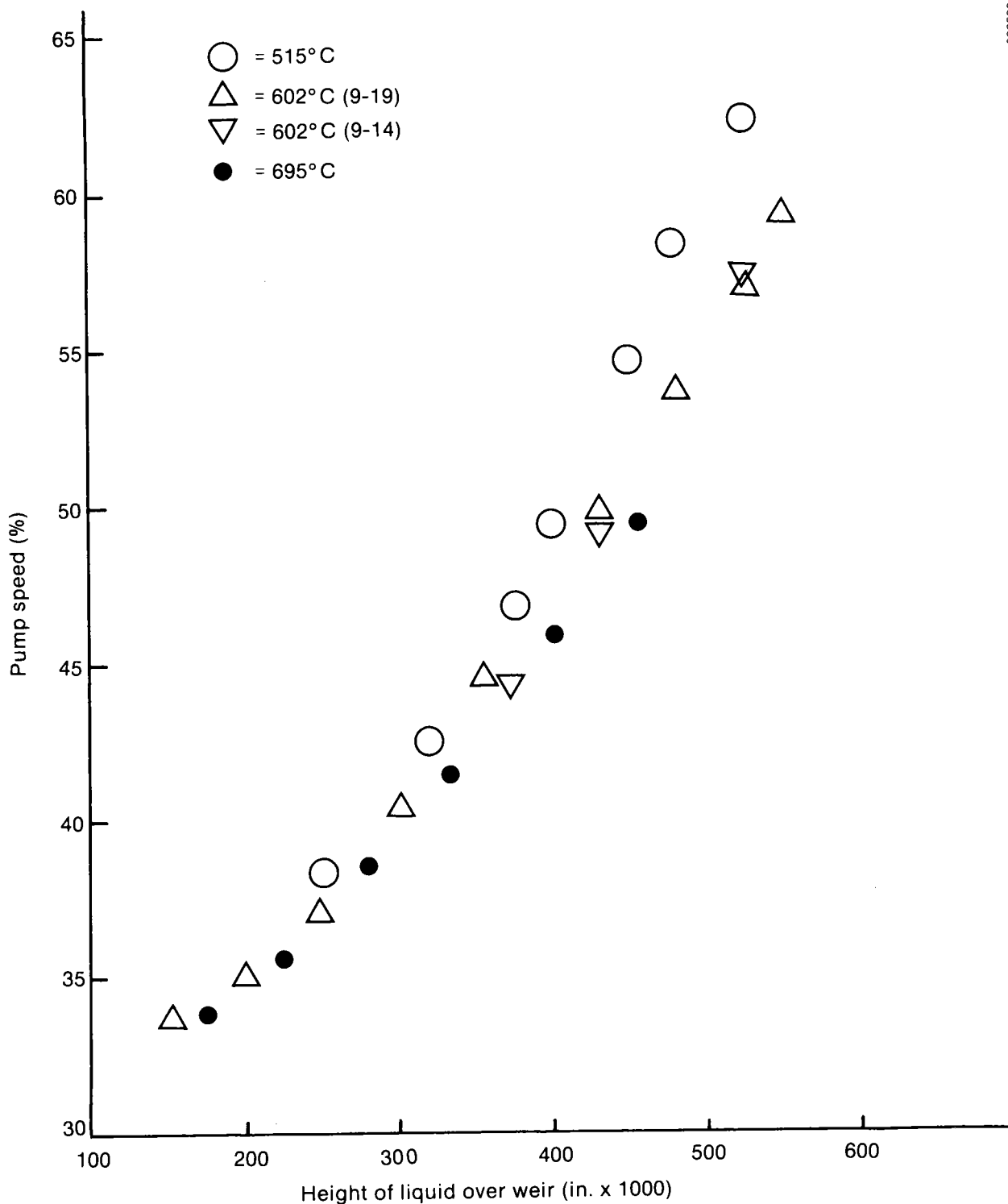
Figure 4-4. Correlation of Salt Pump Speed versus Weir Film Thickness

where

a,b = values defined in Table 4-1

PS = pump speed (%).

Second, an interpolation was made among the three curves based on the salt temperature in tank 1 for a given data point. The pump speed for a given data point was used in these three equations to determine three flow rates. A quadratic curve was fit through these flow rates and then used to interpolate for temperature. These calculations were done in real-time, giving a continuous gallons-per-minute readout during the test.

Table 4-1. Coefficients for Equations for Flow Rate as a Function of Pump Speed[a]

Salt Temperature (°C)	a	b
515	-48.320	14.1313
601	-53.221	15.5933
695	-56.352	16.5243

[a]The measurement technique and an analysis of the errors involved in this calibration are presented in Appendix F.

5.0 ACTF TOWER TEST PLAN

Since the tower tests were the most important part of the research program, we will describe them in detail here. As previously discussed, the tower tests serve several important purposes, which could only be achieved by operating with concentrated solar flux. The tests

- Provided data to compare with the heat transfer model developed by Wang and with other correlations in the literature. In particular, these data include thermal efficiency of the salt film and the heat transfer coefficient at the absorber/salt interface.

- Provided data that describe the stability of the salt film at low flow rates and also at high flow rates in the presence of a wide range of solar flux levels.

- Provided operational experience with the direct absorption receiver under solar flux. This gives design detail criteria for developing a direct absorption receiver.

To better understand the tests performed at the test facility, it is necessary to briefly discuss the heat transfer mechanism and the stability of the receiver film.

5.1 Theoretical Considerations on the Film

5.1.1 Heat Transfer Mechanism

In the heat transfer model developed by Wang and Copeland (1984), an implicit, finite difference scheme is used to solve the two-dimensional energy equation. For a laminar film a fully developed parabolic velocity profile is chosen (see Figure 5-1). We are incorporating a turbulence model to allow calculations to be made for the turbulent region.

The film is exposed to incident flux (in two bands split at 2 μm), which is partially reflected at the salt and air interface. The remainder passes through the film and is partially absorbed in the film (depending on the specified extinction coefficient). The fraction not absorbed is incident on the absorber surface where it is partially absorbed and partially reflected, depending on the specified optical property of the absorbing surface. Energy absorbed at the surface is reradiated and conducted back into the film. Conductive and radiative terms in the flow direction are neglected. The salt enters the top of the absorber at constant temperature, and the absorbing surface is assumed to be adiabatic. The salt and air interface exchange heat by a specified convection coefficient.

We will use this model to calculate film efficiency and an absorber-to-salt heat transfer coefficient for comparison with the ACTF data.

5.1.2 Thermal Efficiency

The numerical model described in the preceding section calculates losses from the salt film; however, it is useful to consider a model based on simple physical principles that can predict the thermal efficiency. We assume that the absorbing surface is adiabatic,
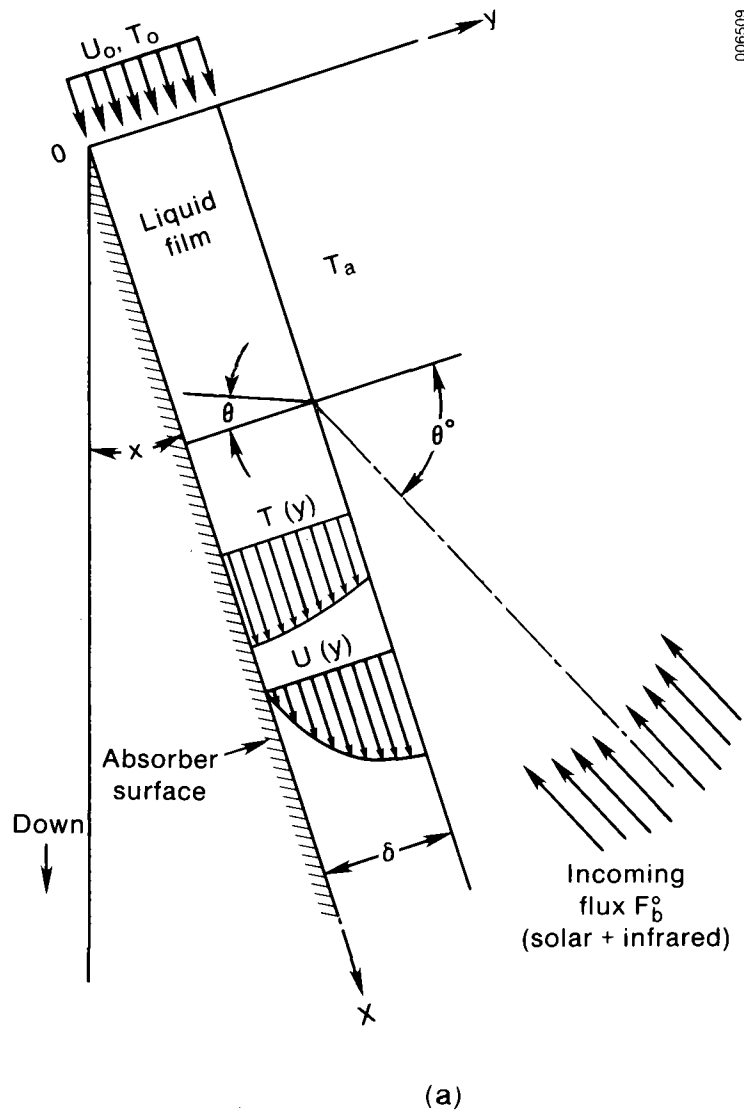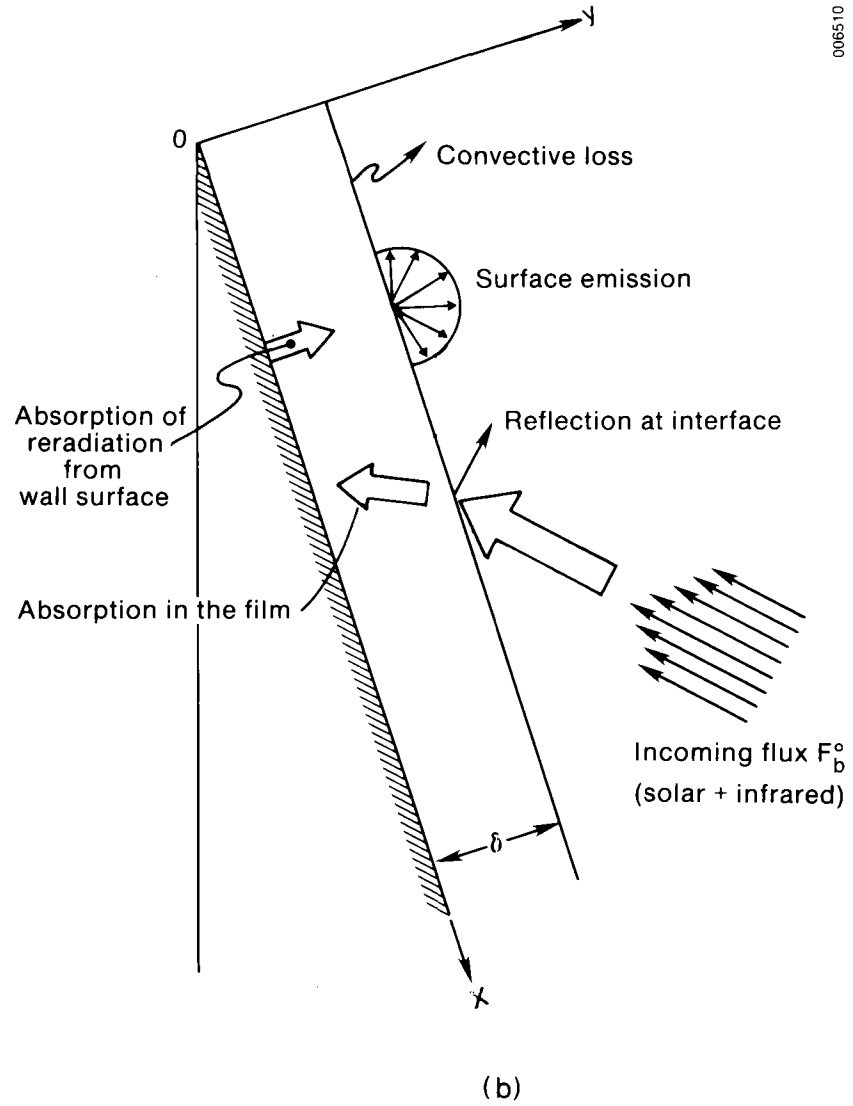
Figure 5-1. Heat Transfer Model

so the only thermal losses are from the air/salt interface. These consist of (1) incident radiation reflected from the interface, (2) convective losses to the air in the cavity, and (3) reradiation losses from the film. This can be expressed as

$$\eta = 1 - \rho_s - \frac{\epsilon\sigma\bar{T}_s^4 + h_{as}(\bar{T}_s - T_a)}{q_{in}} \,. \tag{5-1}$$

Generally, the convective loss term may be neglected. This gives

$$\eta = 1 - \rho_s - \frac{\epsilon\sigma\bar{T}_s^4}{q_{in}} \,, \tag{5-2}$$

which allows us to calculate film efficiency as a function of average salt film temperature and incident flux. Results of this model will be presented with the experimental data in Section 6.0.

5.1.3 Stability

Newell et al. (1985) discuss film stability in terms of (1) film breakdown at low flow, (2) temperature-driven instabilities, (3) gas-liquid interaction, (4) flow surface blockage, and (5) surface-pressure variations. Tests performed at the ACTF and discussed in this report were aimed at providing data to compare with the analysis of numbers (1) through (3).

5.1.3.1 Film Breakdown at Low Flow

Low flow instabilities are related to breakdown of the film caused by the liquid surface tension. This force tends to pull the film into rivulets at low flow rates. For liquids that wet the surface like molten salt, the minimum film thickness (Newell et al. 1985) is

$$\delta = 0.779 \left(\frac{\rho g^2}{15\nu^2\sigma}\right)^{-1/5} \,. \tag{5-3}$$

Since $\delta = (3\nu^2 \, Re/g \sin \theta)^{1/3}$ for a laminar film, we can express Eq. 5-3 as a film Reynolds number.

$$Re = 0.779^3 \sin \theta \left(\frac{125 \, \sigma^3}{9g \, \rho^3\nu^4}\right)^{1/5} = \Gamma/\mu \,. \tag{5-4}$$

Equation 5-4 then allows us to predict the minimum Reynolds number for stable flow. Operating below this Reynolds number should cause the film to break into rivulets. Recall from Section 4.1 that operating at 611°C during the ground tests yielded a critical Reynolds number of 15.4. If we use the appropriate properties of the carbonate salt (in Appendix D) and $\theta = 85$ deg, Eq. 5-4 predicts a minimum Re = 39.5. Thus, Eq. 5-4 appears to be conservative.

5.1.3.2 Temperature-Driven Instabilities

Temperature-driven instabilities are dry patches in the flow caused by local variations in temperature via the thermocapillary effect. This temperature variation can arise because the solar flux is distributed unevenly on the plate or because the film thickness is not uniform. Where the salt temperature rises, the surface tension of the salt decreases. In turn, the film pulls away from the hot area, causing the area to become hotter, further thinning the film until a dry area results.

Zuber (1966) developed a force balance equation that shows how the stagnation pressure of the falling film, the surface tension force, the force caused by the surface tension gradient (thermocapillary force), and the force caused by vaporization for a laminar film falling under the influence of gravity relate to each other near the upper stagnation point of a stable dry patch:

$$\frac{\rho}{15}\left(\frac{g}{\nu}\right)^2\delta^4 = \frac{\sigma(1 - \cos\theta_0)}{\delta} - \frac{\partial\sigma}{\partial T}\frac{\Delta T_f}{\delta}\cos\theta_0 + \rho_v\left[\frac{\dot{Q}/A}{\rho_v h_{fg}}\right]^2\cos^2\theta_0 \ . \qquad (5-5)$$

In Zuber's analysis the stagnation pressure tends to force the flow down the plate while the remaining forces tend to retard this force and hold the dry patch in place. The surface tension gradient is created by the difference in temperature <u>through</u> the liquid film, ΔT_f, from the solid surface to the liquid gas interface. The contribution of the thermocapillary force is such that if $\Delta T_f > 0$ (temperature decreases from the solid surface to the liquid/gas interface) the dry patch will be retarded because for molten salt, $\partial\sigma/\partial T < 0$. Note that for $\theta_0 \simeq 0$, as we expect for molten salt, the surface tension force does not affect the dry patch. The contribution of the vaporization term is about 200 times smaller than the other terms and may be neglected.

For the case $\Delta T_f = 0$, Eq. 5-5 does not agree with Eq. 5-3. This is because Eq. 5-3 was developed according to a power criterion and the first term on the right of Eq. 5-5 was developed according to a force criterion. The two equations will predict the same critical film thickness at $\theta_0 = 44.5$ deg. For low contact angles, as we expect with molten salt, the power criterion is more conservative than the force criterion. To force agreement between the two equations when $\Delta T_f = 0$ and to be more conservative (and also dropping the vaporization term), we modify Eq. 5-5 as follows:

$$\frac{\rho}{15}\left(\frac{g}{\nu}\right)^2\delta^4 = \frac{0.779^5\sigma}{\delta} - \frac{\partial\sigma}{\partial T}\frac{\Delta T_f}{\delta}\cos\theta_0. \qquad (5-5a)$$

Results are given in Table 5-1 for a range of salt temperatures, contact angles, and film temperature drops. Increasing the salt film bulk temperature allows the receiver to operate at lower flow because the reduced viscosity improves wettability. Increasing the contact angle (over the range we expect to be applicable to molten salts flowing on oxidized metal surfaces) has minimal effect on the critical flow. Increasing the film temperature drop, e.g., the flux, forces us to operate at a higher flow although the effect is weak. Since the DAR will be operated at Reynolds numbers well beyond the critical values indicated in Table 5-1, we see that Zuber's dry-out mechanism is not likely to cause operational problems.

Table 5-1. Minimum Salt Flow Due to Temperature-Driven
Instabilities

Temperature ($^\circ$C)	θ_o Contact Angle (deg)	ΔT_f ($^\circ$C)	Critical Reynolds Number	Critical Flow Rate (m^2/h)
500	10	150	26.3	0.82
600	10	150	41.4	0.73
700	10	150	58.9	0.67
600	0	150	41.4	0.73
600	10	150	41.4	0.73
600	20	150	41.2	0.73
600	10	0	37.9	0.67
600	10	150	41.4	0.73
600	10	300	44.7	0.79

In the Zuber analysis a temperature difference through the film (from the solid-liquid interface to the liquid-air interface) creates the thermocapillary force caused solely by the presence of a nonzero heat flux. Simon and Hsu (1970) analyzed the case where the temperature gradient was across the film. Such a gradient would be caused by a disturbance in the film thickness, e.g., by a wave. The results are expressed as

$$\frac{\delta_{min}}{\delta_o} = \exp\left[\frac{2\left|\frac{d\sigma}{dT}\right|q_w b^2 (x - x_o)}{g\rho k}\right] , \qquad (5\text{-}6)$$

where

δ_{min} = critical film thickness

δ_o = inlet film thickness: $(3\Gamma\mu/\rho^2 g \sin \theta)^{1/3}$

b = 100 m^{-1}, an experimentally determined constant

x = distance from inlet where critical film thickness is reached.

x_o = distance from inlet where temperature profile is fully developed, about 1 cm

This equation is valid only for flows low enough so

$$\delta_o/\delta_{min} < 2.1 .$$

The critical film thickness is to be determined from no-flux experiments. Thus, Eq. 5-6 is valid only for flow rates less than 2.1^3 = 9.3 times the critical flow. In this regime, Simon and Hsu's results show that if the flux is nonzero, the film will begin to thin out (starting at one transverse location and thinning in the flow direction) until the critical film thickness is reached, at which point the film will break up. Since we found a critical flow of 0.34 m^2/h for the no-flux case (see Section 4.1), these results indicate that any

flux will ultimately lead to film breakdown for flows less than $9 \times 0.34 = 3.1 \ m^2/h$. This is because the film is bound to exhibit waves, which are required to begin the film thinning according to Simon and Hsu's model.

For flow rates greater than 9.3 times the critical flow, roll waves periodically rewet the dry area, and as Simon and Hsu's data show, much higher flux levels are tolerable at a given flow rate. Simon and Hsu's data and correlation equations were developed only for water and water-glycerol mixtures; therefore, caution is required in predicting the behavior of molten salt films from their results.

5.1.3.3 Gas-Liquid Interaction

Gas-liquid interaction refers to the result of shear forces at the salt-air interface and becomes important for high liquid flows or for high air velocities. These forces can cause waves to form in the film's surface and possibly cause the film to eject droplets. The criterion recommended by Newell predicts critical air velocities much higher than will ever be achieved in a direct absorption receiver. However, the criterion is based on cocurrent gas-liquid flow. For counterflow or cross flow the film may be more sensitive to the shear forces. This type of interaction has not been investigated and merits further study.

Another instability related to gas-liquid interactions is the formation and growth of waves on the surface for long flow lengths. As the experimental results of Takahama and Kato (1980) demonstrate, these waves can develop for film flows of one meter or more and appear to be traveling waves that grow as they propagate downstream. At sufficient amplitude the waves may break, throwing liquid droplets from the film. Since the experimental absorber length was less than one meter, the tests at the ACTF did not explore this film instability. Note that waves developed by this mechanism can be especially sensitive to wind shear forces.

5.1.3.4 Other Film Stability Analysis

Flow-surface blockage refers to film instabilities induced by roughness elements on the absorber surface. These may occur naturally for some absorber surfaces (ceramic materials, or possibly corroded metals) or may be added to increase convective heat transfer between the absorber surface and the salt film. As Newell et al. (1985) pointed out, these raise issues of film stability and must be considered. We did not address this instability in the ACTF tests because we chose to initially investigate a smooth absorber plate.

Finally, surface pressure variations are concerned with how the liquid flow distribution in the film may be affected by airstreams normal to the salt film. An example of such a disturbance would be wind incident on an external DAR. This instability was not considered experimentally, but Anderson (forthcoming) has investigated the applicable literature.

5.2 Test Plan

The complete test plan as originally conceived is given in Appendix B. The six tests are described briefly as follows.

Test 1. No-flux test. Establish salt flow and see that test loop (with cavity) and instrumentation behave as they did on the ground. Roughly determine cavity heat losses and reliability of salt inlet and outlet thermocouples.

Test 2. Flux ramp test. Operate with solar flux for the first time. Bring up flux slowly and observe absorber flow and temperatures.

Test 3. Flux map test. Determine if the fixed and movable flux transducers still show that the variation of flux across the absorber plate is negligible.

Test 4. Film stability and transition/IR-solar split/film efficiency. Check film behavior under solar flux as the flow rate is reduced from turbulent to laminar flow. Determine the fraction of calorimeter output attributable to long-wave and short-wave energy. Determine thermal efficiency of salt film from 500° to $750^{\circ}C$ average film temperature.

Test 5. $900^{\circ}C$ test. Ramp the salt outlet temperature up to $900^{\circ}C$. Determine salt-film thermal efficiency for average film temperatures from 750° to $800^{\circ}C$.

Test 6. Low flow stability. Decrease flow with reduced flux towards dryout flow rate observed on ground. Determine if presence of flux increases the minimum flow.

These tests bring up the operation of the test loop conservatively so the most severe test conditions occur towards the end of the test, increasing the likelihood of getting useful data.

In addition to the test plan, Appendix B also includes the daily log of test results to aid in interpreting results presented in this and in the next section.

5.3 Tests 1, 2, and 3

The first test checked out the operation of the test loop after it had been lifted to the top of the tower and before applying solar flux. During this test period, we checked out the operation of the cavity-flux redirector, ensured that the absorber salt inlet and outlet thermocouples were reliable and accurate, checked out flow control from tanks 1 and 2, and determined the cavity heat loss.

Test 2 provided the first solar flux on the absorber. During this test the solar flux was gradually increased by bringing different sections of the mirror field in focus. This test was about half completed on October 25, and the remaining half was completed on November 5. The order in which mirror groups were brought on-line is given in Figure 5-2. The initial group, denoted as I, provided flux levels on the order of $5-10$ W/cm^2 (50-100 suns). As the additional groups were brought on line, the peak flux as measured by the fixed flux tranducers increased to the 50-60 W/cm^2 range. This part of test 2 was carried out at a fairly high flow rate, 10.4 m^2/h, to ensure adequate cooling of the absorber plate.

The second part of test 2 was intended to verify that at low flows (laminar regime) the film was still stable and therefore the rest of the test plan could be carried out successfully. To do this we decreased the flow to 4.46 m^2/h but immediately detected the formation of a dry spot on the plate accompanied by a large temperature excursion ($180^{\circ}C$ higher than a probe located at the same vertical location on the plate but on the plate centerline in a wetted region). This result was unexpected (since we had seen film instabilities only with flows as low as 0.34 m^2/h in the ground tests) and strongly influenced the remainder of the test program. Basically, we eliminated tests 5 and 6 since they involved low flow rates, and modified test 4 so to focus more on investigating this dryout phenomenon.

Note: Number of mirrors = 543
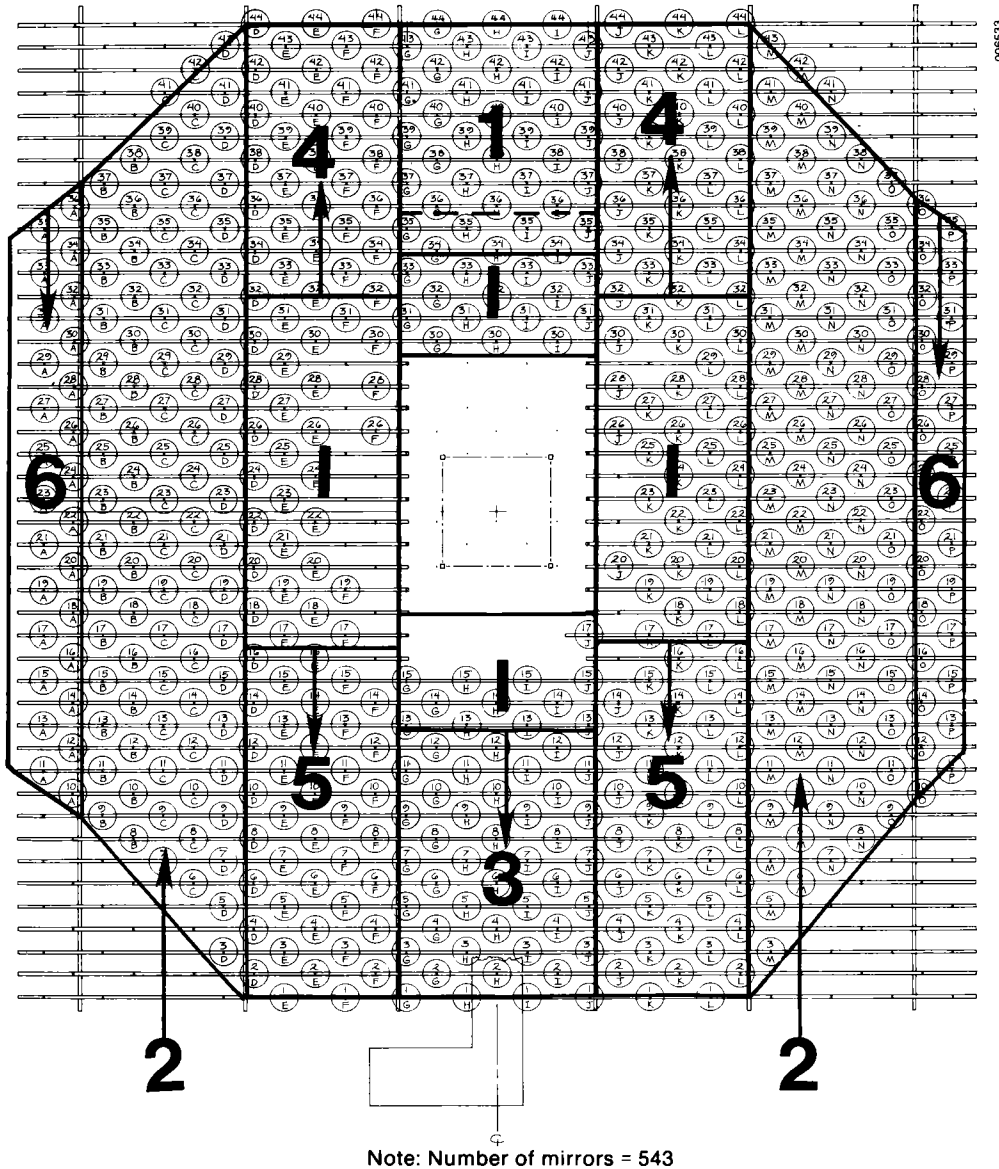
Figure 5-2. DOE ACTF Mirror Field Configuration

Test 3 was carried out as planned and included tests early in the day, near solar noon, and late in the day in which we passed the scanning flux rake down the absorber and took measurements at the level of each fixed flux transducer. During these tests, the output of the fixed transducers was significantly lower than the rake transducers for two reasons. First, the rake transducers were several centimeters closer to the cavity center and were exposed to higher flux. Second, the fixed transducers were exposed to the water-cooled rake. Results (Figures 5-3a,b and 5-4) show that the standard deviation of the flux variation horizontally across the absorber was about ±8% at noon (Figure 5-3a) and slightly larger early in the morning (Figure 5-3b) and presumably late in the day.

The variation vertically was much larger, nearly a factor of two (see Figure 5-4). This means that the 10 fixed-flux transducers could be trusted to provide a good indication of the flux distribution because the important flux variation was vertical, not horizontal. A variation in the vertical flux distribution is not important because the fixed transducers

(a) Morning

(b) Noon
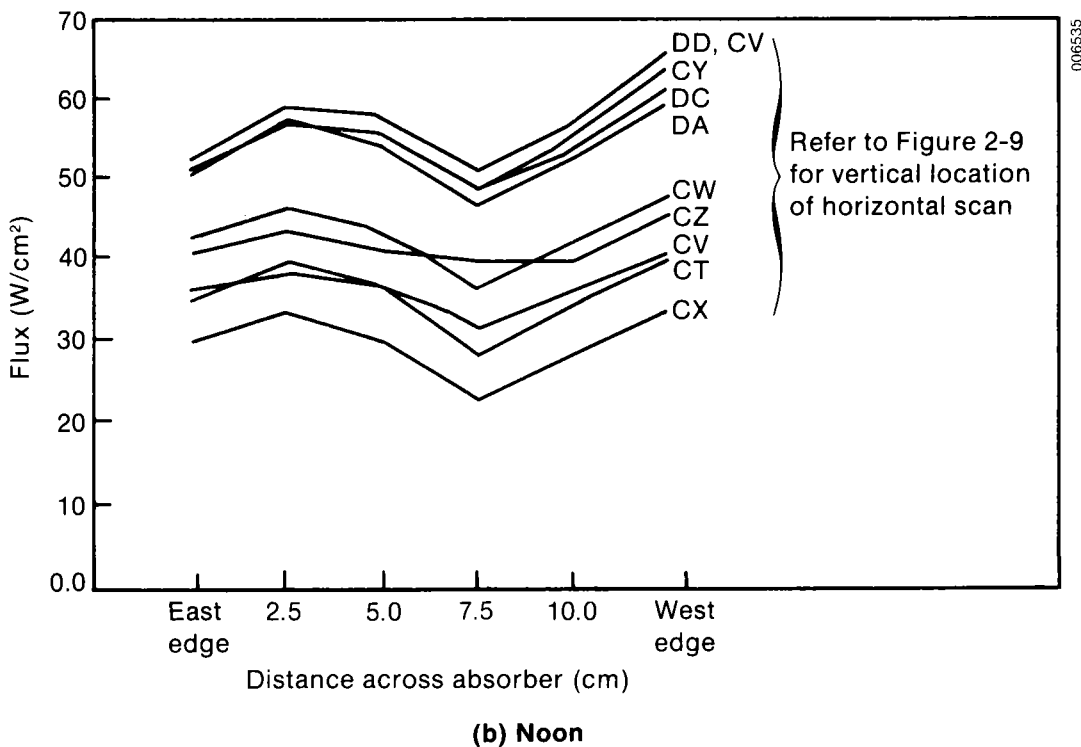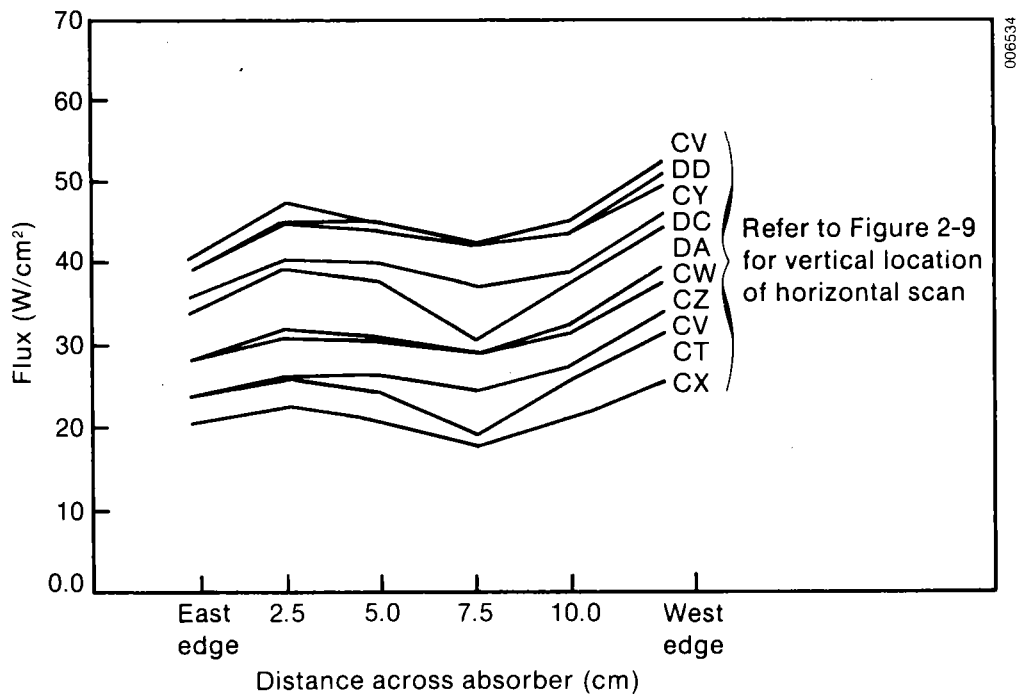
Figure 5-3. Flux Rake Data for Morning and Noon
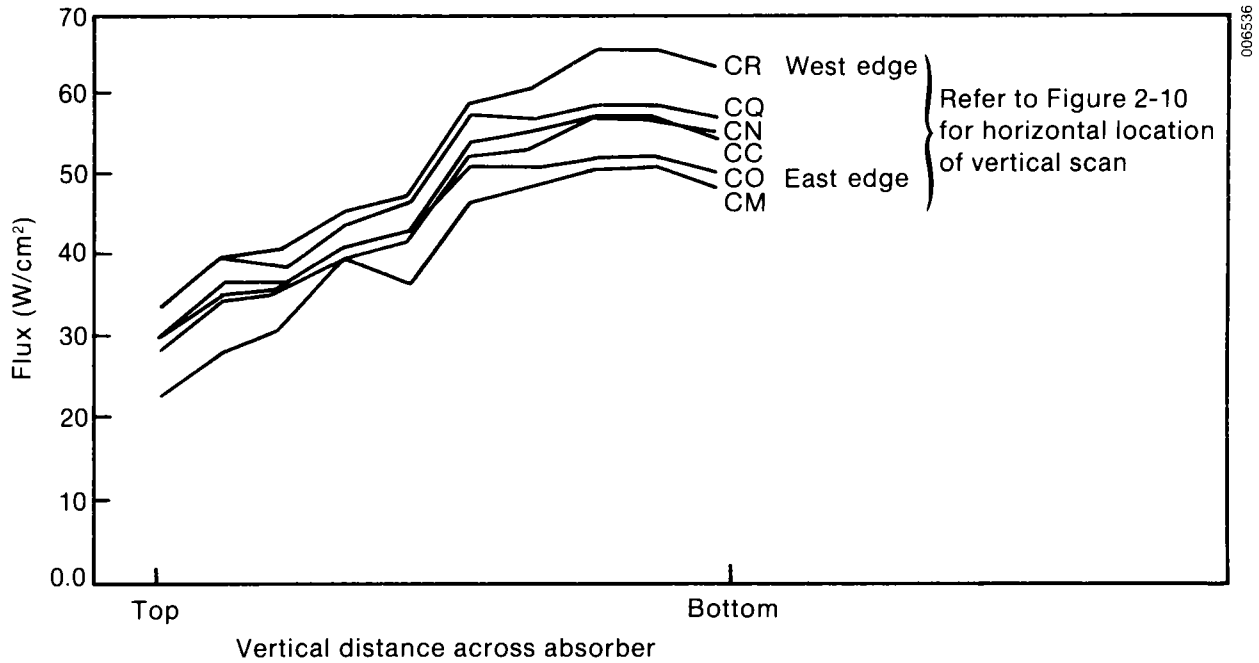
Figure 5-4. Cross Plot of Noon Flux Data, Vertical Distribution

are orientated vertically. A substantial horizontal variation would have been a problem because it would have required that we pass the flux rake in front of the absorber every time we needed incident flux data.

To provide flux distribution input to the analytical model, we simplified the distribution in Figure 5-4 for the west edge of the absorber plate into a three-segment linear curve fit shown in Table 5-2. This distribution was then multiplied by a specified peak flux to produce a dimensional flux distribution and was further divided into the long-wave and short-wave contributions by a procedure described in Section 6.0.

To develop a flux distribution needed for reducing the experimental results (heat transfer and efficiency data), we related the output of the flux rate to transducer CU (see Figure 2-9). Since the rake was located out of the absorber plane, we first determined the ratio of the flux in the absorber plane to that in the rake plane:

$$\frac{q_{cu}}{q_{rake,cu}} = \frac{52.9}{56.2} = 0.94 \ ,$$

where q_{cu} is the output of fixed transducer CU before the rake is inserted into the cavity, and $q_{rake,cu}$ is the average of all six flux transducers when the rake is at the height of transducer CU.

41

Table 5-2. Three-Segment Linear Curve Fit

Dimensionless Distance from Top of Absorber	Dimensionless Flux
$0 < x/L < 0.47$	$0.51 + 0.47(x/L)$
$0.47 < x/L < 0.78$	$0.73 + 0.87(x/L - 0.47)$
$0.78 < x/L < 1.0$	1.0

We then perform an area-weighed average of the rake output for the entire vertical scan, giving $\bar{q}_{rake} = 44.6$, and derate this to the absorber plane by $0.94 \times 44.6 = 41.9$. We then have

$$\frac{\text{average flux on absorber}}{\text{output of transducer CU}} = \frac{41.9}{52.9} = 0.793 \, .$$

Incident energy on the absorber is then

$$q_{in} = q_{cu} \times 0.793 \times 15.2 \text{ cm} \times 60.1 \text{ cm} = q_{cu} \times 736 \text{ (watts)}.$$

Repeating this procedure for the morning flux scan, we find the same results within an experimental error of about 5%. We did not have sufficiently high flux levels during the afternoon flux scan to carry out this procedure.

For local heat transfer coefficient measurements, local flux was determined by the vertical flux profile seen in Figure 5-4. This profile was normalized to 1.0 at the height of transducer CU.

6.0 ANALYSIS OF TEST RESULTS

As mentioned in Section 5.0, test 4 provided the bulk of the test data, including data that support

- Separating the relative contributions of infrared and solar wavelengths to the flux incident on the film
- Calculating thermal efficiency of the film
- Calculating heat transfer from absorber to film
- Determining film stability at various flow rates.

Appendix G presents all experimental data used in the following discussions in tabular form.

6.1 Separating Long- and Short-Wavelength Contributions

This experiment allowed us to separate the flux incident on the film into the long- and short wavelength components. This information is needed in the numerical heat transfer model and was measured in the following way. We achieved steady conditions at a given salt-inlet temperature (500°, 600°, and 700°C) with solar flux and then closed the shutters. Since this removes the solar wavelength contribution, the flux transducers' response after closing the shutters is proportional to the infrared flux incident on the film because of reradiation from the cavity walls. We reduced the data by fitting the best (in a least-square error sense) exponential curve of the form:

$$q_{IR}(t) = q_{IR}(o) \, e^{-t/\tau} , \tag{6-1}$$

to the flux transducer output after the shutter closing. We then extrapolated it back to the instant when the shutters were closed (at t = 0) to determine the infrared contribution just before the shutters were closed. A typical plot of the flux transducer output during this period is shown in Figure 6-1. Only data just after the vertical line in Figure 6-1 were included in the curve fit. Thus we are assured that the flux transducer output was not partly caused by solar flux. Results of the curve fit are given in Table 6-1.

The data suggest that a reasonable average is 0.12 for the fraction of total incident energy that is in the long wavelengths, >2 μm. Obviously, operating at higher temperatures would increase this fraction, but for the relatively narrow range of 500°-700°C this value seems appropriate. This value, 0.12, was used in the model for all calculations of the film efficiency and heat transfer.

6.2 Thermal Efficiency of the Film

We experimentally determined the thermal efficiency of the film by measuring how much heat was absorbed by the salt and dividing it by the energy incident on the film according to

$$\eta = \frac{\dot{m}_s C_s \, (T_{so} - T_{si})}{q_{in} A_{active}} . \tag{6-2}$$
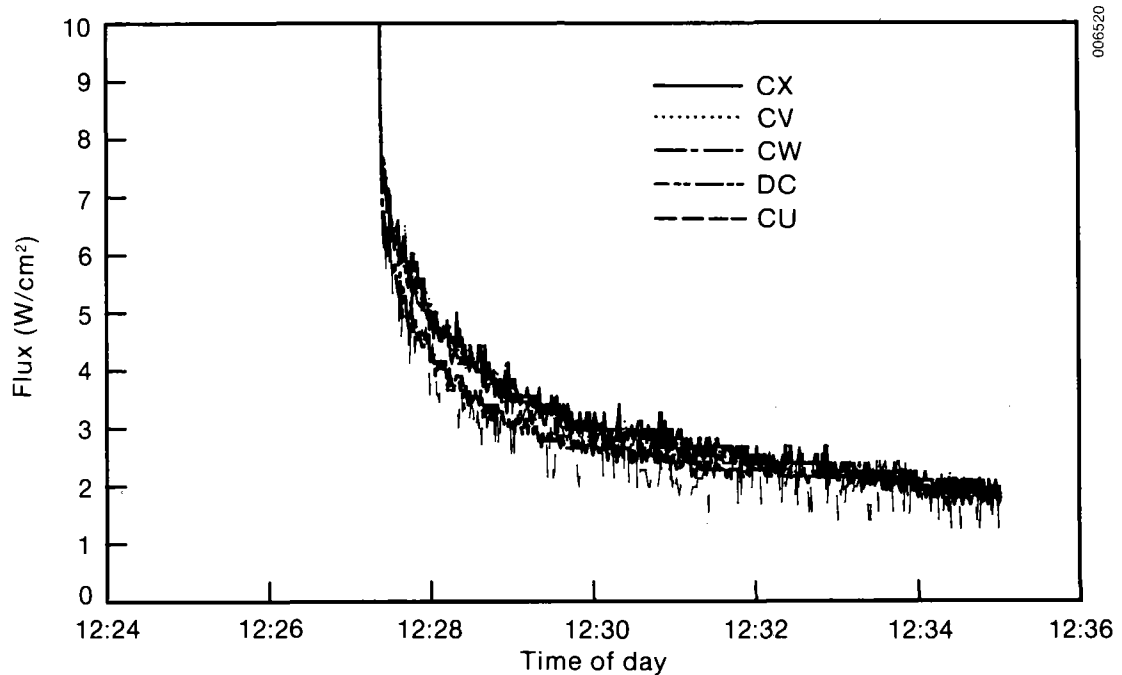
Figure 6-1. Typical Flux Transducer Output during Closed-Shutter Test (11/6/85)

Table 6-1. Relative Contribution of Long and Short Wavelengths to the Flux Incident on the Absorber

Date	Time	Salt-Inlet Temperature (°C)	Total Flux (W/cm²)	Infrared Flux	Infrared/ Total Ratio	RMS Variance of Curve Fit (%)
11/6/85	11:28	600	47.2	4.9	0.103	10.3
11/6/85	12:26	600	54.1	6.0	0.112	6.4
11/6/85	15:01	600	35.8	4.1	0.115	5.7
11/8/85	12:35	500	56.9	6.7	0.118	3.7
11/9/85	12:20	700	48.5	8.0	0.165	2.2
11/9/85	13:20	700	51.2	6.6	0.129	2.6

For a complete discussion of experimental errors, see Appendix F. We noticed that the major contributor to experimental errors, especially in measuring the film efficiency, was unsteadiness, which is inherent in testing under actual solar conditions. As a result, we carefully screened efficiency data and found six data points with an adequate confidence level. These are presented in Figure 6-2 along with results of the numerical model and the simplified model presented in Section 5.1.2. For the simplified model we used a reflectance of 0.06 per Jorgensen (1985), and an emissivity for the salt film of 0.90. Data are presented with flux as a parameter, and one can see that the simplified model is more conservative than the numerical model, generally lying about 4 percentage points below the numerical model. The numerical model should agree with the simple
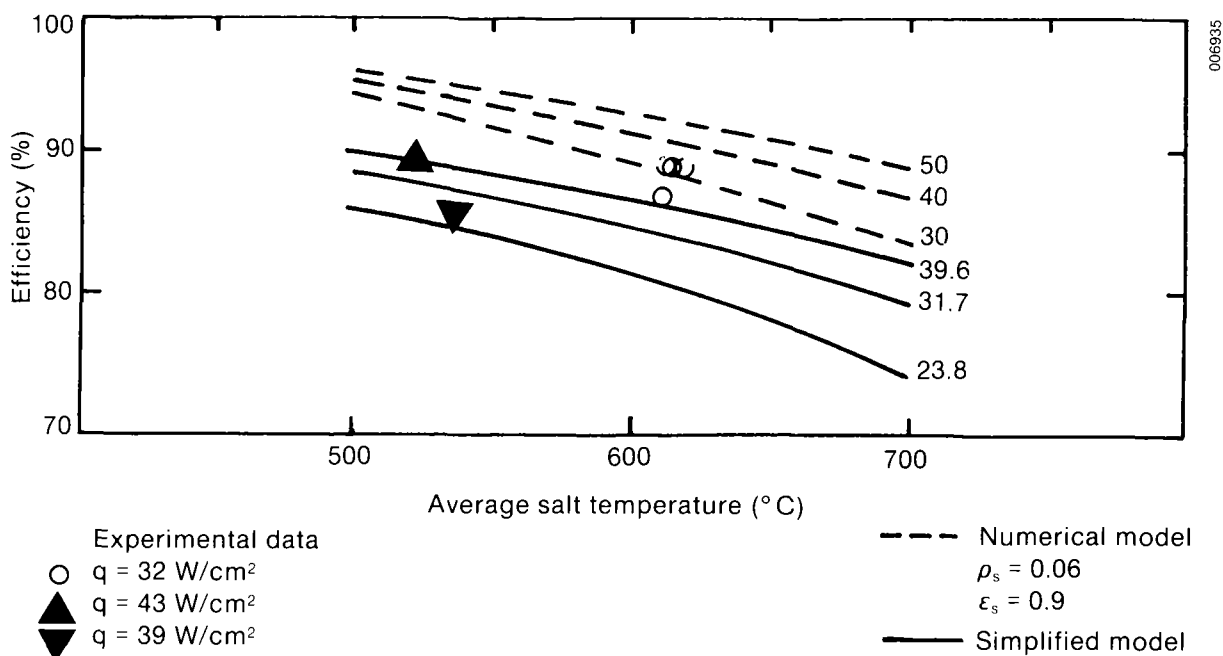
Figure 6-2. DAR Film Thermal Efficiency

model, but because the losses are small, numerical errors of a few percentage points amplify the calculated losses, which are relatively small. The experimental data at both 500° and 600°C agree quite favorably with the simple model, generally within about 4 percentage points.

Using the simplified model, Eq. 5-2, as a guide, the behavior of the film seen in Figure 6-2 can be explained. Losses from the film are essentially incident energy at the solar wavelengths reflected at the salt/air interface and reradiation from the film. The latter increases with increasing film temperature, thereby reducing efficiency. Increasing the flux at a fixed film temperature also reduces the efficiency according to Eq. 5-2 because the reradiation losses are relatively smaller.

6.3 Heat Transfer from the Absorber to the Film

Of primary concern here is the difference in temperature between the flowing salt film and the absorbing surface. This quantity is quite sensitive to the transmissivity of the salt film and the wavelength distribution of the flux because they determine how much energy is absorbed in the film versus how much is absorbed on the absorber surface and subsequently transferred to the salt.

We quantified this effect by plotting the dimensionless heat transfer coefficient $(h/k)(v^2/g)^{1/3}$ against the film Reynolds number $4\Gamma/\mu$. The local heat transfer coefficient is determined from the experimental data by

$$h(x) = \frac{\rho_s q(x)}{T_s(x) - T_a(x)} . \tag{6-3}$$

45

The local flux was determined as described in Section 5.3. Local salt temperature was determined from

$$\frac{T_s(x) - T_{si}}{T_{so} - T_{si}} = \int_{inlet}^{x} q(y) \, dy \, . \qquad (6-4)$$

The heat transfer coefficients were determined at locations of absorber plate thermocouples A, B, D, F, H, I, J, K (see Figure 2-6). See Appendix F for a discussion of experimental errors. We excluded experiments in which the salt flow was less than 7.5 m^2/h for reasons explained in Section 6.4.

Results for local heat transfer for one run are shown in Figure 6-3. Clearly, there is a fairly long thermal entry region, ~ 0.4 m. Inlet heat transfer coefficients (measured near thermocouple A) in the example in Figure 6-3 are about 7500 W/m^2 ^{o}C.

For the average dimensionless heat transfer coefficient, we use the local heat transfer at thermocouple I, J, K, which corresponds to the furthest downstream data point in Figure 6-3 and appears to be in the region of thermal equilibrium. Property values were determined at the mean salt temperature. Results for all runs, grouped by Prandtl number, and those of the model are shown in Figure 6-4.

For the analytical calculations of the heat transfer coefficient, we first used the optical density for the salt film calculated from data by Jorgensen et al. (1985) but found that this optical density (extinction coefficient, 1140 m^{-1}) was very high (a solar absorption >60%) and analytical results were unreasonable. Therefore, we ran the model at several optical densities (25, 50, 100, 500, and 1000 m^{-1}). We chose 100 m^{-1} as the most reasonable because it is equivalent to a solar transmission of about 85%, which seems reasonable for the nominally transparent salt. Until more experimental data are available on the optical density of molten salts, the value of σ used in our analytical model cannot be better defined. If we have overestimated σ, the calculated heat transfer coefficient will be too high and vice versa. The value of ρ_s is 0.06 from Jorgensen et al. (1985) in Eq. 6-3. This is the solar-weighted hemispherical reflectance of a 0.64-mm-thick layer of molten carbonate salt on oxidized Inconel 600. We used an emissivity of 0.90 for the absorber plate, which is oxidized Inconel 600.

Also shown in Figure 6-4 are data from Wilke (1962) for several Prandtl numbers in the turbulent region and two models for the laminar region. The first laminar model is by Seban and Faghri (1976) for laminar films. Wilke's turbulent data are for falling water and water-ethylene glycol mixtures on the exterior of a vertical tube. The low end of Wilke's data depicts the departure from laminar flow based on his observations of the departure of the heat transfer data from laminar behavior. The second model is our numerical model that gives virtually identical results to the Seban and Faghri curve.

Although our experimental data are for Reynolds numbers well into the turbulent region, they appear to closely follow an extrapolation of the laminar curves. This behavior is consistent with our visualization of the film. With the carbonate salt we always observed what appeared to be a laminar film. By testing with nitrate salts (which allow higher Reynolds numbers due to a lower viscosity, 1.14 cp vs. 13.30 cp at 550°C), we observed what appeared to be intermittent turbulent flow on the absorber panel in the range of Reynolds numbers (4Γ/μ) from 4880 to 17,224. At the lower end of this range (which lies just beyond the upper end of our data in Figure 6-4), intermittent turbulent spots
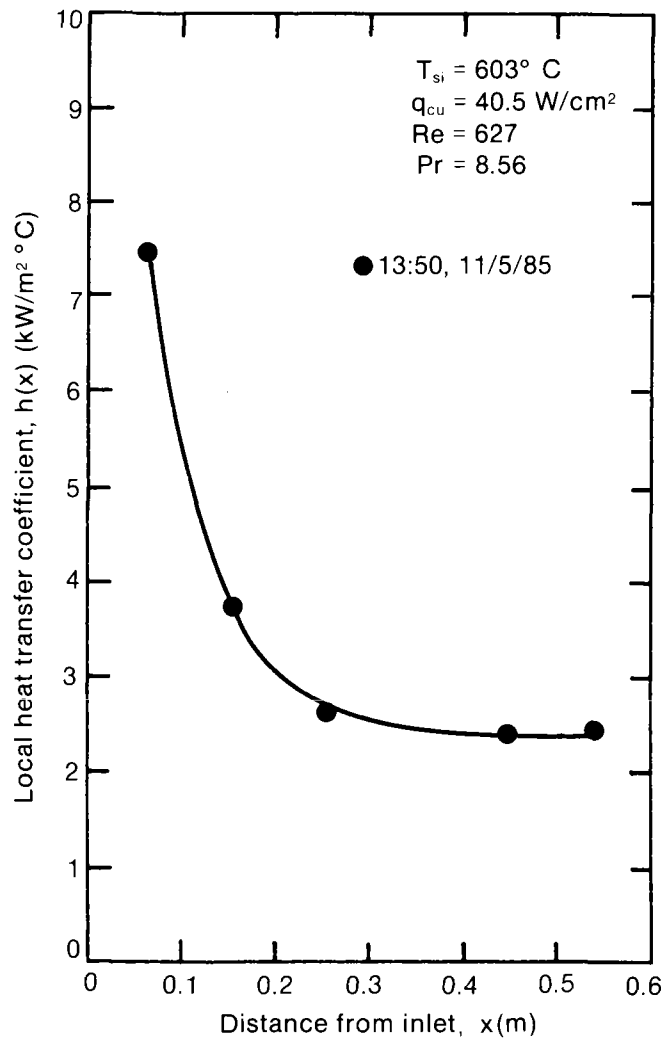
Figure 6-3. Local Heat Transfer Coefficient in Absorber

appeared at the lower end of the absorber plate. As the Reynolds number increased, the turbulence appeared more consistently and higher up the plate. Thus, a finite panel length is required before fully turbulent flow can develop, and the data in Figure 6-4 are for laminar flow.

For a commercial operation, if the flow is in the fully turbulent region the heat transfer coefficients would be much higher (~9000 W/m^2 $^{\circ}C$); i.e., for a given flux the absorber temperature would be much closer to the local salt temperature. For a doped salt, the concept of heat transfer coefficient loses meaning because the flux is absorbed volumetrically. The effect is the same as a large heat transfer coefficient in that the absorber plate can be made to operate at a temperature much closer to that of the salt. Note also that operating in the turbulent region may be desirable even for a doped salt because the thicker film increases the optical path length.
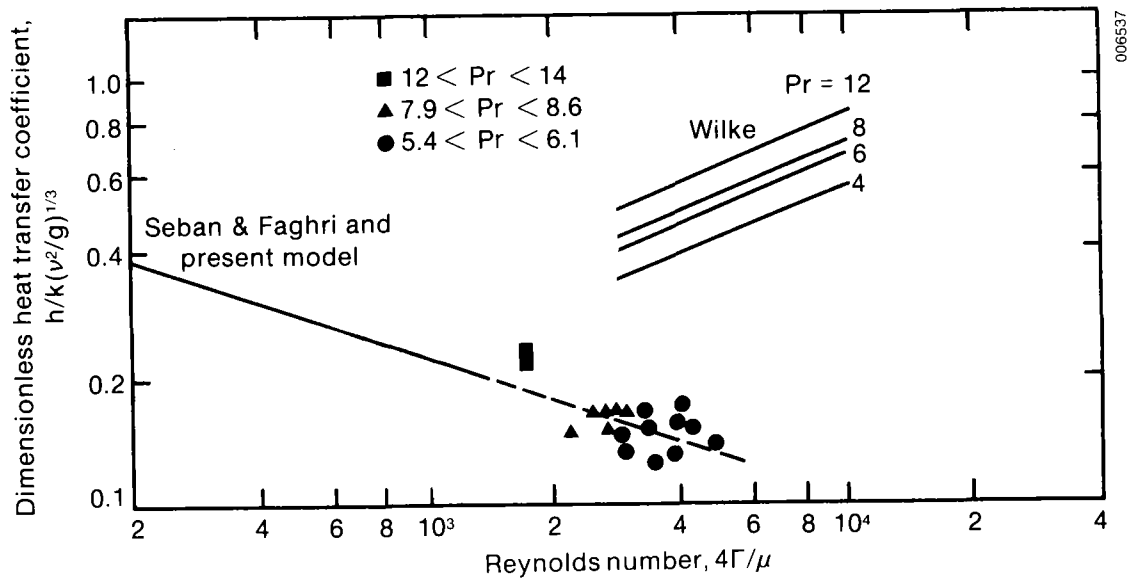
Figure 6-4. Dimensionless Heat Transfer Coefficient (Salt/Absorber) versus Reynolds Number

6.4 Salt-Film Stability

As discussed previously, one of the important purposes of this test program was to determine if the salt film was stable over the range of flow rates anticipated for the DAR concept. (By "stable" we mean a condition in which the salt film uniformly wets the absorber panel.) Roughly speaking, this range is from 14.9 m^2/h at the high end down to below 3.7 m^2/h. The upper range corresponds to a full-power, direct absorption receiver operating in turbulent flow. The lower end of the range corresponds to a smaller receiver operating with a turn-down factor of 3 or possibly 5 and would be in the laminar-flow range. As discussed in Section 4.0, we achieved stable flows in the absorber of flux as low as 0.34 m^2/h on the absorber panel. This can be compared with Table 5-1, which shows the minimum stable flows caused by surface tension and thermocapillary effects. Consistent with results discussed in Section 5.0, we did not experience any salt film instability in the high-flow regime.

The theoretical results in Section 5.0 for low-flow stability indicate that under solar-flux conditions of 50 W/cm^2 (corresponding to a salt-film temperature drop of about 150°C), flow rates as low as 0.67 m^2/h should be stable. Experimentally, we found that flow rates below about 10.4 m^2/h produced what appeared to be a local dry area on the plate and local overtemperatures. Appendix D contains detailed test notes that discuss the dry area formation. Briefly, the dry area began to form as the flow decreased to below 10.4 m^2/h in the shape depicted in Figure 6-5. The film in this wing-shaped area appeared to gradually thin with decreasing flow, and the wing-shaped area widened slightly. At about 4.53 m^2/h the area appeared to be completely dry, and we observed foaming and bubbling at the interface between the film and the dry area.

We quantified the development of the instability by normalizing the temperature measurements depicted in Figure 6-5 according to

$$\theta_k = \frac{T_{19K} - T_{so}}{T_{19I} - T_{so}} \text{ and}$$

$$\theta_f = \frac{T_{19F} - T_{si}}{T_{19D} - T_{si}} , \qquad (6-5)$$

and by plotting this normalized temperature difference against the film Reynolds number Γ/μ. This normalization essentially removes the effect of flux as a parameter. When the normalized temperature is unity, the temperature on the absorber panel is symmetrical; that is, T19K = T19I and T19F = T19D. As the dry area begins to form, T19K rises above T19I, and as the dry area expands, T19F rises above T19D. Results are plotted in Figure 6-6.

Clearly depicted in Figure 6-6 is a critical Reynolds number of 1000. At higher Re the normalized temperatures are both very close to 1. The data at Re = 1000 show that θ_f is close to 1 but θ_k is about 1.25. Just below Re = 1000, the θ_k rises very quickly to nearly 2.0 and the θ_f rise to around 1.25. Below the critical Re, there is a rough correlation between flux and normalized temperature, but the behavior in this region is erratic. Note also that in this region there are virtually no θ_k points less than 1.25. This indicates that even at low flux levels, the dry area formation is still a problem, which is consistent with our observations during testing. This instability occurs at a flow rate 15 times greater than that predicted by Eq. 5-5. However, Simon's and Hsu's model more nearly predicts the observed dry area formation.

Recall that Simon's and Hsu's results show that any nonzero flux will eventually lead to dryout. One must then ask whether this mechanism is not responsible for the dryout we observed. Again, since their data are based on water and water-glycol mixtures, extrapolation to molten salt is tenuous. However, using the water data (for
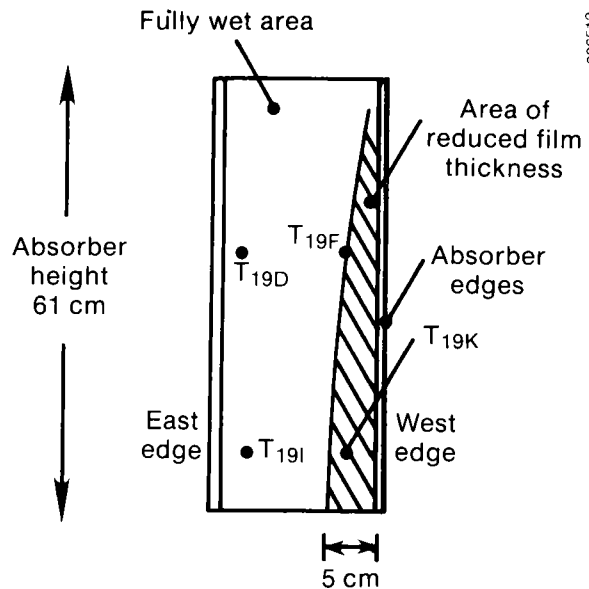
Figure 6-5. Plan View of Salt Film on Absorber Showing General Shape of Dry Area and Thermocouple Locations

which the Kapitza number matches much more closely than does the water-glycol data), it is possible to calculate the Reynolds number that would lead to the formation of a dry area within a given downstream distance in the presence of a given flux (see Table 6-2).

We had to choose between the water and the water-glycol data because these Reynolds numbers are all in the roll-wave region, where Simon and Hsu were not able to develop a fluid-independent correlation as they did in the capillary wave region.

Table 6-2. Reynolds Number for a Given Distance (Flux = 0.5 × 10^6 W/m^2)

Distance (cm)	Re
0.10	349
0.15	576
0.20	950
0.30	2591

49

$$\nabla = \frac{T_{19K} - T_{so}}{T_{19I} - T_{so}} \qquad \bullet = \frac{T_{19F} - T_{si}}{T_{19D} - T_{si}}$$
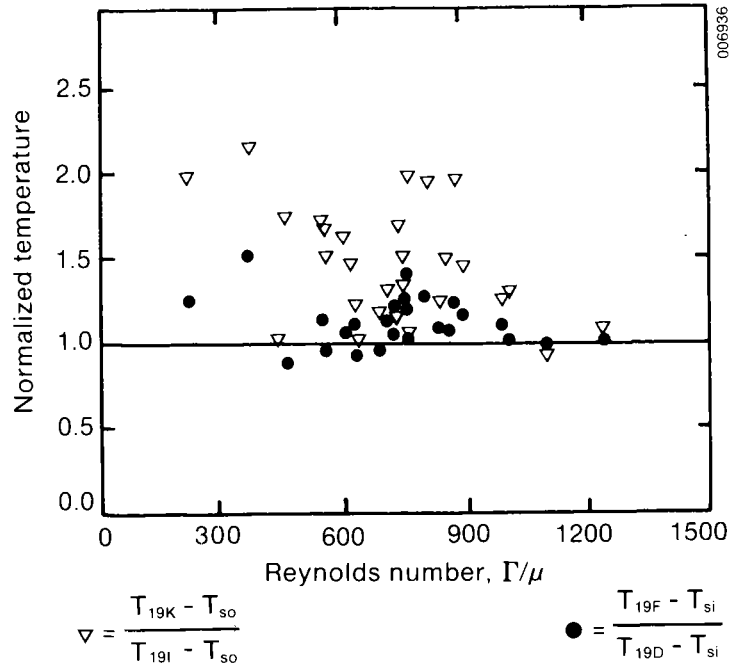
Figure 6-6. Absorber Overtemperature versus Reynolds Number

Simon's and Hsu's analysis therefore predicts that a film with a flux of 0.5×10^6 W/m^2 and a Re = 950 will form a dry area 20 cm downstream from the place where the flux begins. The dry area we observed appeared to begin somewhat higher, implying a lower critical Reynolds number. Nonetheless, the result from Simon's and Hsu's analysis is not so far from what we saw, especially considering that their data were based on water.

Some of our observations of the dry spot formation bear discussion. First, as described earlier, the wing-shaped area we saw was not always totally dry. It first appeared as an area of slightly reduced film thickness (of nearly the entire absorber length), which became thinner as the flow was decreased. This is inconsistent with Simon's and Hsu's analysis, which is based on a gradual thinning of the film in the downstream direction until the critical film thickness is reached, followed by dryout. Upon increasing the flow again, we saw the dry area move downstream to the bottom of the plate before totally disappearing. This observation of rewetting is consistent with their mechanism because increasing the flow should push the point downstream where dryout occurs. Although the dryout mechanism of Simon and Hsu shows some consistencies with our observations, other factors that could cause the dryout require discussion.

An important question is whether the effect is real or whether it is an experimental artifact. By this we mean that the effect could be caused by the apparatus design, its operation, etc., and not a problem inherent in the direct absorption concept. We felt that the most suspect design feature was the absorber edge. Recall that the edges were exposed to flux and that a substantial surface area of edge was provided to ensure that we could contain the salt during ground tests. During these tests, we observed that salt would completely wet the inner surfaces of the edges (for flows above 7.5 m^2/h) but would not crawl over the edges. The design appeared to be successful on the ground since it contained the highest flow rate we ran, but we observed a completely different behavior under solar-flux conditions.

Close observation of the inner surface of the absorber edges under flux showed that these surfaces were completely dry. The salt could not wet the surface so it formed a meniscus at the junction of the absorber and the edges, e.g., a large contact angle. This observation is depicted in Figure 6-7. Although we have not analyzed this behavior in detail, we can hypothesize the following explanation for it and how it relates to the formation of the dry spot on the absorber.

The film we observed on the edges during the ground tests is very unstable. It exists only because the wetting action (creep) of the salt pulls a thin film up the edge, to some extent against gravity. As soon as a substantial flux falls on the edge, the film thins further as the viscosity decreases and the edge temperature increases, further decreasing the viscosity and film thickness. The observed critical flow in Figure 6-6 is consistent with this argument because we did not observe full wetting of the edges (during the no-flux ground tests) until flow rates were above 7.5 m^2/h (see Figures 6-7a and 6-7b).

Eventually the edge becomes dry with no way to dissipate the flux impinging on it, causing the temperature to rise dramatically. Our observation of the edge with flux showed (Figure 6-7c) that the salt has a strong aversion to wetting when the edge is so hot, increasing the contact angle dramatically. This could be because of the high temperature or possibly a change in the chemistry of the edge material (e.g., corrosion) at the high temperature. Data on the effect of temperature on contact angles are minimal (see Moiseev et al. 1967) so we cannot definitely attribute this behavior to any given phenomenon. However, we clearly observed a very large contact angle. How this dry edge contributed to the dry area forming on the absorber is subject to further investigation, but certainly this peculiar behavior at the very location where the dry area formed is suspicious.

(a)

(b)

(c)
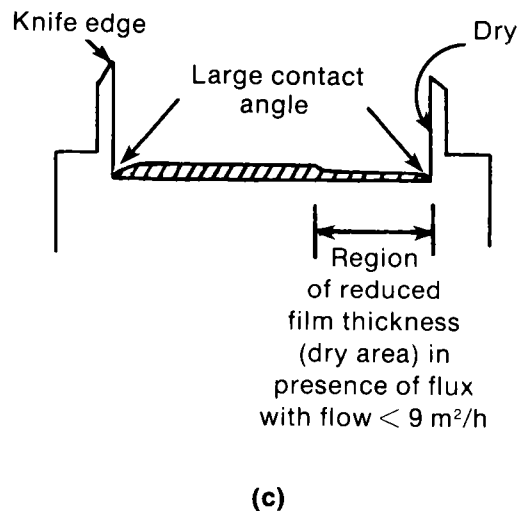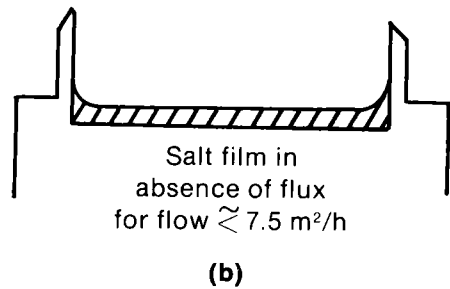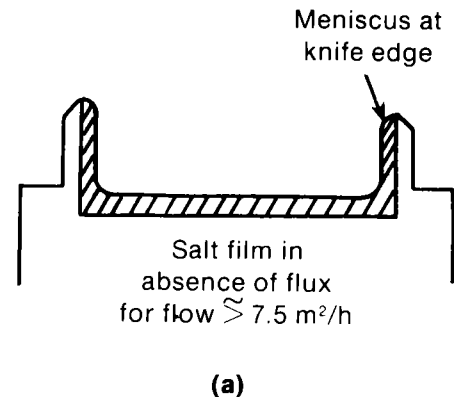
Figure 6-7. Cross-Sectional View of Salt Film on Absorber Showing Dry Area

51

The absorber dry area could be a result of heat transfer from the very hot edges or from the film gradually receding from the absorber-edge interface, where we observed the large contact angles caused by the slightly higher flux on the west edge of the absorber, etc. We never observed a similar dry area on the east edge and cannot give a satisfactory explanation as to why. We did observe a slightly darkened area where the dry area was the same shape as the dry area. This likely happened after the first dry area was formed because of oxidation. Subsequent dry-area formations tended to favor this side because of the higher solar absorptance by the absorber plate. It is possible that a slight flow imbalance (caused by the weir not being perfectly level or by absorber warpage) could precipitate the formation of the dry area on one side. However, as described in Section 4.1, the weir was carefully leveled before the ground tests and again just before the tower tests.

We performed two experiments to determine what caused the dry area to form. First, we fabricated a ceramic insulation to protect the outer surface of the absorber edges (Figure 6-8). This partially shaded the edges from flux so they would operate at lower temperature. The ceramic material was a series of high-temperature electrical insulators. Since these were not of especially high-purity ceramic, we noticed some degradation and discoloration. However, they did last long enough to complete the test.

Although we noticed that less smoke was produced with this edge protection, the dry area still formed, and we observed an overtemperature of about 80°C at 7.5 m^2/h and a flux of 47 W/cm^2. A crude thermocouple under the ceramic shield indicated that the temperature of the edge reached 900°C or greater. Since we were not able to shade the inner surface of the edge, we cannot be sure that this would not have completely eliminated the dry area. We can say only that shading the outer surface of the edge reduced the overtemperature.

Next, we moved the solar beam approximately 15 cm to the east to even out the flux. This decreased the flux on the lower west edge from about 45 to 28 W/cm^2 while the flux
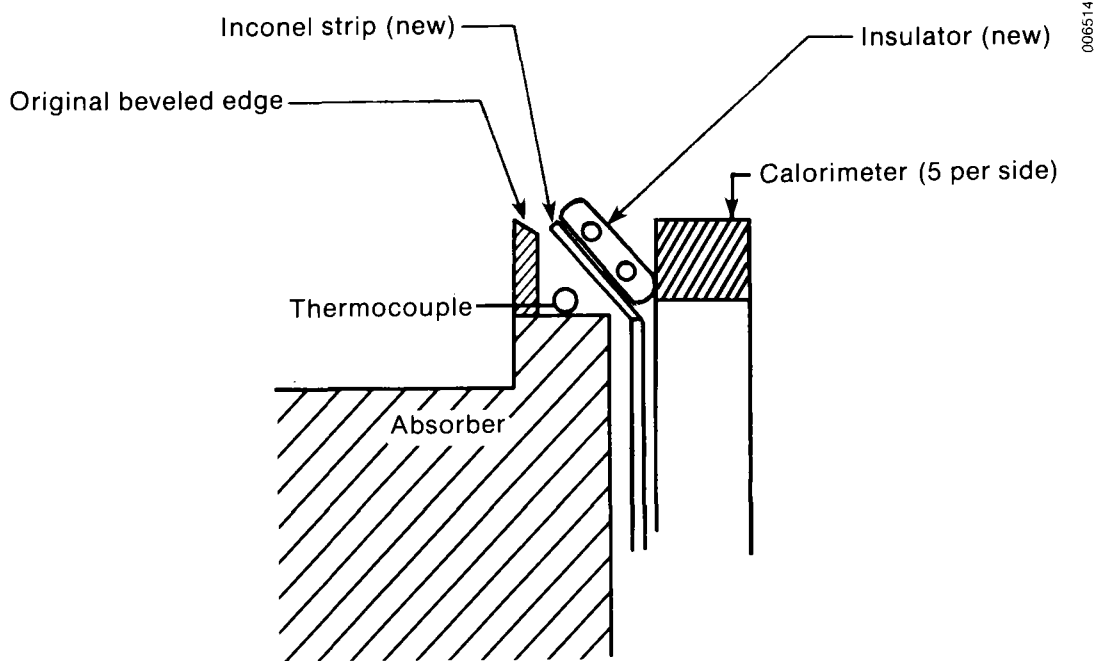
Figure 6-8. Ceramic Edge Protection

on the lower east edge remained near 40 W/cm^2. The overtemperature decreased from about 80° to 59°C but definitely did not decrease further, nor did the dry area disappear or form on the east side. Thus, flux imbalance does not explain the dry area.

Although we were not able to perform definitive tests to prove the source of the dry area, our experience indicates that it would not occur if the edges were protected better. As previously discussed, we believe that the most likely cause of the dry area is insufficient wetting of the edges at flows below 7.5 m^2/h that subsequently caused these edges to dry out. This apparently leads to the salt film thinning and gradually receding from the junction of the absorber and the edge because of surface tension gradients and the apparently very high contact angle that prevents the salt from wetting the edge. This point needs to be checked with further experiments to verify its validity.

Since the instability analysis of Zuber (1966) predicted very low critical flow, further investigation based on this model is probably not warranted. However, since Simon's and Hsu's (1970) analysis and data imply a potential problem with any flux level, it would be prudent to develop experimental data for the molten salt that would support an analysis similar to Simon's and Hsu's.

It is important to point out that even for a darkened salt, the dryout mechanism of Simon and Hsu would still exist. This is because this mechanism is based on uneven lateral heating of the film or a nonuniform lateral film thickness distribution caused by waviness, neither of which would be affected by darkening the salt. The Zuber-type mechanism, which relies on a temperature gradient normal to the absorber through the salt film, can be totally eliminated by judicious use of dopants in which this gradient can be eliminated.

7.0 CONCLUSIONS AND RECOMMENDATIONS

7.1 Concept Feasibility

The experiments provide the data needed to confirm that the concept is feasible for use in solar thermal central receiver systems, although the behavior of the film should be examined further to increase our confidence in the system. The results of the experimental work can be highlighted as follows:

- The salt film is stable at flow rates high enough to be of commercial interest.

- Thermal efficiency of the salt film is in the range of 75%-95%, depending on temperature and flux.

- Heat transfer coefficients between the absorber surface and the salt film should exceed 3000 W/m^2 $^{\circ}C$, keeping the absorber no more than $150^{\circ}C$ above the bulk-salt temperature for flux levels of about 50 W/cm^2. This assumes no dopant has been added to the salt to darken it. Adding a dopant to the salt or operating the system in the turbulent regime greatly reduces the absorber temperature at a given flux and salt-film temperature. In the turbulent region we expect heat transfer coefficients of about 9000 W/m^2 $^{\circ}C$.

- The existing model, which predicts efficiency and heat transfer coefficients (or equivalently, absorber temperatures), can be used with confidence in the flow regime tested, assuming certain property values are determined with greater confidence in the future.

- Temperature control should not be a problem since the salt film responds rapidly to changes in flux. Simple buffer storage at the salt exit manifold effectively isolates the load from short-term flux fluctuations.

The experiments conducted at the ACTF were limited to a small-size absorber plate and to flux levels in the range of 15-60 W/cm^2. Because of these facility constraints, extrapolation of test results to other situations requires great care. For example, consider the following items:

- A change from the carbonate salt used in this study could alter some of the conclusions of this work.

- A possible stability problem exists for most flux levels with salt flows below 10.4 m^2/h.

- Special care needs to be taken at absorber edges to prevent dryout, salt degradation, and loss of salt.

- New stability problems could arise for long absorber runs (one meter or more) or operation in the turbulent-flow regime.

- Operation above 50 W/cm^2 will most likely require that the salt be doped to enhance absorption in the solar spectrum.

- Certain property values for the molten carbonate salt, notably the solar- and infrared-weighted extinction coefficients and thermal conductivity, need to be determined before the model can predict receiver performance reliably.

7.2   Recommendations for Future Research and Development

These recommendations follow naturally from the areas listed for additional considerations. Research topics include the following:

● Long Flow Lengths. Our experimental research was limited to a 0.6-m-long absorber. The literature suggests that longer flow lengths could lead to stability problems in the form of traveling waves that grow in amplitude. This problem needs to be addressed before an investment is made in a full-scale absorber panel for testing.

● Turbulent Flow. Turbulent flow enhances heat transfer between the salt and the absorber but could lead to stability problems not seen in the (laminar) experimental results presented here. Experiments are required to determine if any stability problems arise and also to determine the (salt-to-absorber) heat transfer coefficients for comparison with the model.

● Doped Salt. To absorb high fluxes and reduce the size and cost of the receiver, the performance of an absorbing salt needs to be studied.

● Edge Effects. As a follow-on to our results, the cause of the dry area needs to be investigated. The effect of edge treatments, which may solve the problem of salt containment on the absorber but create a different dry-out problem, should be investigated analytically and experimentally. Since a commercial DAR film may be exposed to more direct irradiation, as opposed to the diffuse irradiation in these tests, the dry-out problem could be aggravated. Testing under such conditions is needed.

● Property Values. Extinction coefficients at solar and infrared wavelengths must be determined especially for the doped salts. Thermal conductivity of the carbonate molten salt needs to be determined with greater confidence levels than we currently have.

8.0 REFERENCES

Anderson, R., forthcoming, *Heat and Mass Transfer in Falling Film Cavity Receivers*, SERI/PR-252-2822, Golden, CO: Solar Energy Research Institute.

Asbell, O. D., C. T. Brown, D. H. Neale, and C. L. Scott, 1984, *Molten Salt Test Apparatus Design*, Atlanta, GA: Georgia Tech Research Institute.

Brumleve, T. D., 1974, *A High-Temperature Solar Energy System*, SAND 74-8008, Livermore, CA: Sandia National Laboratories.

Brumleve, T. D., 1978, *Status Report on the Direct Absorption Receiver*, SAND 78-8702, Livermore, CA: Sandia National Laboratories.

Copeland, R. J., forthcoming, *A Direct Absorption Receiver (DAR) System Description*, SERI/TR-252-2625, Golden, CO: Solar Energy Research Institute.

GTRI, Mar. 1981, *ACTF User's Manual*, Atlanta, GA: Georgia Tech Research Institute.

Hruby, J. M. and B. R. Steele, 1985 (Aug.), "Design and Performance Evaluation of a Solid Particle Solar Central Receiver," presented at the AIChE Summer National Meeting, Seattle, WA.

Hunt, A. J., 1979, "A New Solar Thermal Receiver Utilizing a Small Particle Heat Exchanger," presented at the 14th IECEC, Boston, MA, 5-10 August 1979; also, LBL 8520, Berkeley, CA: Lawrence Berkeley Laboratory.

Hunt, A. J., and C. T. Brown, 1983, "Solar Test Results of an Advanced Direct Absorption High Temperature Gas Receiver, SPHER," *Proceedings of the 1983 Solar World Congress*, Perth, Australia, 15-19 August 1983; also, LBL 16497, Berkeley CA: Lawrence Berkeley Laboratory.

Janz, G. J., Dec. 1985, *Viscosity Measurement of Molten Carbonate Salt*, SERI/STR-252-2905, Golden, CO: Solar Energy Research Institute.

Jorgensen, G. J., P. Schissel, and R. W. Burrows, 1985 (Aug.), "Optical Properties of High-Temperature Materials for Direct Absorption Receivers," presented at the 29th Annual International Technical Symposium on Optical and Electro-optical Engineering, San Diego, CA; also SERI/TP-255-2791, Golden, CO: Solar Energy Research Institute.

Lewandowski, A. et al., 1984, *Direct Absorption Receiver System Study*, SERI/SP-253-2438 (Phase I, July); SERI/SP-253-2592 (Phase II, Dec.), Golden, CO: Solar Energy Research Institute.

Mamantov, G., G. Braunstein, and C. B. Mamantov, eds., 1981, *Advances in Molten Salt Chemistry*, Vol. 4, New York: Plenum Press.

Moiseev, G. K., and G. K. Stepanov, 1967, "Electrochemistry of Molten and Solid Electrolytes," in *Physicochemical Properties of Electrolytes and Electrode Processes*, Vol. 5, edited by A. N. Baraboshkin, New York: Consultants Bureau.

Newell, T. A., K. Y. Wang, and R. J. Copeland, Nov. 1985, "Film Flow Characteristics for Direct Absorption Solar Receiver Surfaces," in *Heat Transfer and Fluid Flow in Solar Thermal Systems*, Vol. 1, 1985 ASME Winter Annual Meeting, Miami Beach, edited by T. C. Min and J. P. Chiou, pp. 53-60.

Newell, T. A., K. Y. Wang, and R. J. Copeland, Feb. 1986, *Falling Film Flow Characteristics of the Direct Absorption Receiver*, SERI/TR-252-2641, Golden, CO: Solar Energy Research Insititute.

Seban, R. A. and A. Faghri, 1976 (May), "Evaporation and Heating with Turbulent Falling Liquid Films," *Journal of Heat Transfer*, pp. 315-318.

Simon, F. F., and Y. Hsu, 1970, *Thermocapillary Induced Breakdown of a Falling Liquid Film*, NASA TN D-5624. Washington DC: National Aeronautics and Space Administration.

Streeter, V. L., *Fluid Mechanics*, 5th edition, New York: McGraw-Hill.

Takahama, H., and S. Kato, 1980, "Longitudinal Flow Characteristics of Vertically Falling Films without Concurrent Gas Flow," *Int. J. Multiphase Flow*, Vol. 6, pp. 203-215.

Wang, K. Y., and R. J. Copeland, 1984, "Heat Transfer in a Solar Radiation Absorbing Molten Salt Film Flowing over an Insulated Substrate," ASME paper 84-WA/Sol-22; also, SERI/TP-252-2342, Golden, CO: Solar Energy Research Institute.

Wang, K. Y., T. A. Newell, and R. J. Copeland, June 1985, "Film Stability for Direct Absorption Receivers," presented at ISES/SESCI Intersol '85 Conference, Montreal, Canada; also SERI/TP-252-2739, Golden, CO: Solar Energy Research Institute.

Wang, K. Y., and F. Kreith, Sept. 1985, "Heat Transfer Research for High Temperature Solar Thermal Energy Systems," presented at the 1985 U.S.-Japan Heat Transfer Joint Conference, San Diego, CA.

Wilke, W., 1962, "Warmeugergang an Reiselfilme," *Ver. Deut. Ingr. Forschungsh.*, Vol. 490.

Zuber, N., and F. Staub, 1966, "Stability of Dry Patches Forming in Liquid Films Flowing over Heated Surfaces," *Int. J. Heat Mass Transfer*, Vol. 9, pp. 897-903.

SERI⬢

APPENDIX A

OPERATING PROCEDURES

OPERATING PROCEDURES
Solar Energy Research Institute
DARTS Receiver Test Program

Caution: No one allowed on tower until Step 2.0 without specific permission
from ACTF Test Director. Concentrated solar beam may not be in safe
position.

Step 1.0

1.1 Test Director: Distribute radios and verify their operation at
appropriate stations.

1.2 Mirror Field:

1.2.1 Service mirror field.

1.2.1.1 Pressurize mirror control air system.

1.2.1.1.1 Verify that main supply valves (two) on air
compressors on thermal cycle pad are open (red-
handled ball valves adjacent to compressors).

1.2.1.1.2 Verify that air compressor(s) are operating or
that tank pressures are between 100 and 135 psi.

1.2.1.1.3 Verify that air supply valve on auxiliary air tank
at base of tower is open.

1.2.1.2 Verify that mirror field is in safe position (move field
if necessary) and that field is not driving. Mirror
field control console should be left in "off" state
(440 v. and 120 v. breakers off).

1.2.1.3 Notify Test Director that tower area is safe for ascent.

1.3 Check REG 6 upstream pressure. If less than 500 psig, open additional
CO_2 bottle to the manifold behind the CO_2 station.

1.3.1 Verify REG 6 downstream pressure is 40 psig.

1.3.2 Verify that SOV7 is open.

1.3.3 Verify that SOV6 is open.

1.3.4 Set FCV6 for a 1 li/min flow rate on F4 (SS float at 10).

1.3.5 Open SOV9.

1.3.6 Open FCV9 and adjust to get flow rate of 0.9 SCFM (50% of F.S.) on rotameter F6.

Step 2.0

2.1 Data System:

2.1.1 Turn on Motorola TV cameras and monitors.

2.1.2 Initiate start up of data system in bit bucket mode (no data saved).

2.2 Mirror Field:

2.2.1 Determine declination and start setting field.

2.3 Test Director:

2.3.1 Ascend tower.

2.3.2 Remove weather protection.

2.4 Experimenter:

2.4.1 Ascend tower.

2.4.2 Remove weather protection.

Step 3.0

3.1 Test Director:

3.1.1 Verify that thermocouple oven is on.

3.1.2 Turn on data system monitor and bring up appropriate display (DISP DARTS←CHANA::DATA)

3.1.3 Verify that cooling water is flowing through all 10 fixed calorimeters (and rake, if installed).

3.2 Experimenter:

3.2.1 Verify that all 10 controllers are in remote ("REM") mode - controllers in enclosure at south end of skid.

```
┌─────────────────────────────────────────────────────────────┐
│                                                             │
│  CAUTION:  Cooling water to fixed calorimeters (and rake,    │
│            if installed) must be on before heating cavity.   │
│                                                             │
└─────────────────────────────────────────────────────────────┘
```

3.2.2   Activate trace heat circuit breakers and rheostats per Table(s) 3. Increment rheostats at no greater than 35% per 2 hours.

3.3   DARTS Console:

3.3.1   Adjust trace heat set points per tables(s) 3. Increment set points at no greater rate than 200°C per 2 hours.

TABLE 3

Trace Heat Settings; Step _____

Zone	Breaker (on/off)	Control Thermocouple and Set Point	Overtemp Set Point
Tank #1	8 (_____)	T5C (_____°C)	(_____°C)
Line B	5 (_____)	Rheostat (_____%)	N.A.
DV1	13 (_____)*	Rheostat (_____%)	N.A.
Line C	3 (_____)	T11C (_____°C	(_____°C)
FCV1	13 (_____)*	Rheostat (_____%)	N.A.
Tank #2	12 (_____)	T6C (_____°C)	(_____°C)
Lines D & E	11 (_____)	T12C (_____°C)	(_____°C)
FCV2	13 (_____)*	Rheostat (_____%)	N.A.
Line F	7 (_____)	T14C (_____°C)	(_____°C)
FCV3	13 (_____)*	Rheostat (_____%)	N.A.
Lines G & H	9 (_____)	T15C (_____°C)	(_____°C)
Kaman	15 (_____)	Rheostat (_____%)	N.A.
Absorber Manifold	6 (_____)	T18C (_____°C)	(_____°C)
Absorber Panel	2 (_____)	T19C (_____°C)	(_____°C)
	4 (_____)		
Absorber Dump	6 (_____)	T20C (_____°C)	(_____°C)
Absorber Trough	10 (_____)	T16C (_____°C)	(_____°C)
Line A	1 (_____)	Rheostat (_____%)	N.A.

Clock Time at Completion: _____

TABLE 3

Trace Heat Settings; Step _____

Zone	Breaker (on/off)	Control Thermocouple and Set Point	Overtemp Set Point
Tank #1	8 (_____)	T5C (_____°C)	(_____°C)
Line B	5 (_____)	Rheostat (_____%)	N.A.
DV1	13 (_____)*	Rheostat (_____%)	N.A.
Line C	3 (_____)	T11C (_____°C	(_____°C)
FCV1	13 (_____)*	Rheostat (_____%)	N.A.
Tank #2	12 (_____)	T6C (_____°C)	(_____°C)
Lines D & E	11 (_____)	T12C (_____°C)	(_____°C)
FCV2	13 (_____)*	Rheostat (_____%)	N.A.
Line F	7 (_____)	T14C (_____°C)	(_____°C)
FCV3	13 (_____)*	Rheostat (_____%)	N.A.
Lines G & H	9 (_____)	T15C (_____°C)	(_____°C)
Kaman	15 (_____)	Rheostat (_____%)	N.A.
Absorber Manifold	6 (_____)	T18C (_____°C)	(_____°C)
Absorber Panel	2 (_____)	T19C (_____°C)	(_____°C)
	4 (_____)		
Absorber Dump	6 (_____)	T20C (_____°C)	(_____°C)
Absorber Trough	10 (_____)	T16C (_____°C)	(_____°C)
Line A	1 (_____)	Rheostat (_____%)	N.A.

Clock Time at Completion: _____

TABLE 3

Trace Heat Settings; Step _____

Zone	Breaker (on/off)	Control Thermocouple and Set Point	Overtemp Set Point
Tank #1	8 (_____)	T5C (_____°C)	(_____°C)
Line B	5 (_____)	Rheostat (_____%)	N.A.
DV1	13 (_____)*	Rheostat (_____%)	N.A.
Line C	3 (_____)	T11C (_____°C	(_____°C)
FCV1	13 (_____)*	Rheostat (_____%)	N.A.
Tank #2	12 (_____)	T6C (_____°C)	(_____°C)
Lines D & E	11 (_____)	T12C (_____°C)	(_____°C)
FCV2	13 (_____)*	Rheostat (_____%)	N.A.
Line F	7 (_____)	T14C (_____°C)	(_____°C)
FCV3	13 (_____)*	Rheostat (_____%)	N.A.
Lines G & H	9 (_____)	T15C (_____°C)	(_____°C)
Kaman	15 (_____)	Rheostat (_____%)	N.A.
Absorber Manifold	6 (_____)	T18C (_____°C)	(_____°C)
Absorber Panel	2 (_____)	T19C (_____°C)◄	(_____°C)
	4 (_____)		
Absorber Dump	6 (_____)	T20C (_____°C)	(_____°C)
Absorber Trough	10 (_____)	T16C (_____°C)	(_____°C)
Line A	1 (_____)	Rheostat (_____%)	N.A.

Clock Time at Completion: _____

65

```
┌─────────────────────────────────────────────────────────┐
│                                                         │
│    Succeeding steps need not be initiated until trace   │
│    heat temperatures are within one hour of stabilizing │
│                                                         │
└─────────────────────────────────────────────────────────┘
```

Step 4.0

4.1 Test Director:

4.1.1 Set water flow rates as follows:

4.1.1.1 Large circular shield:__9__gpm (read:_____psig _____gpm)

4.1.1.2 Fixed calorimeter manifold:__4__gpm (read:_____psig, _____gpm).

4.1.1.3 Flux rake (if to be used during the day) __5*__gpm (read:_____psig, _____gpm).
[*monitor during solar runs and establish setting]

4.1.2 Verify all flows at drain.

4.1.3 Open shutters and lock out air supply; verify that shutters will not close.

4.1.4 Don full safety clothes and inspect aperture area from scissors lift.

4.1.5 Verify that catch pan is installed (omit this step for solar experiments).

4.1.6 Return to tower top.

4.2 Experimenter:

4.2.1 Don full safety clothes and inspect aperture area of experiment from scissors lift.

4.2.2 Inspect and remove all material from catch pan (omit this step for solar experiments).

4.2.3 Return to tower top.

4.3 Data System: Bring up data system in data capture mode.

Step 5.0

5.1 Test Director:

5.1.1 Close shutters.

5.1.2 Bring up data system monitor display (DISP DARTS←CHANA::DATA)

66

5.2 DARTS Console

   5.2.1 <u>DO NOT PROCEED</u> with this step unless valves above 500°C (check $TFCV_{xx}$ and $DV1_{xx}$).

                 Record: TFCV1:_____°C

                          TFCV2:_____°C

                          TFCV3:_____°C

                          DV1: _____°C

   5.2.2 Close valve controllers FCV1, FCV2, FCV3, FCV4 and DV1.

5.3 Experimenter:

   5.3.1 Verify that SOV5 is closed.

   5.3.2 Verify that bubbler shut off valve (SOV7) is open (valve located on <u>east</u> side of skid where CO_2 lines enter skid).

5.4 Mirror Field: Start air compressor using instructions on compressor. <u>DO NOT OPEN SUPPLY VALVE</u>.

Step 6.0

   6.1 Mirror Field: Open supply valve at compressor <u>only</u> when requested by Test Director.

Step 7.0

   7.1 Experimenter:

      7.1.1 Check P11 for minimum of 100 psig.

      7.1.2 Open SOV-5.

      7.1.3 Check for 20 psig reading on P12; adjust REG-7 if needed.

Step 8.0

   8.1 DARTS Control: Verify that salt pump turned off at console; i.e. "stop" light illuminated on console and the pump speed rheostat is set to zero.

   8.2 Experimenter: Verify settings of pump controller (controller is located in box on experiment deck). <u>Drive</u> to be set to <u>MANUAL</u>. <u>FREQ. ADJ.</u> to be at zero; i.e. full CCW.

Step 9.0

   9.1 Experimenter: Turn breaker #14 on (pump power).

Step 10.0

   10.1 Experimenter: all non-essential personnel vacate tower platform
and area below tower.

   10.2 Test Director:

       10.2.1 Verify that shutter control is armed (LOVE valve in operate
             position).

       10.2.2 All non-essential personnel vacate tower and area below tower.

       10.2.3 Lower elevator to ground level.

       10.2.4 Lock out elevator power at elevator platform.

Step 11.0

   11.1 Mirror Field:

       11.1.1 Perform mirror field pre-test checkout procedure (limit switches
             etc.).

       11.1.2 Check emergency air motor by momentarily opening double valve on
             north wall in mirror control shed. Mirror field will drive
             towards east limit if not already at east limit. If at east
             limit, fast track off limit and then open double valve
             momentarily.

       11.1.3 Verify that image is east of tower; if not, drive mirror field
             towards east limit until concentrated beam is east of scissors
             lift structure. This may involve sweeping beam across tower.
             NOTIFY TOWER TOP PERSONNEL BEFORE START OF ACTION.

   11.2 Test Director:

       11.2.1 Verify declination complete.

       11.2.2 Verify that data system operation is normal.

       11.2.3 Verify that radio operation is normal.

11.2.4 Verify that all personnel are on station:

a) Test Director (on ground or tower):_____

b) Experimenter (on ground or tower):_____

c) DARTS console:_____

d) Mirror field operator:_____

e) Data system operator/log and shutters:_____

f) CO_2 station:_____

g) Tower top personnel: (1)_____
                           (2)_____
                           (3)_____
                           (4)_____

Proceed to: Step 20 for pumped salt flow,
              Step 40 for pressurized salt flow, or
              Step 60 for experiment shut down

```
┌─────────────────────────────────────┐
│   PROCEDURE FOR PUMPED SALT FLOW     │
└─────────────────────────────────────┘
```

Step 20.0 Complete start up procedure for salt flow operations (Steps 1 - 19).

Step 21.0

  21.1 Data System:

        21.1.1 Open shutters.

        21.1.2 Focus TV camera #3 on aperture

        21.1.3 Close shutters when requested by Test Director.

  21.2 DARTS Console:

        21.2.1 DO NOT PROCEED to next step unless valves above 500°C
                (check $\overline{TFCV_{xx}}$).

        21.2.2 Open FCV1 to 100%.

        21.2.3 FCV2, FCV3 and DV1 remain closed.

        21.2.4 Verify that pump speed rheostat is set to zero.

        21.2.5 Push pump "start" button on console.

        21.2.6 Adjust pump speed rheostat to initiate salt flow. Flow rate set
                according to day's test plan.

        21.2.7 Turn off following trace heat: ___T16C (trough)

                                                 ___T20C (dump)

                                                 ___T19C (absorber panel)

Step 22.0

  22.1 Mirror Field: Bring up solar beam and start tracking with 23A. Notify
        Test Director when on track.

  22.2 Data System: open shutters when requested by Test Director.

22.3 DARTS Console:

    22.3.1 Conduct test according to plan.

    22.3.2 Monitor temperatures and use cooler (FCV4) to control
             temperature of Tank #1 at _____°C.

22.4 ACTF Tower:

    22.4.1 Monitor all cooling water temperatures and adjust flows as
             necessary.

[SHUTDOWN]

Step 23.0

23.1 Data System: Close shutters.

23.2 Mirror Field: Drive mirror field off target after shutters have been
closed.

23.3 DARTS Console:

    23.3.1 Reduce pump speed rheostat to zero.

    23.3.2 Press "Salt Pump" STOP button on console.

    23.3.3 Close FCV1.

    Go-to one of following, depending on test plan of the day:

        Step 20 - pumped flow
        Step 40 - pressurized flow
        Step 60 - shut down

```
┌─────────────────────────────────────────┐
│   Procedure for Pressurized Salt Flow    │
└─────────────────────────────────────────┘
```

Step 40.0   Complete Steps 1.0 through 19.0 before continuing.

Omit Step 41.0 if salt is already in Tank #2

Step 41.0   DARTS console (salt transfer to Tank #2).

41.1   Verify that Line B, DV1, and Tank #2 are all above 450°C.

41.2   Open Tank #2 vent valve (console).

41.3   Close Tank #2 presurization valve (console).

WARNING: Do Not Exceed 80% on Tank #2 Level

41.4   Open DV1. Drain salt into Tank #2 as needed (there is no minimum salt level required in Tank #1 when the pump is off).

41.5   Close DV1.

Step 42.0   Experimenter (CO_2 station).

42.1   Close FCV8.

42.2   Open the shut-off valve on the CO_2 bottle on which REG 5 is mounted.

42.3   Set REG 5 to 200 c.f.h.

42.4   Set REG 3 to 20 psi. Briefly open and close FCV8 to see response of REG 3 and verify the setting.

42.5   Open FCV8.

Step 43.0   DARTS Console (Tank #2 pressurization).

WARNING: Tank 2 pressure should not exceed 55% on control console meter or 17.9 psig on P3.

43.1   Verify that DV1 is closed.

43.2   Close Tank #2 vent valve--control console.

43.3   Open bubbler by-pass valve.

43.4   Open Tank #2 pressurization valve.

72

43.5 If Tank #2 is ever overpressurized (55% on control console meter), open Tank #2 vent valve.

43.6 When Tank #2 pressure, P3, has stabilized, close the bubbler by-pass valve.

Step 44.0 DARTS Console (salt flow)

44.1 Verify that FCV1 is closed.

44.2 Verify that FCV3 and/or FCV2 is above 500°C before doing next step.

$$\text{Record:}\quad \text{FCV2:}\underline{\hspace{2cm}}°C$$
$$\text{FCV3:}\underline{\hspace{2cm}}°C$$

44.3 Open FCV3 (C_v = 0.4) or FCV2 (C_v = 100); adjust as desired for flow control.

44.4 DO NOT allow the Tank #2 level to drop below 5 inches (10% on control console, LG2 = 100 kg).

Step 45.0

45.1 Mirror Field: Bring up mirror field and begin tracking with 23A. Nofify Test Director when tracking.

45.2 Data system: WHEN REQUESTED, open shutters.

45.3 DARTS console: Conduct day's test program.

45.4 ACTF Tower: Monitor cooling water temperatures.

[SHUTDOWN]

Step 46.0

46.1 Data System: Close shutters.

46.2 Mirror Field: After shutters have been closed, drive mirror field off to stand by position.

Step 47.0   DARTS Console (flow termination)

   47.1   Close FCV2 and FCV3.

   47.2   Close Tank #2 pressurization valve (console).

   47.3   Open Tank #2 vent valve (console).

      Go to one of the following, depending on test plan of the day:

         Step 20 - pumped flow.
         Step 41 - pressurized flow.
         Step 60 - shut down.

PROCEDURE FOR
EXPERIMENT SHUT DOWN

Step 60.0

60.1 DARTS console and CO_2 Station (order of events important)

    60.1.1 Close shut off valve on CO_2 bottle on which REG5 is mounted.

    60.1.2 Verify that Tank #2 vent valve is open (console).

    60.1.3 Open Tank #2 pressurization valve (console).

    60.1.4 Verify FCV8 open (CO_2 station).

    60.1.5 Allow system to bleed down (REG 3 + REG 5) (CO_2 station).

    60.1.6 Back off REG 3 and REG 5 (adjustment knobs).

    60.1.7 Close Tank #2 pressurization valve (console).

    60.1.8 Close FCV8.

    60.1.9 Close SOV9 (CO_2 station); close FCV9.

    60.1.10 Verify that SOV6 is open. Set FCV6 for a 1 li/min flow rate on F4 (SS float at 10).

    60.1.11 Verify that SOV 7 is open.

    60.1.12 Verify REG 6 downstream pressure is 40 psig.

    60.1.13 Check REG 6 upstream pressure. If it is less than 500 psig, open an additional CO_2 bottle onto the manifold behind the CO_2 station.

60.2 Mirror Field:

    60.2.1 Drive mirror field to point east of scissors lift structure.

    60.2.2 Turn off 120 volt and 440 volt breakers on mirror field console.

60.3 DARTS Console: Open FCV1, FCV2 and FCV3 to allow drain down of salt (console).

Step 61.0

  61.1 Test Director:

      61.1.1 Restore elevator electrical power.

      61.1.2 Ascend tower to operating level.

  61.2 Experimenter: Ascend tower to operating level.

Step 62.0

  62.1 DARTS Console:

      62.1.1 Delay 10 minutes after completing Step 60.

      62.1.2 Close FCV1, FCV2, and FCV3; verify that FCV4 and DV1 are closed.

      62.1.3 Advise mirror field that air compressor can be shut down.

  62.2 Mirror Field:

      62.2.1 Close gate valve at compressor.

      62.2.2 <u>When requested by DARTS console</u>, shut down air compressor using instructions on air compressor (bleed to 20 psig).

  62.3 Experimenter: Close SOV5 on east side of skid.

      62.3.1 Close SOV5 on east side of skid.

      62.3.2 Open breaker #14 (pump power).

  62.4 Test Director:

      62.4.1 <u>Do Not</u> turn off water to fixed calorimeter manifold.

      62.4.2 Turn off water to large circular shield.

      62.4.3 Turn off water to flux rake <u>if rake has been removed from cavity</u>.

Step 63.0

  63.1 Experimenter: Adjust trace heat breakers, rheostats and over temperature limits per Table 63.

  63.2 DARTS console: Adjust trace heat set points per Table 63.

TABLE 63

Trace Heat Settings; Step _____

Zone	Breaker (on/off)	Control Thermocouple and Set Point	Overtemp Set Point
Tank #1	8 (_____)	T5C (_____°C)	(_____°C)
Line B	5 (_____)	Rheostat (_____%)	N.A.
DV1	13 (_____)*	Rheostat (_____%)	N.A.
Line C	3 (_____)	T11C (_____°C	(_____°C)
FCV1	13 (_____)*	Rheostat (_____%)	N.A.
Tank #2	12 (_____)	T6C (_____°C)	(_____°C)
Lines D & E	11 (_____)	T12C (_____°C)	(_____°C)
FCV2	13 (_____)*	Rheostat (_____%)	N.A.
Line F	7 (_____)	T14C (_____°C)	(_____°C)
FCV3	13 (_____)*	Rheostat (_____%)	N.A.
Lines G & H	9 (_____)	T15C (_____°C)	(_____°C)
Kaman	15 (_____)	Rheostat (_____%)	N.A.
Absorber Manifold	6 (_____)	T18C (_____°C)	(_____°C)
Absorber Panel	2 (_____)	T19C (_____°C)	(_____°C)
	4 (_____)		
Absorber Dump	6 (_____)	T20C (_____°C)	(_____°C)
Absorber Trough	10 (_____)	T16C (_____°C)	(_____°C)
Line A	1 (_____)	Rheostat (_____%)	N.A.

Clock Time at Completion: _____

Step 64.0

  64.1 Data System: Shut down data system, save data and initiate plots/ printouts.

  64.2 Test Director:

      64.2.1 Open shutters and use LOV valve to lock out air supply.

      64.2.2 Don safety clothes to allow work below experiment deck.

      64.2.3 Use scissors lift to inspect aperture area of experiment.

      64.2.4 Return to deck and close shutters.

  64.3 Experimenter: Inspect aperture area of experiment and return to deck.

Step 65.0

  65.1 Experimenter:

      65.1.1 Install weather protection.

      65.1.2 Descend tower.

  65.2 Test Director:

      65.2.1 Install weather protection.

      65.2.2 Descend tower.

Step 66.0: All stations swap copies of logs.

opproc/darts

APPENDIX B

TEST PLANS WITH DAILY NOTES

The first part of this test will verify that the test loop and data system are working as they did on the ground. It will be carried out after the test loop is installed on the tower, connected to power and instrumentation, and the salt melted.

As the salt is being melted, carry out the cavity heat loss experiment. Operate the absorber heaters at steady state with the controllers. Determine the voltage applied to the heaters, the current when they are on, and the percent on time. Repeat for absorber temperatures of 500°, 600°, and $700^\circ C$. Use the inlet manifold and dump heaters as guard heaters. Determine if the modified absorber (removal of the cavity convection suppression plates) has created large convection losses.

After completion of the loss test proceed as follows:

a. Establish salt flow with the pump in the range of 2 to 10 gpm, $600^\circ C$ temperature in Tank 1.

b. Observe the flow on the absorber plate with the video or a telescope located near mirror 36H. Insure that installation of the cavity has not caused problems with salt flow into the dump for the full flow range.

c. Check data system output for any irregularities in any channel.

d. Determine that the salt outlet probe gives reasonable temperatures by comparing the indicated heat loss with that measured in the heat loss experiment above. If the comparison is not good, the outlet salt thermocouple should be moved, perhaps down in the outlet manifold to improve its output. This is a critical measurement.

e. Drain salt from Tank 1 to Tank 2. Exercise the bubbler shunt valve/Tank 2 pressurization procedure. Operate from Tank 2 at various flow rates. Confirm correct operation and correct gpm calculation by data system.

Format of data output: Be sure output has listed salt inlet and outlet thermocouples.

The second part of this test will establish whether the flux scanning bar causes any disruption in the salt flow.

a. Establish a salt flow rate in the 4 to 6 gpm range.

b. Observe the video monitor for salt film disruption (especially on the knife edges) as the flux bar is scanned down the plate.

Time and conditions required: one or two nonsolar days.

Format of data output: None special.

Expected results: The flows on the panel and the outlet manifold should look like they did during ground tests. Salt outlet thermocouple should prove reliable. Presence of the flux scanning bar should not disrupt the film although at higher flows it will probably assist salt in crawling over the knife edges.

Results:

Tests of 10/22/85:

Cavity loss test. Measured volts and amps on the two absorber circuits in the left and right Hoffman boxes behind the cavity. To do this we had to turn up the set point so they were not cycling. This gave 6393 W for 100% on time. Tried different proportional bandwidths to slow down cycle time but did not work so we estimated the on time at pretty close to 50% or about 3196 W to hold the cavity at about 550°C plate temperature (after overnight soak). This loss would only correspond to a salt delta T of about 14.7°C at 1 gpm flow.

We then went to a tank 2 test because we only needed to drain salt from tank 1 to 2 to proceed. This seemed to go very slowly so we quit after we had about 550 kg in Tank 2. Possible problem here--check later.

Ran out of tank 2 at four flow rates: ~0.5, ~1.5, ~0.06 (!), ~3.4 gpm. It was very difficult to establish a desired flow rate especially when increasing valve 3 setting, the last flow was out of valve 2 and it was easier to control. Also easier when decreasing flow than when increasing flow. This could be critical during Tests V and VI. Noticed large salt delta T, much larger than loss test would indicate. Presence of cavity top did not affect this figure implying that the error is due to poor placement of T/C's 20. Jim and George adjusted the weir at the lower flow rate so that the (centered) rivulet was about 1" from the center (best they could do).

Then ran out of Tank 1 at 4.8, 7.0, 8.0, and 10.0 gpm. There was some leakage at 10 so we quickly backed down to 8 or 9 and it was ok. Otherwise everything worked fine. Salt delta T indicated about a 24-32 kW heat loss! It actually increased with increasing flow indicating that the thermocouple error stayed the same as the flow increased. Definitely need to move these probes.

Then performed a cooldown test. With the air valve wide open we still got only 160 SCFM and no more than about 90 psig at the P4 although the compressor was cycling between 105 and 125 psig (about 3 sec cycle). Need to reduce data to see if cooling rate is sufficient anyway. Regardless, it would be helpful to put a pressure gauge just before the pressure regulator and just after the compressor filter to see where the pressure drop is coming from.

Flux rake test not done on run of 10/23/85. Video was not working yet so it was not yet tested.

Action items:

● Move T20 to better location
● Software changes/corrections relayed to Paul and Will
● Check draining from Tank 1 to Tank 2
● Carry out flux rake checkout per test plan
● Test video when it is ready.

Spent 10/23/85 installing two new salt outlet thermocouples, to be called T20A and B. It was difficult to insert these and tell where they ended up exactly. As best as we could tell, A is in front of the dump on the floor of the trough. B is definitely down the drain pipe about 2" and probably on the floor of the pipe.

Tests of 10/24/85:

Ran out of tank 1 at 2, 4, 6 gpm. Spent a lot of time to convince ourselves that T20 A and B are giving ok readings. Checked grounds, shields, sensitivity to heat trace, etc. It appears that T20A is quite good as it tracks the last absorber thermocouple well, is quiet and does not appear to be susceptible to trace heat effects as much as B.

We still have a substantial problem with heat loss than if we believe T20A although it is a lot better than before. Then ran out of tank 2. (Transfer from tank 1 to 2 went very quickly, about 20 minutes so problem noted on 10/22 was not real.) Paul's gpm calculation still not right (he later found problem--inadequate precision when operating on the time variable which is in seconds since midnight) and still a large salt delta T. However, noted that for very low flows (0.16 gpm) the implied heat loss was about 3 kW consistent with the dry absorber heat loss tests. (Radiation loss is about 3 kW so this dry absorber loss is probably mostly radiation out cavity.)

This would tend to imply that the presence of a substantial salt flow greatly increases the convective loss, up to 25 or 30 kW. One possibility for this would be the setting up of a convective loop as shear at the falling film pulls air down and out of the cavity drawing in cold fresh air.

Will test this by plugging up cavity and running again.

Tested fit of flux rake and adjusted its manual stop. It looks fine. Also, the mirror field camera was made operational although it is not fully automatic yet--it should suffice. Will stock up on video tape blanks for solar runs. We decided that since the rake does not touch the absorber panel, we will not test the rake with flow salt--it should be ok.

We removed Reg 4 after the 10/22 test because it had a 12-14 psi drop across it and does not seem to do anything useful (confirmed by C. Benham). This definitely increased flow and cooling as shown in another cooling test performed on 10/24. Need to reduce data.

Action items:

● Inspect cavity and box for heat leaks and proceed to next step:
● Place tight fitting cap over cavity opening and repeat flow tests for several flow rates.

10/25/85 Continuation of Test I

After George packed more insulation into the top and back of the box where the lines enter, he plugged the cavity opening with some wool and covered that with marinite board sealed to the cooling coil with duct tape.

We then ran out of tank 1 at about noon at 3.3 gpm and 6 gpm. At 3.3 gpm using the probe T20A near the dump we have ~20 kW loss, using probe T20B it is about 10 kW. Going to 6 gpm we have about 7.5 kW using probe T20B. So, probe B seems to be closer, but clearly we cannot have a 20 or even 8 kW loss from a plugged cavity. Therefore, we must still have thermocouple errors.

I did a calculation of the heat loss from under the trough and drain line (where T20A and B are) and realized that when George and I inserted these probes in on 10/23 the insulation had salt in it. This occurred from the first run where we overflowed the trough and spilled some salt into the drip pan.

Calculation: Assume a thermal network (see George notebook dated 10/26/85) with resistance between salt and probe (which is on internal tube surface) tube wall resistance, and insulation resistance. For the salt to probe resistance, use a range of values of h=100 and 1000 Btu/hr ft^2°F, for the wall resistance use 2" sched 40 Inconel (0.154" wall, k=12 W/m K), and for the insulation 2" thick use k=1.9 (wet, like salt) and 0.0548 dry. With 600°C salt in the trough and 20°C cooling water the probe would read:

Indicated probe temperature

| h > 100 | 1000 Btu/hr ft^{2}F |
| (low flow) | (high flow) |

| dry | 598.9°C | 599.9°C |
| wet | 564 °C | 596.2°C |

The value of 596.2 is definitely the kind of error we are seeing at 3-6 gpm, while the 564 is more like the error we saw at 0 .16 gpm.

It would definitely be worthwhile to remove the bad insulation when we replace the thermocouples with the new Inconel ones due in on Monday. Also, we should use the two new ones as inlet and outlet salt temperatures if T18A is easily accessible.

It would also be interesting to look at gpm vs. delta T for run on 10/24 (open cavity) and 10/25A (closed cavity).

10/28/85 see notebook: Cleaned out bottom of cavity area—removed a lot of saturated insulation and improved the whole insulation scheme to eliminate possibility of saturated insulation cooling bottom of drain pipe where new outlet probe is. Checked out new 18" Inconel probes together in inlet manifold—they give exactly same reading all the way through the computer system.

10/29/85 ran with plugged cavity hole, new inlet manifold thermocouple (new Inconel probe with extension cable) inserted vertically into inlet manifold and also new one with Inconel and extension inserted down drain pipe. Then decided that original inlet probe was best so used it with an extension cable.

Results: heat loss measurement seems pretty much fixed at near 7 kW. Also measured cavity surface (exterior) temperatures and calculated that for natural convection losses from cabinet, exterior surface would be 3.1 kW, radiation from exterior is 100 W, radiation from cavity should be about 3 kW.

11/4/85 ran with open cavity hole to measure losses again and to be sure that no problems remain before Tuesdays guaranteed sun. Only problem was that one flux transducer is reading 269 W/cm^2 at all times. Re-ran loss test at several flows and found that loss seemed to increase slightly with flow rate from about 7 kW at 2.5 gpm to about 8.5 kW at 6.9 gpm.

Test II Flux ramp test with actual results

The purpose of this test is to bring up the solar flux on the panel slowly, allowing time to observe the salt film behavior and absorber plate temperatures. The test will start with about 20% of full power and a high salt flow to insure cooling of the plate and a relatively low salt inlet temperature. The test provides preliminary evidence that the salt

film/absorber plate temperatures are well behaved over the full range of flows from Tank 1, allowing Test IV, the major test from Tank 1, to be carried out with minimal concern about film behavior.

The initial 20% power will be accomplished by only using a few mirrors at a time. Begin with the mirrors marked "I" (see the DOE ACTF Mirror Field Configuration diagram). This will be 96 mirrors or about 17% of the mirrors and somewhat more flux due to the cosine effect. This flux will mostly hit the top of the cavity and bounce around, eventually being absorbed on the salt film.

a. Establish steady state operation at 7 gpm and about 600°C in Tank 1. Achieve equilibrium and record heat loss, kW

b. Bring the flux into the cavity

c. Observe the absorber plate temperatures and the plate itself with the video camera. This will require two people

d. A third person will be needed to observe Tank 1 temperature as it rises due to heat input. This person will need to bring on the cooling air flow and try to maintain the 600°C temperature. Some trial and error will be necessary to achieve smooth temperature control (critical for later tests at high temperature)

e. Abort if the absorber plate temperatures begin to rise quickly or if any flow irregularities occur on the plate

f. When it appears that behavior of the flow on the absorber and plate temperatures are normal, bring on mirrors indicated by "1" in the mirror diagram. This will bring on an additional 31 mirrors which will directly "see" the absorber plate.

g. As these mirrors are brought into the cavity, continue to observe the plate and plate temperatures and continue to monitor the Tank 1 cooling

h. When steady conditions are achieved and all appears normal, bring the mirrors marked 2, 3, 4, 5, and finally 6. This will require some time so it will be possible to carefully monitor the absorber behavior and to carefully control Tank 1 cooling

i. After steady conditions at maximum flux are achieved continue to observe temperatures and flow patterns and recording data for a short period, about 20 min.

j. Begin reducing the flow rate by reducing the pump speed. Do this in steps of about 1 gpm until the lower pump speed limit is reached (to avoid sudden flow stoppage). The objective is to achieve laminar flow as will be obvious in the video output. At the 600°C temperature this will occur at about 6 gpm (Reynolds number of 500) and below.

k. At each step, observe the flow for any unusual behavior. Note that the absorber plate temperatures and the salt outlet temperature should increase with decreasing flow but not suddenly. A sudden increase would imply a hot spot.

l. Continue stepping the salt flow down until either laminar flow is reached, or it is necessary to abort due to excessive plate temperatures or unusual flow patterns.

Time and conditions required: one solar day

Format of data output:

A video tape of the entire run is needed. Get a plot showing: salt inlet temperature, salt outlet temperature, and salt flow. Get a second plot showing output of all absorber plate temperatures and a third plot showing output of all flux transducers throughout the test. Get another set of three plots of the steady region with maximum flux and 7 gpm and also in the laminar (lowest steady salt flow) region.

Plot T_{si} from 550° to 650°C, T_{so} from 200° to 600°C, gpm from 0 to 10, flux from 0 to 100 W/m², and T_{abs} from 500° to 1000°C.

Expected results:

We should be able to observe the flow as the flux increases with no unusual behavior exhibited at 7 gpm. It should also be possible to decrease the flow into the laminar range (but not into the dryout range, see Test VI) slowly with full flux without any unusual behavior in either the film behavior or hot spots on the plate.

Actual Results:

Run 10255B starting at 1 pm EDT. Brought up beam at 1:48 pm EDT with mirror section I. Proceed according to above test plan and completed through set g and through step h as far as bringing mirror field section 3 on line. Complete on 10/26.

Video view was very good up until more mirrors were brought on where it degraded somewhat (see video tape of entire run). Initially, flux levels were 4-8 W/m^2 with section I on line. Definite trend to higher flux towards top of cavity. When section 3 was on line, fluxes were 12-19 W/m^2.

Time	Insolation	Incident Flux	T19H
14:36	670	10.7 8 (I123)	641°C (cloudy)
14:20	751	5.44 kW (I+1+2)	699°C
13:39	808	10.4 (I+1)	669°C
12:56	813	6.2 (I)	635°C

It was never really clear after field 3 was brought on line so we will complete this on Saturday.

Generally, everything seemed well behaved per expected results. Some Tank 1 cooling was required. This was not especially easy to control. At first we thought we saw a spot on the film which could have been a dry spot. We bumped up the flow a bit, but it turned out to be a internal reflection which went away at higher fluxes.

Continue to monitor per plan as more flux is brought up.

11/5/85 Completed Test II:

Brought up remainder of mirrors (4,5,6) at 7 gpm and 600°C per test plan. Nothing unusual observed with exception of T19H swapping with T19K as the highest temperature. T19K and H were both about 785°-800°C when mirrors 5 then 6 were brought on line. Then T19K reached the following maximums when we ran at 7, 6, 5, 4, 3 gpm 600°C:

gpm   T19K (max)

7   785°C
6   845°
5   872°
4   900°
3   920°

Other T19s were around 100°C cooler. Observation of the video (the tape shows it but not very clearly) is the existence of a darker strip starting fairly high on the plate and getting wider as one goes down the plate. Maximum width near bottom is about 2". This dark area goes over T19K and must be a dry patch based on the difference between T19K and J which are at the same height but different spans. Inspection of absorber at end of test revealed same dark area but no damage at all. It is just slightly darker. Need to plot T19s and flux (which was highest near the bottom right of the plate) for the run to find out when it occurred.

Also got a "closed shutter" run during this test, check data and see if we can get anything useful for IR/solar split.

Noticed that efficiencies were very good. In fact, if we added in the 7 kW loss that we had calibrated, we would definitely be above 100% efficient. Without adding this in we were in the range 88%-92% based on 6" plate width. It now seems that this 7 kW loss is real only when the plate is hot because it is radiating to the other cavity surfaces which are cooler because of substantial losses out to the ambient. When solar is one, the cavity walls are hotter than the plate and act as a source to the plate. See my notebook of 11/5 for calculations of the losses from the plate when under solar conditions: they include conduction out back insulation (<30 W), conduction out supporting Inconel rod (<18 W) and convection (<<900 W). Remaining loss is reradiation out cavity which is part of loss we are interested in. Need fairly careful calculation of view factor from plate out cavity to calculate this, but we can calculate it. It will be included in the efficiency.

Inspection of cavity after test revealed a white coating on flux transducers, probably due to the off tracking which burned up some silicon sealer and cladding. Dave cleaned this off on 11/6 but said data for 11/5 was probably suspect.

Test III Flux map test

This test determines if the fixed flux transducers give comparable results with the scanning bar; i.e., whether there is significant variation of flux across the absorber plate. It is to be repeated three times on a clear day, early morning, solar noon, and late afternoon.

While waiting for noon or 3 p.m. it will be possible to proceed with Test IV steps k through s if the flux rake output looks reasonably constant for all transducers when the rake is at one height.

a. Establish 6 gpm and 500°C in Tank 1
b. Bring on full flux
c. Record flux transducers and make a pass with the scanning flux bar. Locate the rake at the 10 elevations of the fixed transducers for a period of 10 seconds or until the rake transducers become steady.

Time and conditions required: one full solar day, sun in 3 pieces at 9 a.m., noon, 3 p.m.

Format of data output: Plot output of all fixed and moveable transducers on a 0-100 W/m² scale and inlet manifold temperature on a scale of 450°-500°C.

Expected results: The fixed and moveable transducers should agree at each vertical location of the scanning bar. Indicated variation across the plate at each vertical location should not be greater than ±15% from the mean for that vertical location.

Variation in the vertical direction is permissible. The agreement should hold throughout the day for a wide variation in sun angle.

Actual results: Ran per test plan with scans at 10:00-10:37 for the morning run, 12:59-13:30 for the noon run, and 15:52-16:13 for the afternoon run (solar noon was 12:21 EST). I recorded data by hand to quickly reduce it to see if we could proceed with Test IV in between Test III phases. We located the rake at each of ten vertical positions and held it there for about 1-2 minutes and wrote down data for all 6 rake calorimeters and the one fixed calorimeter nearest the rake. The results were as expected.

In the morning the flux was increasing with the sun angle but typical variation of the rake transducers was 9%-12% rms. Had to drop CM because it was noisy and read low at all times.

At noon variations were 5%-9% and in the afternoon about 10%-12%. In the afternoon, we were loosing the sun pretty quickly so did not get as complete a scan as we would have liked.

In general, the fixed transducer near the rake read low because it was behind the cooled rake. Also, the rake was further into the cavity by maybe 2" so it read higher for this reason too. We had some peak readings on the rake at noon of 68 W/cm^2.

Transducers were getting coated with some white powder (analysis revealed potassium as major component). They were cleaned just before a.m. test, noon test (I think), and p.m. test. Must check Test IV results to see how this was affecting the flux transducers--but probably Test III was successful: no other explanation for minimal variation across plate.

Plots of the rake output show the maximum flux on the right edge of the absorber with a local minimum in the center and the lowest value on the left edge. There is a clear increase of flux ~2x from top to bottom. Along the right edge at noon the flux at the top is about 33 and at the bottom it is nearly 70. This trend holds along a traverse of the plate. See plots.

Test IV Film stability and transition.

      IR/Solar Split
      Film efficiency

This test will verify that the film is stable in the full range of flow in the presence of flux, determine the split between long and short wavelengths in the cavity, and give the thermal efficiency of the salt film over a range of average film temperatures from 500° to 750^oC.

   a. Establish 6 gpm and 500^oC from Tank 1
   b. Bring up full flux
   c. When equilibrium is reached, take data for about 5 min. Observe video output for unusual behavior.
   d. Close the shutters
   e. Continue taking data until the flux transducers drop to about 2 W/m^2
   f. Open the shutters and wait for steady state
   g. Increase flow to 8 gpm, and repeat step c
   h. Increase flow to 10 gpm, and repeat step c
   i. Decrease flow to 4 gpm, and repeat step c

j. If it appears that two or three good solar flux hours are left in the day, shut off Tank 1 cooling and let it come up to 600°C. If not: shut off flux, achieve equilibrium and record heat loss, kW. Then, set Tank 1 control to 600° C for next day's testing.

k. Establish 6 gpm with the 600°C in Tank 1

l. Bring up full flux. Turn on Tank 1 cooling.

m. Repeat step c

n. Close shutters

o. Continue operating until flux transducers indicate <2 W/m² output

p. Open shutters and wait for steady state

q. Increase flow to 8 gpm, and repeat step c

r. Decrease flow to 4 gpm, and repeat step c

s. Decrease flow to 2 gpm or minimum, and repeat step c

t. If it appears that 2 or 3 good solar flux hours are left in the day, shut off cooling to Tank 1 and allow it to come up to 700°C. If not: achieve equilibrium and record heat loss, kW. Then, set Tank 1 controller to 700°C for next days testing.

u. Set Tank 1 flow to 6 gpm

v. Bring on flux into cavity. Turn on Tank 1 cooling.

w. Wait for equilibrium then take data for about 10 min

x. Close shutters

y. Wait for flux transducer to indicate <2 W/m² output

z. Open shutters

aa. Increase flow to 8 gpm and repeat step c

bb. Decrease flow to 4 gpm and repeat step c

Modified Test Plan IV (11/9/85) 700°C

Start-up note: to avoid smoking from the fins try starting with 3 gpm or so and increase just after the flux is brought on.

a. If possible to run in the morning as the flux increases from 25 to 60, establish a flow near the critical (assuming this is not a function of temperature try 5 to 5.5 gpm) and leave for the entire morning. Watch T19K-J increase as the flux goes up. The right flow chosen if the initial delta T is around 20° to 40°C and increases to 100° to 150°C.

b. During the noon period (CU will read ~50 W/cm²) run flows of 7, 6, 5, 4 gpm for about 10 min. each or until delta T is steady. Photograph if possible the dry spot forming and going away.

c. Beginning around 2 p.m. the flux will be around 50, so set a flow just below the critical (with the assistance of the a.m. data) and watch it as the flux drops to 20 or so.

End of modified plan for 11/9/85

Time and conditions required: One solid day of sun, probably two.

Format of data output:

A video tape of the entire run is needed. Get a plot showing: salt inlet temperature, salt outlet temperature, and salt flow. Get a second plot showing output of all absorber plate temperatures and a third plot showing output of all flux transducers throughout the test.

Plot T_{si} from 400° to $800^{\circ}C$, T_{so} from 400° to $800^{\circ}C$, gpm from 0 to 10, flux from 0 to 100 W/m^2, and T_{abs} from 500° to $1200^{\circ}C$.

Expected results: The absorber plate should not exhibit any unusual excursions in temperature. Observation of the video output should not be noticeably different than that taken on the ground.

The plots of flux transducer output should be level until the shutters are closed. After a short period of garbled output, the flux transducers should show an exponential output as the cavity cools off and the IR in the cavity decays. It should be possible to extrapolate the exponential curve back to the point where the shutters were closed to determine how much of the indicated flux at that point was short wave or long wave.

At $500^{\circ}C$ Tank 1 temperature, the salt outlet temperature should be 523°, 531°, 546°, $592^{\circ}C$, for 8, 6, 4, and 2 gpm, respectively. For the $600^{\circ}C$ Tank 1 temperature these values will be 623°, 631°, 646°, and $692^{\circ}C$ for 8, 6, 4, and 2 gpm. For the $700^{\circ}C$ Tank 1 temperature, these will be 723°, 731°, 746°, and $792^{\circ}C$ for 8, 6, 4, and 2 gpm. This assumes about 40 kW absorbed by the film.

Calculate the film efficiency from the energy absorbed in the film [$mC_p(T_{so}-T_{si})$+ $Q_{loss}(T_s)$] divided by the average flux falling on the film. Plot efficiency as a function of average film temperature which should vary smoothly from 500° to $750^{\circ}C$.

Actual Results:

11/6/85

Interleaved the $600^{\circ}C$ part of this test with the gaps in Test III.

Note: the two critical probes: T18A and T20A are now both Inconel probes with extension wires. T18A is in the inlet manifold vertically just into the packing bed and T20A as before is in the drain pipe.

The first Test IV was just before solar noon, started at 6 gpm and got efficiencies around 87%-90% then did a IR/solar split test. The flux dropped very quickly to ~10 W/cm^2 and to 3-4 then slowly below that. This indicates a small component of IR. Need to reduce data.

Went to 8 gpm and saw that T19K agreed closely with J and I. Ran for about 10 minutes. Then went back to 6 gpm briefly, then 5, then 4 per test plan. What appeared to be a hot spot appeared on panel with smoke and T19K going to $950^{\circ}C$. (Later discovered that the stainless spill tray had become exposed and may have been contributing to the smoke.) Went quickly back to 7 gpm at 12:21 this brought K more in line with I (854/839) so ran there for ~5 minutes. But problem here was that efficiency was >100% apparently because the fixed transducers got smoke on them and read too low. Need to inspect fixed transducer vs. time compared to insolation to see if we can detect a sudden drop in the fixed even as the insolation was increasing. This will clearly show where the efficiency data is believable.

At these high fluxes, it seems that the minimum flow is quite high, maybe 7-8 gpm. Eight worked very well. Definitely 4-5 is not acceptable. It is almost like there is a very sharp increase in minimum allowable flow with flux because we ran late in day at 2.8 gpm with no problem.

Got two shutter closing tests at 11:28:04 and at 12:26. For these need ACTF temperatures, fixed transducers, T18A and T20A minimum.

Due to smoked up flux transducers we ran this part of Test IV again after the noon Test III. This went from 14:00 to 15:03. I think we cleaned the flux transducers first (nearly sure). Tried to start at 8 gpm but this produced a lot of smoke from the edges. Tried at 9 gpm. Less smoke but still some. Reduced flow to 8 gpm--continued smoking. Check transducers again for loss of signal to assess validity of this data. Ran at 8, 7, 6, 5, 4, 3 gpm about 10 min each. No real problem but check T19K to be sure.

Inspected cavity after this run and found some crud on flux transducers but not too bad. BL looked quite clean. Decided that most of the smoke towards the end of latest run was due to exposure of stainless steel tray to flux and subsequent disintegration. Stuffed Kaowool to protect tray and went on to last part of Test III. At end of Test III we found that Kaowool was saturated (must have wicked salt) but found no film on transducers.

Good shutter closing at 15:01. Check for IR/solar split data.

Interesting data:

- is efficiency data (flux data) good?
  if so, reduce it
  if not, need way to keep flux transducer clean and retry
- is IR/solar data good?
  if so, reduce it
  if not, why? can we improve it?
- deduce from T19 data, gpm, flux where critical conditions occur. This could be more important than and is similar to Test VI where it was to be done for very low flows and fluxes. So we are really modifying the test plan. This could be more important than knowing the efficiency to n decimal places since it determines if the DAR concept will work at all.

11/7/85:

Attempted a run at 700°C, 6 gpm from tank 1 (only got tank 1 to 683°C). Had good sun for a short period and run appeared to be good but shortly came some high clouds. We did not observe any smoke this time so the flux transducers stayed clean (as verified during later inspection) but we began to get salt dripping out the west edge of the silica cum Kaowool, so we shut down after which heavy clouds came in anyway.

We observed the absorber film flow from the cavity top and from below in the scissors lift even up to 8 gpm without any salt spillage at all. It was at least as clean as we saw on the ground even at 700°C. Two possibilities: the Kaowool is wicking a reservoir from an old spill or the higher salt temperatures coupled with flux is causing unusual behavior of the film. C. J. cleaned out the problem areas and will make repairs more permanent than the Kaowool. He noted that he saw a good deal of salt behind the silica and in front of the stainless steel. Lower tank 1 to 500°C and try again tomorrow.

11/8/85:

C. J. repaired the silica area and it held. I incorrectly reset the tank 1 temperature last night to 600°C, wanted 500°C. In trying the cooling air to drop it we found that it did not work. So we replaced the I/P controller and it worked. Dropped to 500°C pretty

quickly. During this Will checked the offset for flux transducer CZ. (Tom had questioned this based on the offset for CZ relative to the others on the shut-down exponential curve.)

Brought beam up at 12:19, still got smoking especially at start. This probably precludes any good flux transducer measurements except that maybe the BR one is not bad.

During this run we got very good observation of the plate with the Celestron telescope of the dry area and also on the video. It is definitely the wedge shape that forms on the right side and it does so at fairly high and repeatable flow rate. The edge of the wing exhibits bubbling salt and is probably a source of the vapor depositing on the calorimeters. Also, there does not seem to be much hysteresis; i.e. it goes away at about the same flow rate on the way up as it forms on the way down. The temperature excursions on T19K correlate very well with the formation of the dry area. Observed the film through the Celestron at the $500^{o}C$ conditions high flux case (noon+1.5 hr). Need to come up with a clever way to quantify the temperature excursions with video, flow rate, Re (?), flux.

The $500^{o}C$ run was at 6, 5, 4, 8, 9, 6.5, 6, 5.5, 6, 7 gpm. Around 6.5 gpm was critical. Also noted that at 6.5 gpm T19K-T19J increased even if it was not fully dry--may just be a continuous thing. Dropped to 6 and T19K really took off, $46^{o}C$ in 8 minutes. When the dry wing was visible you could see it open and close as the flow was decreased and increased, respectively. Back up to 7 and the film looked very clean. Need to correlate this with BR flux transducer--it was reading 54.2-51.9 during all this.

Then shut off cooling air and got to $600^{o}C$ in about 40 minutes, per the plan. Here the flux had dropped to about 45; we ran at 7, 6, 5, 4, 5, 7 with some intermediate points. Then set up Celestron for photos at 14:59, 8 gpm, flux BR=40 and dropping. Ran at 8, 7, 6, 5, 3.8 (held at 3.8 while the flux dropped to 33.9) then 5, 6, 6.5, 7, 9, 8.5, 7, 6.5, 6 (held at 6 while the flux dropped from BR=27 to 19) then finished up at 4, 2.7 to the finish when BR = 15. Could clearly see the effect of flux, which when reduced produced no noticeable dry spot even at 2.7 gpm.

To answer the three questions on Page 4: (i) efficiency data is probably going to be extremely difficult to get unless we solve the smoking problem. We will have a few points but clearly the stability problem is more important. (ii) the IR/solar data is good and suggests that about 20% of the flux the transducers see is IR, probably less. This may be less important, see (i). (iii) focused today's run on the stability question and we seem to have a very good handle on the stability at $500^{o}C$, high flux, $600^{o}C$ low and very low flux (in addition to previous runs).

At end of test, cavity inspection revealed no obvious place which could initiate the dry spot except the discoloration where it had been is now a little more obvious and you can see the "tracks" of 2 or 3 wings. No bumps or spots which would be doing this. Also, alignment can not be the problem because this was only a problem before at <0.2 gpm, now we have flow mal-distribution at 6-7 gpm. The BL transducer looks pretty clean at the end of this run. BR has a light film on it but its center spot is pretty black. One above BL looks like BR.

After reducing data from 11/8/85 run: $500^{o}C$ data were done at noon during constant flux and are a very good database for the effect of flow rate on dry spot at fixed flux. The temperature difference T19K-J is quite low for flows above 7 gpm (~10 C) and increase quickly for flows less than that ($40^{o}C$ at 6 gpm, $90^{o}C$ at 5.5 gpm, $125^{o}C$ at 5 gpm, $180^{o}C$ at 3 gpm).

The data at 600°C are useful; they seem to fall into three groups: a few points at fluxes around 35-45 for flows near and below the critical flow (which, by the way still seems to be around 6 gpm), a group with flux around 15-20 for flows near and below the critical flow, and a group at fixed flow (5.92 gpm) as the flux decreased in the afternoon. The latter group shows clearly the effect of flux near critical flow as the temperature seems to begin increasing quickly above 45 (more data at higher fluxes would have been nice). The first two groups seem to form branches off the 500°C smooth curve and show that as the flux is decreased the critical flow does not seem to be strongly changed, but a maximum overtemperature for very low flows seems to occur which of course is lower for lower fluxes: 50°C for 15-20 flux and $\sim110^{\circ}$C for 35-45 flux.

May not be a function of Re, but really need 700°C data to determine this. If true, it is definitely related to the surface tension gradient with temperature. Important data at 700°C would be a.m. and p.m. runs with fixed flow and slowly changing flux then fixed flux near noon with many flows, allowing steady conditions ~10 minutes, at each.

11/9/85:

Ran according to test modified test plan for the day. This included 700°C and 5.3 gpm for about 32 minutes as flux increased from 33 to 44. The delta T increased smoothly and we could see the dry wing. We looked through the Celestron and could see the wing but not any bubbling or foaming. We could clearly see a reflection of a horizontal silica seam which deflected as it got near the wing so this is pretty convincing that the area is dry or at least there is for sure a change in film thickness. A lot of smoking during this run.

Then went to 6.2 gpm for 12 minutes, ΔT was very small or negative. However, we could still see the wing but it was not as well defined and in the Celestron the reflection of the silica seam was still deflected. At this point a logical conclusion is that the film in the wing just gets thicker as the flow increases but some sort of disturbance still exists. Went back to 5.7 gpm for 11 minutes for steady state, then 4.7 gpm then up to 8.5 for about 18 minutes (Re=1170).

Then went through the second part of the plan where we ran at 8.5, 7.5, 6.5, 6, 5.5 gpm for about 5 or 10 minutes each. Then did a shut down (check IR data) so we could clean the bottom 4 flux transducers during the period of steady insolation (it was 930° or 940°C the whole time). CU was not excessively filmy. Came back up and found that CU increased from 54-55 to maybe 58 although it was immediately exposed to smoke. Then repeated the sequence at steady flux: 7, 6.6, 6, 5.7, 5, 6 gpm.

All during these preceding tests the insolation was very steady so we should have exceptionally good stability data for 700°C.

Then we shut down to try and do something about the smoking. It appears to come a lot from the edges which must run very hot. As salt creeps over the edges it vaporizes. A more important concern is whether the presence of these edges could be causing the dry spot. They could be reradiating to the film near the edge, or conduction through the plate into the film could be causing it. We tried a long slender piece of silica inserted between the calorimeters and the edges (see video #6 near the end) and re-ran, but the silica melted within 7 minutes. It did seem that there was no smoking until it melted and that even at the 5 gpm I ran, there was not an overtemperature situation. Ran briefly at 4 gpm but the silica was pretty well gone by then. This was at 14:19 so the flux should have been only down to about 52 so this would have been a pretty good test. It would

have been worth checking the data. The video shows that we ran for about 7 minutes at this high flux and 5 gpm without smoke and without a large ΔT starting. We started this day's run at 4 gpm briefly then 5.2 for quite a while and within 20 minutes we had a ΔT-- not a bad set of data to compare it with.

The only thing worth continuing with would be to find out whether the dry spot is real or if it is an experimental artifact. About the only thing we can change at this point is the overheating of the edges and see if these influence the dry spot formation. We need a little more permanent way to shade the edges. If this decreases the smoke, we may also want to repeat some of the efficiency measurements.

If stability is improved a lot, should consider continuing the test program. Criterion is this: if flow is stable to 2.5 or 3 gpm at 50-55 flux should definitely consider the Test V--900°C then should do Test VI at lower flows and fluxes (but probably a smaller scale than the test plan calls for).

11/12/85:

Tested the edge protection George built and installed, see my notebook p. 45. Ran at 600°C, starting at 5 gpm. Sun was on/off most of the day but got some really good steady periods. Ran steadily at 5 gpm from 11:50 to 14:10 when the flux was 47 or less. Got smoke in about 90 sec, and the left ceramic piece bowed out from new Inconel strip. This is where most of the smoke came from. Smoke was definitely less, but transducers still were getting chalky. Set up Celestron to try to definitely identify source of smoke. Definitely got a hot spot, delta T of 80°C or so.

We shifted the beam about "1/2 solar disk" to the east. This evened out the flux pretty well. Hot spot still existed but was only about 54°C, flux was down to about 35.

Then went to 6 gpm for efficiency data but T20A went south (chalky flux transducers probably messed up efficiency data anyway). The dry area was definitely smaller, with less contrast--same behavior as before.

Then went back to 5 gpm to get a ΔT vs. flux curve as the flux decreased. May be pretty good data for a while because it complements the previous try at 5.92 gpm. Here, ΔT started at 74 and went down to about 60 for flux from 37 to 34.

Got a really good observation of dry area and edges during last part of this test. Observed from the side again looking for whether the edges/fins are smoking. Saw that the edges are definitely dry! Smoke must come from all of it. The salt at the junction of the 6" width and the edges appears to have a mercury-like meniscus and cannot go up the edge, so it stays very dry. See my sketch dated 11/12/85, ~14:45. The interface of the dry wing showed up clearly from closer under the tower and it may have been reflections but it seemed from the angle we looked that one could clearly see the interface was a wave and the wing was just thinner, not dry.

We did not continue the test plan any further since we still had some smoke (no better efficiency data possible) and since we still had the dry area at about the same flow as before. However, the exercise showed that: (i) the dry spot probably is not caused by the hot wings. We shaded the outboard edge of the fin (it still got to about 900°C) and even though the east side pulled away, it did not cause a hot spot. The west side stayed covered pretty good, but the hot spot was still there (check data to see quantitatively if there was a reduction). Since the same critical flow seemed to exist, it seems that this

did not change the dry spot. The only thing we could do better to test this would require a major redesign of the edges (see my sketches). (ii) The dry spot does not seem to be especially because of the higher flux in the area. We moved the beam over to make it more uniform but the dry area was still there. It could still be due to nonuniform flux, however.

At this point we considered going to 900°C overnight to test with or without flux to get a for sure turbulent flow, (Re ~10000) but the heaters would only get tank 1 to 683°C and hooking up the backup heaters would be difficult.

APPENDIX C

TYPICAL OUTPUT PLOTS
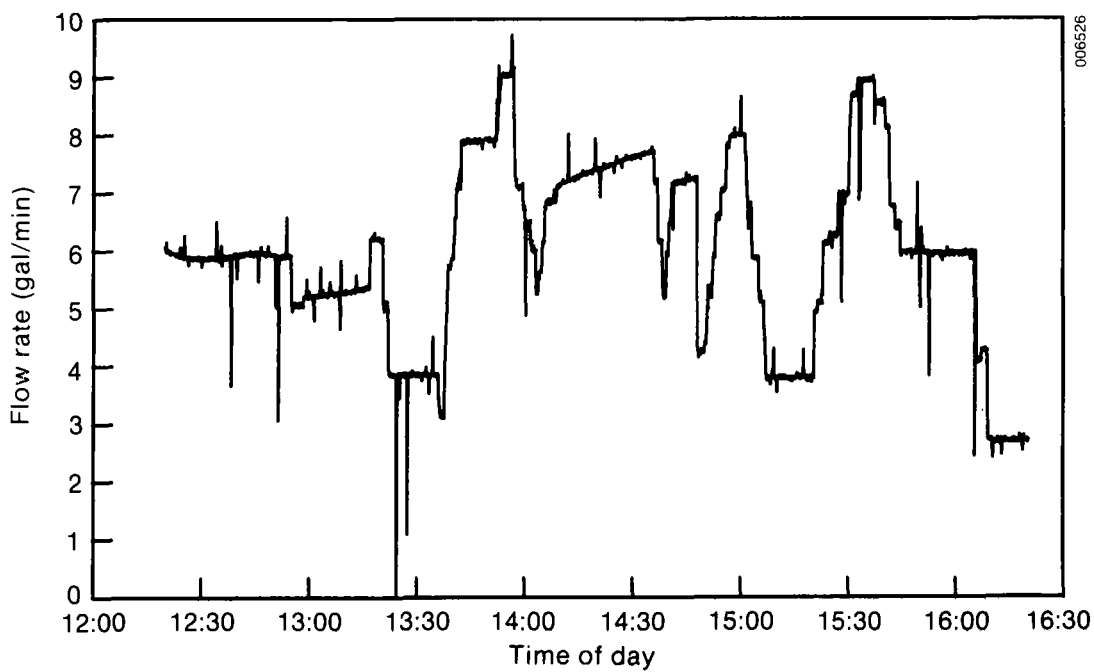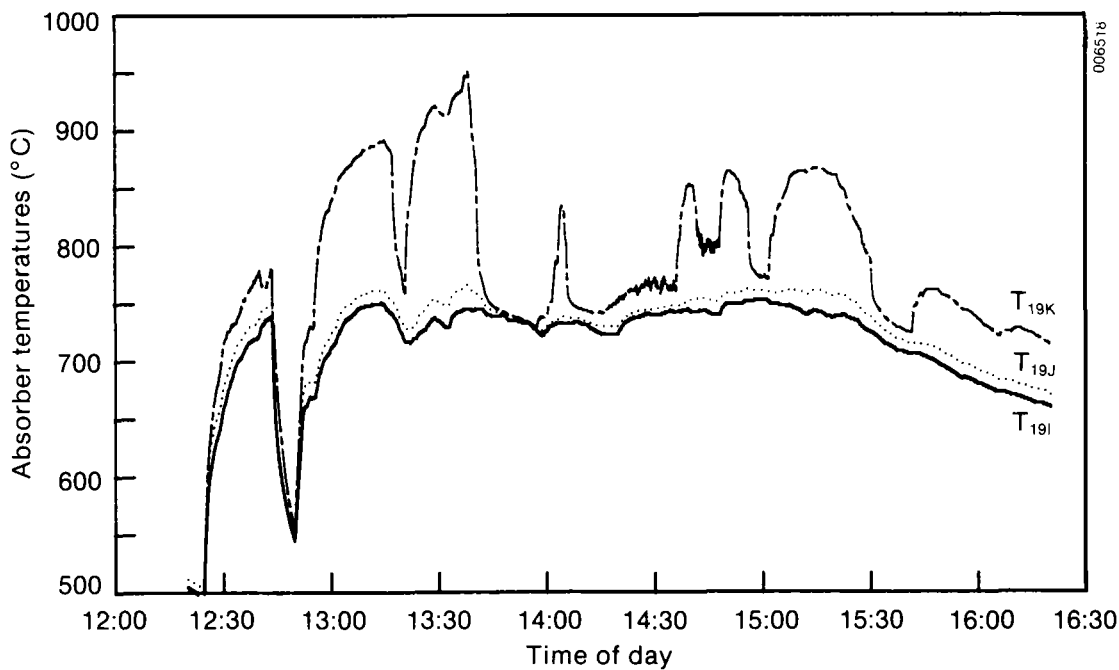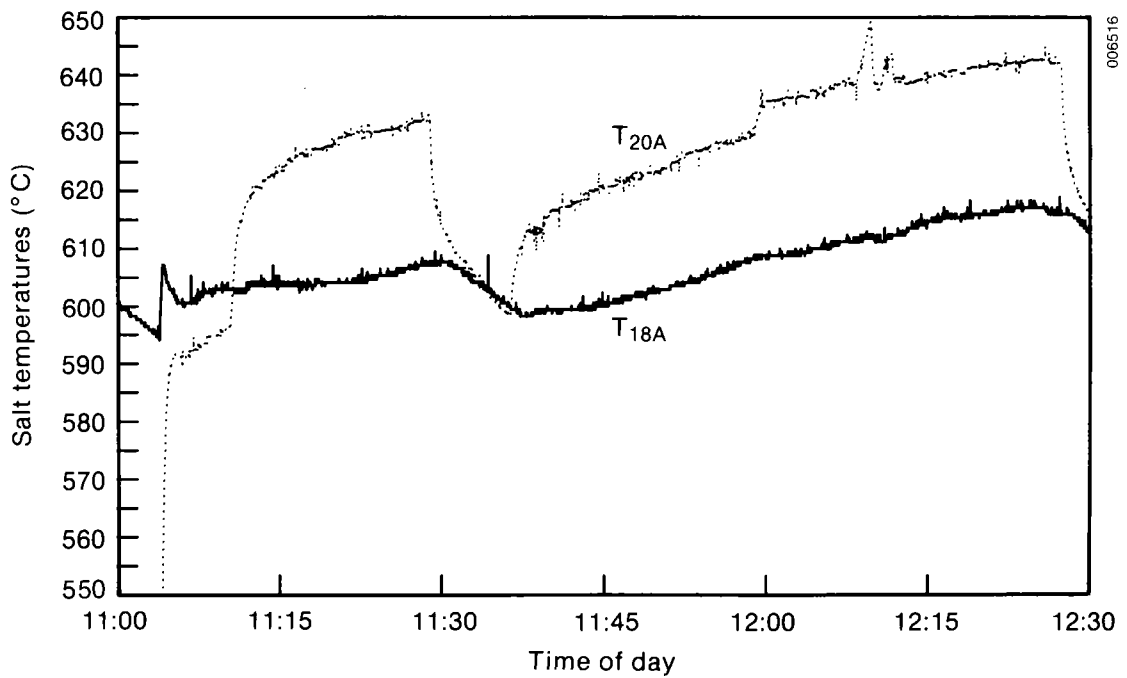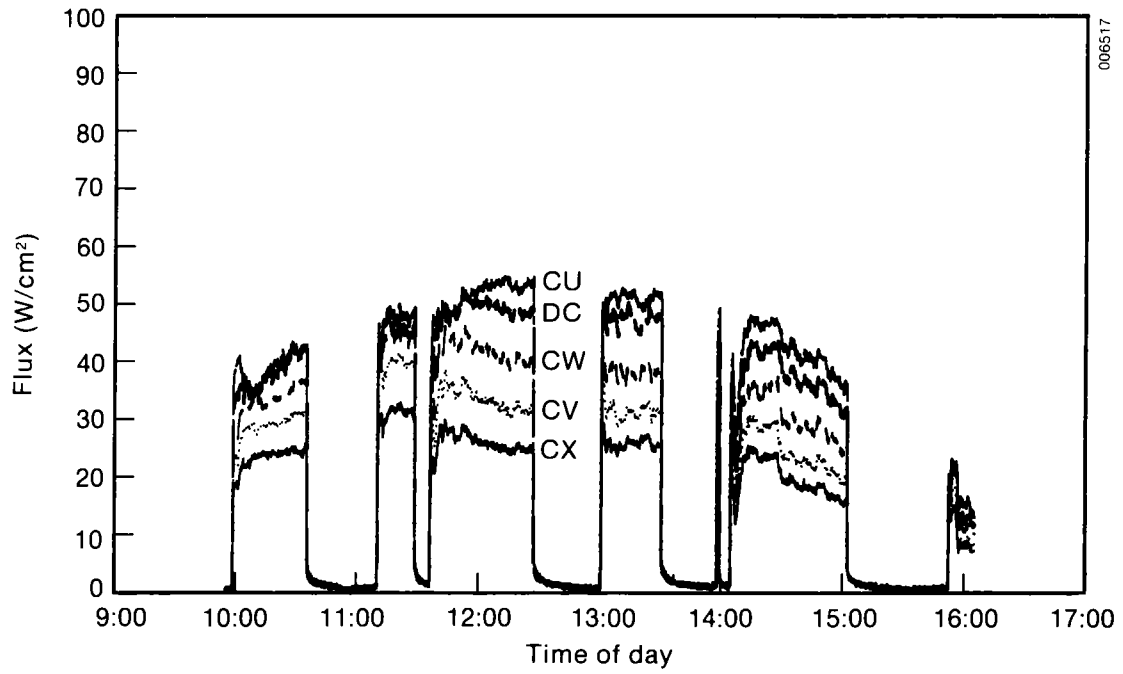
SERIO

APPENDIX D

MATERIALS DATA

D.1 Optical Properties of Slip Cast Silica/Alumina Insulation

Inter-office Memorandum   SERI ☀
                                               Solar Energy Research Institute

TO: Mark Bohn

FROM: Gary Jorgensen

DATE: September 5, 1985

SUBJECT: Optical Measurements of Slip Cast Silica/Alumina Insulation
           Materials for DAR's

Optical characterization of your sample of slip cast silica/alumina insulation material has been completed. Spectral, hemispherical reflectance measurements were made between room temperature and 900°C using our integrating sphere spectrometer. The solar weighted absorptance was computed for an air mass 1.5 spectrum. Infrared emittance measurements were made using an Everest Interscience Model 430 infrared thermometer having a spectral band pass between 7-16 μ. This surface probe was aimed at the heated sample and the emissivity setting was adjusted until agreement was obtained between the temperature read-out and a thermocouple measurement. The data are presented below.

T(°C)	α	ε
23	.057	
400		.48
500	.055	.47
600		.46
700	.055	.45
800	.057	.45
900	.059	.44
22	.054	

Note that there is little variation in solar absorptance over the temperature range 20-900°C. The measured emittances are in general agreement with data reported for Mullite (alumina silicate) by Touloukian and DeWitt (Thermal Radiative Properties of Nonmetallic Solids, Vol. 8).

cc: Dick Burrows
     Paul Schissel
     Jim Green
     K. Y. Wong
     Meir Carasso

D.2 Chemical Analysis of Salt Used in Dar Apparatus

See Figure D-1 for DTA Analysis.

Hazen Research, Inc.
4601 Indiana St. • Golden, Colo. 80403
Tel: (303) 279-4501 • Telex 45-860

DATE	August 16 1985
HRI PROJECT	009-50
HRI SERIES NO.	30705
DATE RECD.	7/29/85
CUST P.O.#	C-5-23432-1

Solar Energy Research Institute (SERI)
1617 Cole Boulevard
Denver West Office Park
Golden Colorado 80401

```
                    REPORT OF ANALYSIS
------------------------------------------------------------
SAMPLE NO. 30705-1
SAMPLE IDENTIFICATION: Salt - SERI
------------------------------------------------------------


Na as Na2CO3,%                      30.6
K  as K2CO3,%                       32.0
Li as Li2CO3,%                      33.7
```

Salt sample used in 900 deg test loop

By: *[signature]*
Robert Rostad
Laboratory Manager

D.3 Properties of Carbonate Eutectic Salt

Viscosity

$$\mu = 1.38 \times 10^{-4} e^{3986/T}$$

Source: Janz (1986) $T(K), \mu(kg/m\ s)$

Density

$$\rho = 2513 - 0.544 \times T$$

Source: Mamantov (1981) $T(K), \rho(kg/m^3)$

Thermal Conductivity

$$k = 1.98$$

. Source: Mamantov (1981) $k\ (W/m\ K)$

Surface Tension

$$\sigma = 0.287 - 6.94 \times 10^{-5} \times T$$

Source: Mamantov (1981) $T(K), \sigma(N/m)$

Contact Angle

$$\theta_o = 0^o$$

Source, Moiseev (1967)

Specific Heat

$$c_p = 1179 + 0.700 \times T$$

Source: Mamantov (1981) $T(K), c_p(W\ s/kg\ K)$
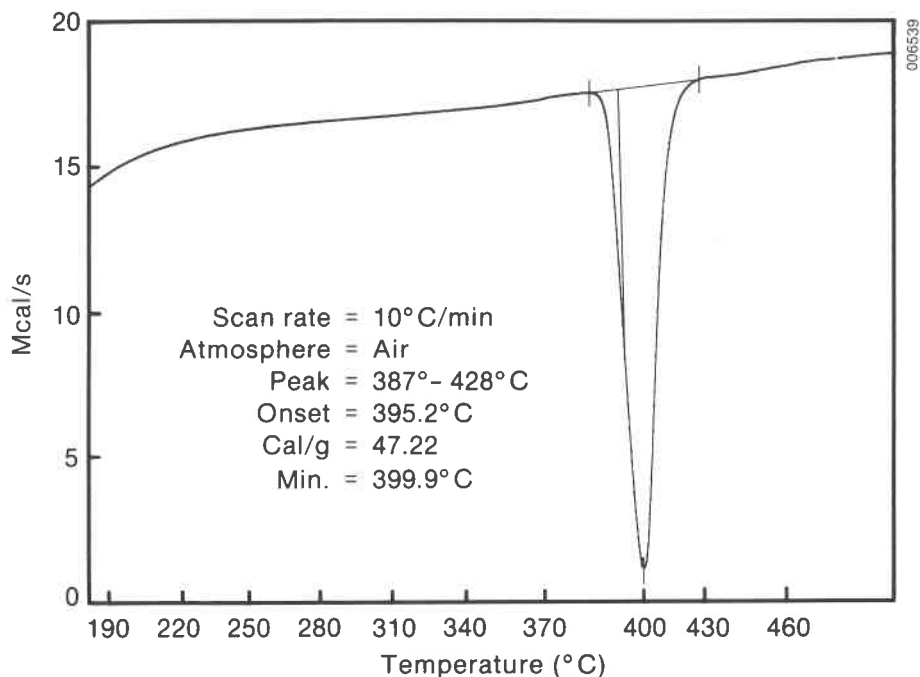
Figure D-1. DTA Analysis of Salt Used in DAR Apparatus

D.4 Stress Corrosion Cracking Tests

Metallographic examinations were performed on samples of Inconel 600 (Huntington Alloys) to assess their resistance to corrosion by a eutectic of molten carbonate salts ($NaCO_3$, KCO_3, and $LiCO_3$). Both stressed and unstressed samples were examined. The unstressed sample was taken from the wall of a manifold on an experimental test loop following about 100 hours exposure to molten salts above $500^\circ C$ over a two month period. The stressed sample was a U-bend specimen typical for stress corrosion cracking testing (ASTM G30-79). Both plastic and elastic strain were maintained in the sample during exposure to the molten salts. The sample was immersed in $650^\circ C$ molten salt for three days.

Figure D-2 shows the surface of the stressed IN600 sample at 400X magnification. There is a surface oxide layer but no evidence of intergranular corrosion. Figure D-3 shows the unstressed sample at 250X magnification. Intergranular oxidation is evident in the sample to a depth of 0.1 mm (0.004 in.). This is similar to the results reported by Coyle (1985) for unstressed IN600 immersed in $900^\circ C$ molten salt for 62 days. From these tests there is no evidence of stress contributing to the IN600 corrosion rate, and the intergranular oxidation near the surface of the alloy appears to stabilize after an initial period of growth.

Similar tests were also performed on samples of 316 and 316L stainless steels. These alloys are potential lower cost alternatives to IN600. Figure D-4 shows severe intergranular corrosion in a sample of 316 SS taken from the wall of a molten carbonate salt storage tank after 40 days exposure at $500^\circ C$. Figure D-5 shows a stressed sample of 316L stainless steel exposed to $500^\circ C$ salt for 113 hours. No intergranular attack is evident in this sample.
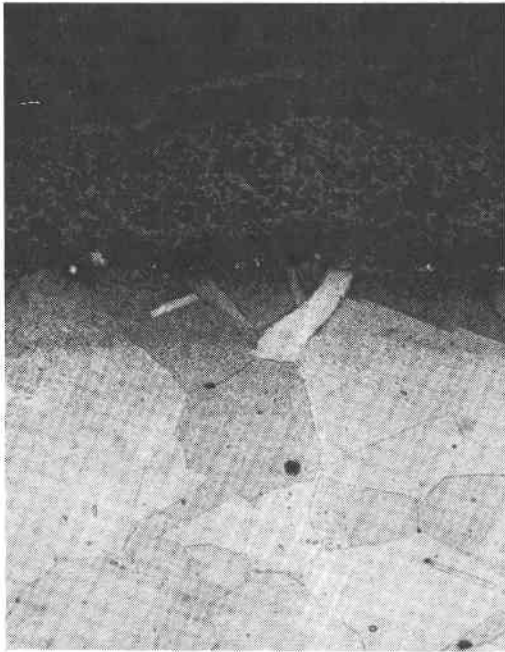
Figure D-2. Inconel 600 Stress Corrosion Cracking Sample. Three days exposure to molten carbonate salts at 650°C, 400X magnification, chemically etched
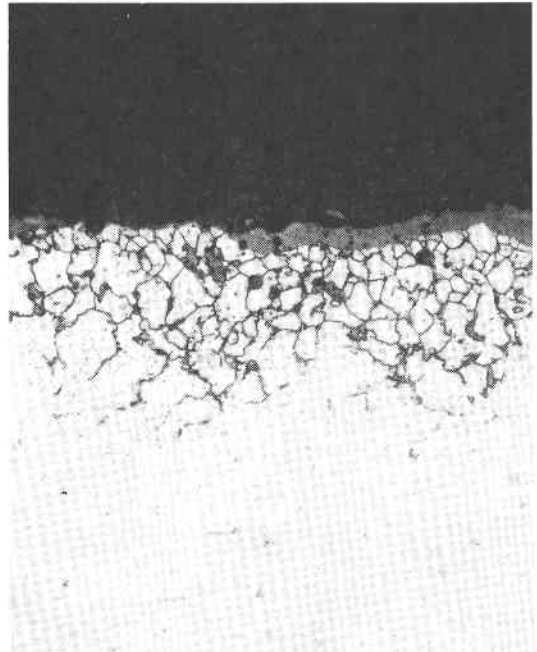
Figure D-3. 316 Stainless Steel Sample from Wall of Molten Carbonate Salt Storage Tank. 40 days exposure at 500°C, 100X magnification
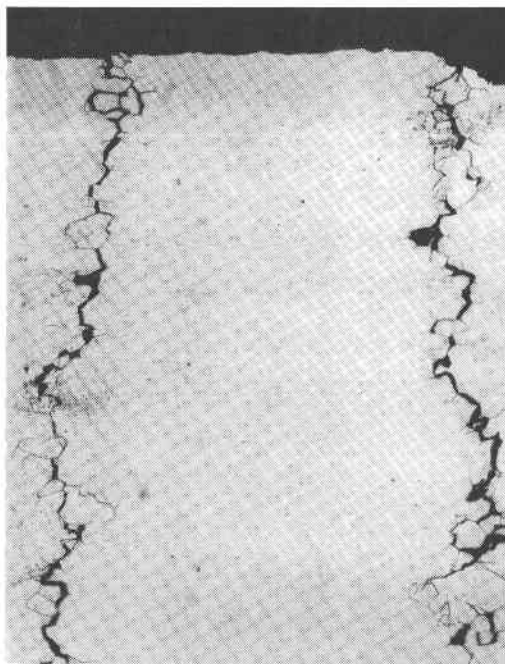
Figure D-4. Inconel 600 Sample from Wall of Inlet Manifold on Laboratory Test Loop. 100 hours exposure to molten carbonate salts above 500°C, 250X magnification, chemically etched
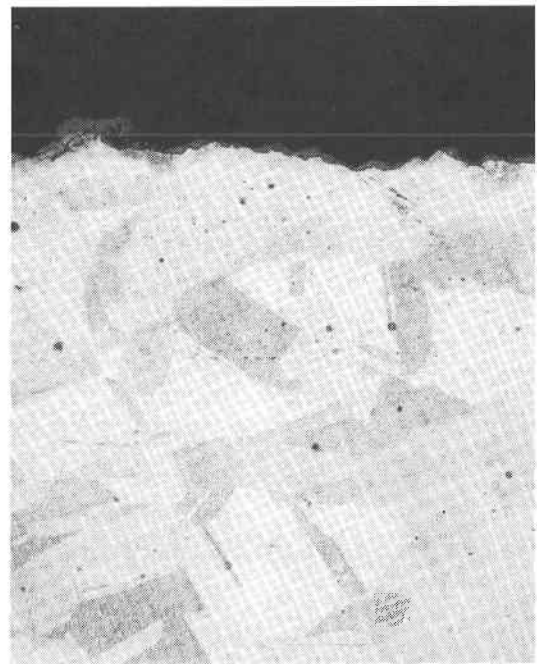
Figure D-5. 316L Stainless Steel Stress Corrosion Cracking Sample. 113 hours exposure to 500°C molten carbonate salts, 250X magnification, chemically etched

Table D-1 summarizes all the corrosion tests performed.

D.5 Salt Sample

A sample of the bulk salt was analyzed by the Materials Characterization Branch, EMSL, GTRI. By emission spectroscopy the elements described in Table D-2 were detected.

By x-ray diffraction, the compounds shown in Table D-3 were identified.

D.6 Condensate

A sample of the white condensate that formed on cool surfaces in the cavity during solar irradiation was submitted to the Materials Characterization Branch, EMSL, GTRI, for analysis. Energy dispersive x-ray analysis revealed the elements present (see Table D-4).

D.7 Reference

Coyle, R. T., T. M. Thomas, Paul Schissel, 1985 (Apr.), "Fluids and Containment Materials Compatibility Research," prepared for the Annual Solar Thermal Research Conference, Lakewood, CO, 20-22 February 1985, SERI/TP-255-2699, Golden, CO: Solar Energy Research Institute.

Table D-1.   Summary of Alloy Corrosion Testing in
            Molten Carbonate Salts

Material	Exposure Time	Temperature (°C)	Condition	Results
IN600	100 h	500	From apparatus	0.004 in. intergranular oxidation (Figure D-2)
IN600	3 days	650	Stressed	No intergranular attack (Figure D-1)
316L	40 days	500	From apparatus	No intergranular attack
316L	113 h	500	Stressed	No intergranular attack (Figure D-4)
316L	30 days	500	Stressed	No cracking visible to eye
316L	60 days	550	Stressed	No cracking visible to eye
316	37.5 h	500	Stressed	No cracking visible to eye
316	40 days	500	From apparatus	Severe intergranular corrosion
316	86 h	500	Stressed	Crack visible to eye

Table D-2. Elements Detected
in the Bulk Salt

Element	Approximate %
Sodium	Very strong
Potassium	Very strong
Lithium	Very strong
Silicon	0.02 - 0.2
Magnesium	0.2 - 1.0
Aluminum	0.01 - 0.05
Iron	0.01 - 0.1
Copper	0.005 - 0.05
Nickel	0.005 - 0.05
Calcium	0.2 - 1.0

Table D-3. Compounds Identified
in the Bulk Salt

Compound	Approximate %
Sodium carbonate	Very strong
Lithium carbonate	Very strong
Potassium carbonate	Very strong
Calcium carbonate	2
Magnesium carbonate	2
Unidentified, similar to $NaAlSiO_4$	Trace

Table D-4. Elements Present in
Salt Condensate

Element	Approximate %
Potassium	90
Sulfur	7
Chromium	1-2
Sodium	Trace
Aluminum	Trace
Silicon	Trace
Fluorine	Trace

APPENDIX E

CALIBRATION DATA

E.1 Typical Flux Transducer Calibration

```
These are the coefficients:
    C 0  =     980986E-01
    C 1  =     299817E-01
    C 2  =     281656E-06
    C 3  =     127827E-09
    C 4  =  -  208089E-13

These were the input values:
     1.        0.0000           0.0000
     2.      500.0000          15.3034
     3.     1000.0000          30.6067
     4.     1500.0000          45.9101
     5.     2000.0000          61.8511
     6.     2500.0000          77.7921
     7.     3000.0000          94.3708
     8.     3500.0000         110.9494
     9.     4000.0000         127.5281
    10.     4500.0000         144.1068
    11.     5000.0000         159.4101
    12.     5500.0000         175.9888

    Error factor CHISQR =    .920800E-07

   Test input       Test out
      0.0000          .0981
    500.0000        15.1741
   1000.0000        30.4685
   1500.0000        46.0305
   2000.0000        61.8779
   2500.0000        77.9972
   3000.0000        94.3440
   3500.0000       110.8424
   4000.0000       127.3854
   4500.0000       143.8347
   5000.0000       160.0210
   5500.0000       175.7435
```

CERTIFICATE OF CALIBRATION

"THE TEMPERATURE PEOPLE"

HY-CAL ENGINEERING
A Unit of General Signal
9650 Telstar Avenue • El Monte California 91731

"DA"

DATE 7-25-85

CUSTOMER GEORGIA TECH

P. O. NO. 004603937

INST. TYPE CALORIMETER

MODEL C-1301-AX-120-120

ABSORPTIVITY .89

CERTIFIED RECORD OF CALIBRATION
DATA ON THE INSTRUMENT DESCRIBED
ABOVE. THE DATA WAS OBTAINED IN
HY-CAL ENGINEERING'S THERMAL FLUX
FACILITY.

REFERENCE STANDARD 20045

TESTED BY

Q. C. APPROVAL

SERIAL # 134139

OUTPUT MILLIVOLTS

BTU/FT² SEC.

☒ ABSORBED   ☐ INCIDENT

10

8

6

4

2

0   20   40   60   80   100   120

111
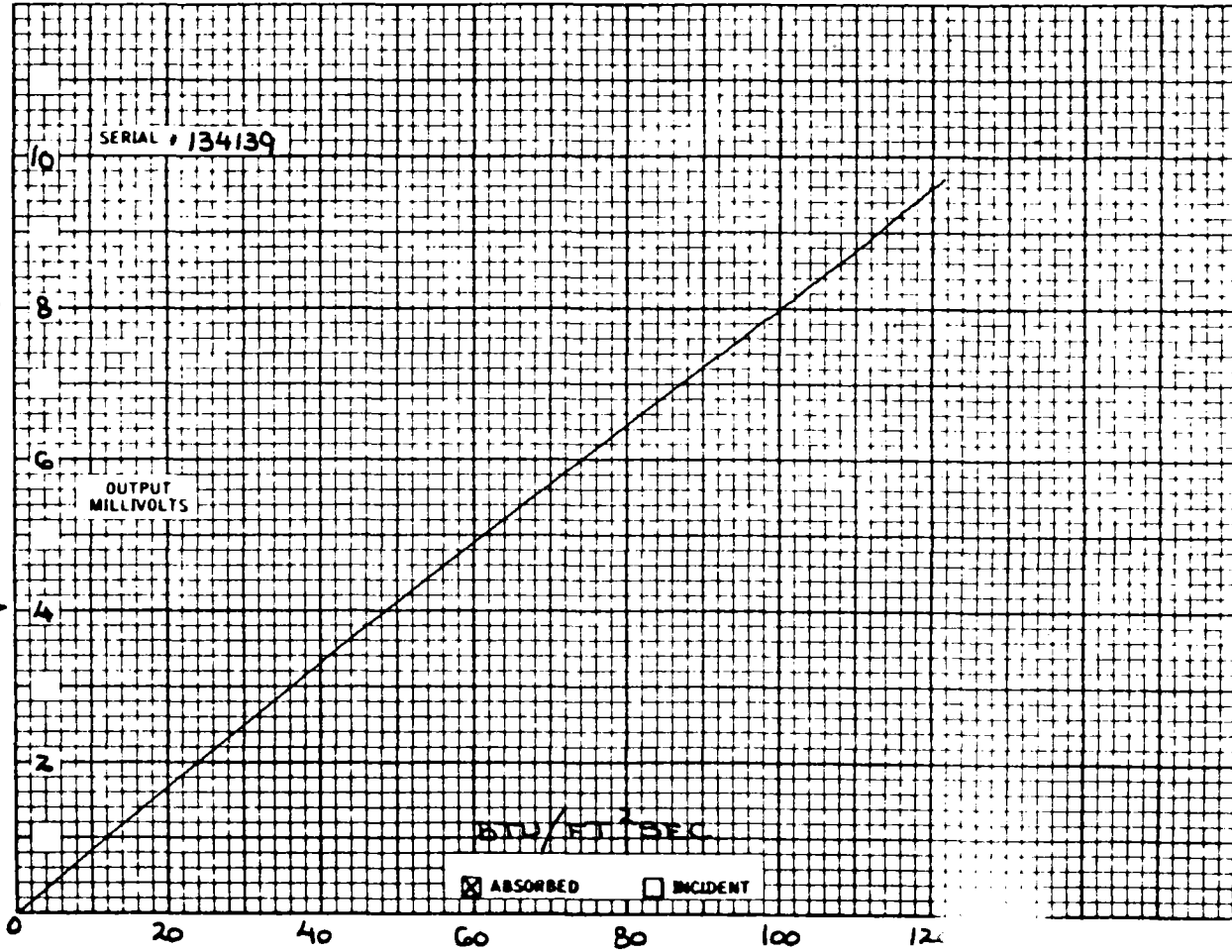
Table E-1. Flow Calibration Data, Height of Molten Salt over the Weir versus Flow Rate from Tank 2

Run No.	Salt Temperature (°C)	Salt Density (g/cm³)	Time of Day	Flow Rate from Tank 2 Based on Rate of Change of Bubbler Output, $\dot{m}_s$ (kg/min)	Flow Rate (gal/min)[a]	Height of Liquid over Weir (in. × 10³)
09145A	602.6	2.036	9:50:40 - 9:56:43	24.75	3.21	250
09145A	603.2	2.036	9:59:50 - 10:03:39	34.69	4.50	301
09145B	601.4	2.037	11:21:50 - 11:24:00	46.49	6.03	374
09145B	602.6	2.036	11:26:50 - 11:28:00	56.18	7.29	425
09145C	602.0	2.037	12:28:00 - 12:30:00	73.83	9.57	501
09145C	603.2	2.036	12:32:00 - 12:32:55	38.76	4.89	324
09145D	607.4	2.034	13:56:00 - 14:10:00	10.89	1.42	126
09145D	603.8	2.036	14:14:00 - 14:19:00	36.33	4.71	322
09165A	516.7	2.083	13:05:00 - 13:16:00	17.89	2.27	203
09165A	514.3	2.084	13:19:00 - 13:23:00	44.24	5.61	350
09165A	514.9	2.084	14:15:50 - 14:18:50	54.75	6.94	404
09175A	709.1	1.978	13:35:00 - 13:53:00	9.49	1.27	128
09175A	700.7	1.983	14:50:00 - 14:55:00	51.63	6.88	403
09205A	611.4	2.032	7:25:00 - 7:55:00	4.73	0.61	80

[a] $Q(\text{gal/min}) = 0.26417 \dfrac{m(\text{kg/min})}{\rho(\text{g/cm}^3)}$

Table E-2. Flow Calibration Data, Pump Speed versus Height of Molten Salt over the Weir

Run No.	Tank 1 Temperature (^{o}C)	Time of Day	Pump Speed (%)	Height of Liquid over Weir (in. $\times 10^3$)
09135A	601.2	16:20:20 – 16:21:50	33.66	152
09135A	601.6	16:17:30 – 16:19:10	34.98	198
09135A	601.2	16:14:40 – 16:16:20	36.96	246
09135A	601.8	16:09:10 – 16:11:40	40.29	301
09135A	601.8	16:06:00 – 16:07:40	44.46	357
09135A	604.2	15:38:00 – 15:39:40	49.31	428
09135A	601.8	16:02:20 – 16:03:40	49.76	430
09135A	601.8	15:59:20 – 16:00:40	53.73	479
09135A	602.4	15:56:10 – 15:57:40	57.07	527
09135A	603.6	15:41:40 – 15:43:10	57.40	530
09135A	602.4	15:51:50 – 15:54:20	59.43	554
09145A	607.3	08:16:50 – 08:18:50	44.39	369
09145A	604.2	08:27:10 – 08:29:30	49.24	428
09145A	601.8	08:38:30 – 08:40:40	57.28	525
09165A	515.0	10:21:30 – 10:23:40	38.33	251
09165A	515.0	10:25:20 – 10:27:30	42.50	320
09165A	515.1	10:12:50 – 10:15:00	46.84	374
09165A	515.7	10:30:00 – 10:32:30	49.43	399
09165A	516.9	10:42:00 – 10:43:40	54.72	451
09165A	516.3	10:47:00 – 10:49:30	58.45	479
09165A	517.0	10:51:30 – 10:53:10	62.52	526
09175A	695.1	15:32:20 – 15:35:40	33.81	174
09175A	695.7	15:26:00 – 15:28:40	35.51	225
09175A	696.3	15:22:40 – 15:25:00	38.43	281
09175A	696.9	15:13:20 – 15:17:20	41.37	331
09175A	694.5	15:36:40 – 15:39:20	45.93	402
09175A	693.9	15:41:20 – 15:43:40	49.59	455

SERI⚙

APPENDIX F

ANALYSIS OF EXPERIMENTAL ERRORS

F.1 Efficiency

The equation used to calculate thermal efficiency from the experimental data was

$$\eta = \frac{\dot{m}_s C_s (T_{so} - T_{si})}{\overline{q}_{in} A_{active}} .$$ (F-1)

Typical values used in this equation were

date: 11/5/85   Time: 13:50 $\dot{m}_s$ = 0.90 kg/s
                                                  C_s = 1798 W s/kg K
                                                  T_{si} = 603°C
                                                  T_{so} = 619°C
                                        $\overline{q}_{in} A_{active}$ = 29,810 W
                                                  η = 0.869

Uncertainty in each variable in Eq. F-1 was determined as shown in the following sub-sections.

F.1.1 Salt Flow, $\dot{m}_s$

Calibration of the salt flow was described in Section 2.0. We analyzed all errors involved in the calibration and in the measurement at a nominal 7 gal/min, 630°C condition. Detailed analysis of this calibration procedure included analyzing errors attributed to tank 2 diameter thermal expansion, voltmeter errors, weir depth measurement, pump speed measurement and repeatability, and bubbler instrumentation errors. The result was that the calibration errors were all bias errors and the total magnitude was ±0.19 gal/min.

A similar analysis of the actual flow measurement errors involved only pump speed measurement repeatability. This error was judged to be a precision error of ±0.166 gal/min. The calibration error and measurement error totalled 5%. An additional bias error was introduced during data analysis by assuming a constant salt density of 2050 kg/m³. This resulted in an additional error of ±2%.

The total uncertainty in the salt flow was therefore ±6%.

F.1.2 Specific Heat

Uncertainty was ±0.5% (see Appendix D.3).

F.1.3 Salt Temperature Difference

To make sure we measured the temperature differential $T_{so} - T_{si}$ accurately, we used special probes fabricated from the same thermocouple wire lot to read the salt temperature in the inlet manifold and in the drain pipe just below the absorber. (Figure F-1 shows the placement of these probes.) We checked the reliability of the probes by placing both probes mechanically connected together within the inlet manifold and reading the indicated temperature on the ACTF data system monitor. This test was performed near 590°C, and the two probes indicated 587.6°C each or 587.6°C on one and 587.0°C on the other. This difference (0.6°C) was the smallest that could be resolved by the ACTF data system.
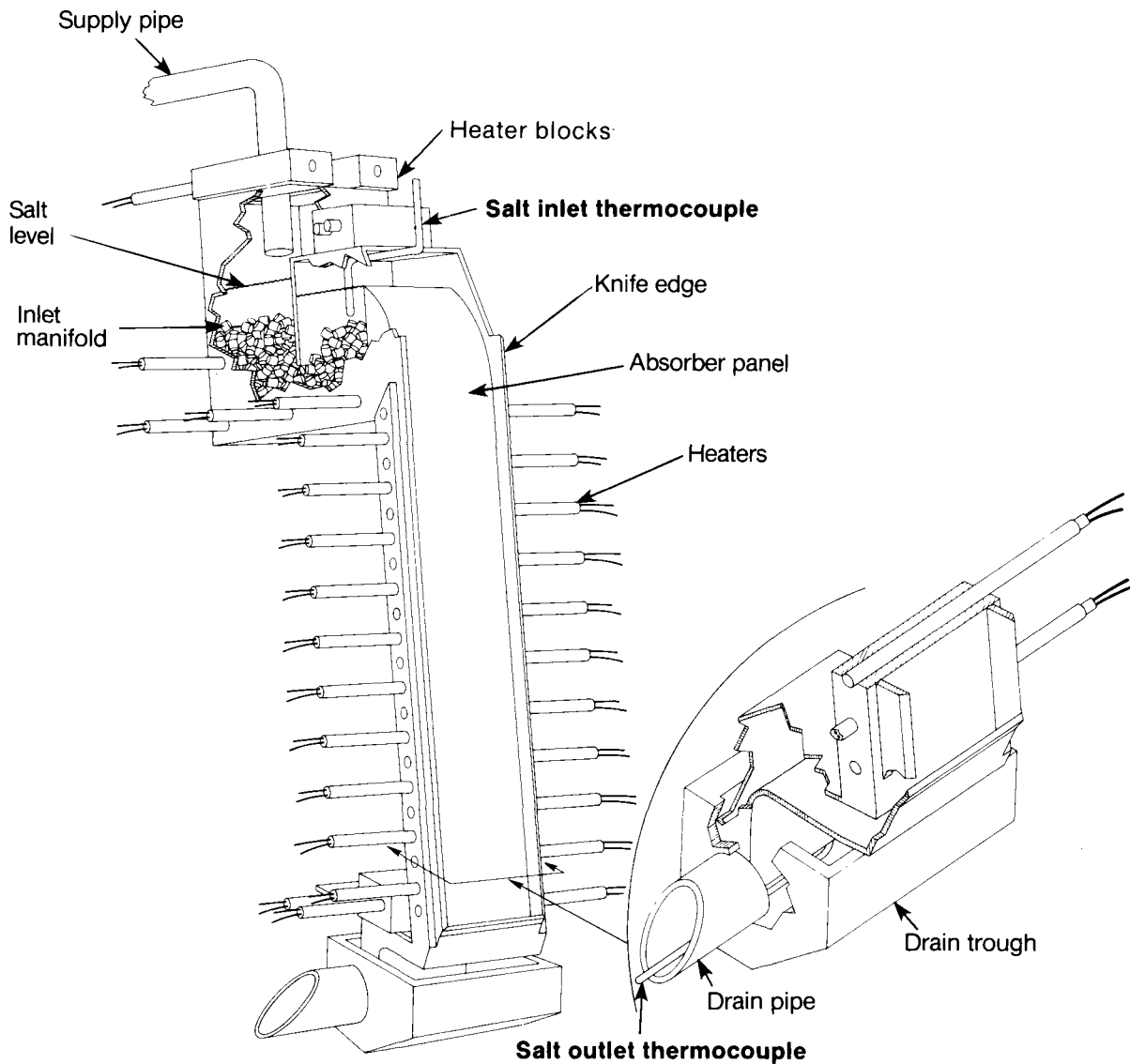
Figure F-1. Absorber Panel Showing Thermocouple Placement

A greater problem than reliable thermocouples was placing the probes correctly to ensure that they actually read the desired fluid temperature. Elements we considered include: radiation errors, immersion length, damage to the thermocouple wire caused by bending, location near trace heaters, and location near cold spots. We experimented with thermocouple placement to try to minimize these sources of error. The final placement of the probes is shown in Figure F-1.

In addition, we analyzed probe conduction errors caused by an inadequate immersion depth. Based on the outlet probe being immersed to a depth of 0.15 m (see Figure 2-3), on a forced convection coefficient (calculated from the salt velocity in the outlet pipe), and on the remainder of the probe being exposed to air at $200^\circ C$ through natural convection, we found that the probe error was extremely small. For the inlet probe we use an immersion depth of 5 cm exposure to the salt through natural convection, and the air-exposure part was treated like the inlet probe. The error here was $0.0018^\circ C$, also negligible.

Based on this discussion, it appears that the uncertainty in measuring $T_{so} - T_{si}$ was caused only by the resolution of the data system, which was less than $\pm 0.6^\circ C$ or $\pm 4.7\%$.

F.1.4 Flux Measurement

The most important errors in flux measurement arose from two sources. First, we noticed that salt decomposition led to the deposition of a fine white film on the face of the transducers (see Appendix D for an analysis of the deposit). The rate of deposition increased with salt temperature and appeared to result from the dry vertical edges on the absorber plate as depicted in Figure F-2. Since correctly operating these transducers depends on a fixed absorptance at the transducer face, this white deposit should reduce the sensitivity of the transducer.

To quantify how much the reading from transducer CU (upon which all flux measurements were based) was affected by this white coating, we cleaned it just after a shutdown and brought the system back up as quickly as possible. A flux increase was not detectable after it was brought back up, but several things helped mask this. First, about a half hour was required to shut down and clean the transducer. Thus, a short period was required after the flux was brought back up before the transducers reached steady state. Second, before the shutdown the flux transducers were fluctuating $\pm 5\%$. This was typical of the measured insolation and was probably caused by high clouds. Third, the diurnal insolation variation caused a slow change in flux, detectable even over the half-hour shutdown near solar noon. For this test it changed from 930 W/m^2 to about 940 W/m^2, about a 1% increase. Finally, within 30 seconds of bringing up the flux after the cleaning, more smoke was produced and presumably recoated the transducers.

This test and further testing and data reduction (primarily comparing measured insolation with the output of transducer CU near solar noon on clear days) lead us to believe that the reading was less than 5% below the actual flux. This error may be presumed to be a fixed-bias error.

The second source of error was suggested by researchers at Sandia National Laboratories (SNLA), Albuquerque, N. Mex., and related to the fact that the flux transducers were calibrated by the manufacturer (Hy-Cal) with an infrared heat source and the transducers are used with a solar input. To test this hypothesis we removed the flux transducer CU after testing at the ACTF and had Hy-Cal recalibrate it as received, then refurbish

Figure F-2. Cross-Sectional View of Salt Film on Absorber Showing Dry Area

Table F-1. Calibration of Flux Transducer CU

Entry	Calibration Date	State of Flux Transducer	Calibrated by	Heat Source	mV@ 100 Btu/ ft^2 s	Change from Original Calibration (%)
1	7/25/85	prior to shipment (new)	Hy-Cal	IR	8.70	–
2	2/10/86	after last ACTF test	Hy-Cal	IR	8.81	+1.0
3	2/10/86	after refurbishing	Hy-Cal	IR	8.90	+1.0
4	5/14/86	same as 3	SNLA	sun	7.87	-9.6

the transducer and calibrate again. Finally, we sent the same transducer to SNLA where it was calibrated in their solar furnace. Table F-1 gives the results, which show that operating the transducer in solar flux but using the IR calibration (as we did at the ACTF) would give readings 9.6% less than the correct flux. Thus, this error may be considered a fixed bias of -9.6%. Adding these two bias errors together, we see that the uncertainty in the flux measurement was -14.6%.

The final input to Eq. F-1 was the area to be multiplied by the incident flux. Although the active area of the absorber was described as a nominal 15.2 x 61 cm, the actual active width of the absorber panel is open to discussion. Even without the additional edge height as described in Section 2.3, the absorber edge design provides a potential additional absorption area beyond the nominal 15.2 cm width. Adding the edge height increased this absorption further. In particular, if the entire exposed face of the absorber contributed with 100% effectiveness to the temperature rise of the salt flowing on the plate, the effective width should be 28.6 cm not 15.2 cm, nearly a 90% increase. We are neglecting the contribution of these edges since, as discussed in Section 6.4, the salt did not wet these surfaces at all and therefore did not play a role in the salt film absorption.

A summary of all the errors in η is given in Table F-2.

Table F-2. Summary of Errors, Efficiency Measurement

	Bias		Precision
Mass flow	±0.027	(flow calibration/ measurement)	±0.024
	±0.02	(density error)	
Specific heat	±0.005		--
Temperature difference	--		±0.037
Flux	+0.05	(deposit on transducers)	--
	+0.096	(solar vs. IR calibration)	

These errors were combined using the standard method described in *Measurement Uncertainty Handbook**. This procedure gives an uncertainty on efficiency = 15.8%, 7.8%.

F.2 Heat Transfer Coefficient

The equations used to calculate the dimensionless heat transfer coefficient from the experimental data were

$$Nu = \frac{h}{k}(\frac{v^2}{g})^{1/3} \qquad (F-2)$$

$$h = \frac{(1-\rho_s)q(x)}{T_a(x) - T_s(x)} \qquad (F-3)$$

Uncertainty in the solar-weighted reflectance ρ_s was ±1% (bias) according to Jorgenson (1985). Uncertainty in the flux measurement was discussed in Section F.1. Uncertainty in the absorber and salt temperature was estimated to be ±3°C (bias), the standard ASTM error for 24-gauge type K thermocouple. We analyzed the error in T_a resulting from inserting it in the absorber panel and found it to be negligible. We estimated an additional precision error in $T_s(x)$ to be ±10% of $(T_{so} - T_{si})$ because $T_s(x)$ was an interpolation between these two terminal salt temperatures. Thus the precision in $T_s(x)$ was ±1.8°C. Uncertainty on absolute viscosity, according to Janz (1986), is ±3% (bias) and on density, according to Wein and Janz (1965), is ±1% (bias). Since thermal conductivity has not been determined from experimental data, uncertainty in k is unknown. These errors are summarized in Table F-3.

These errors were combined using the standard method described in *Measurement Uncertainty Handbook.** This procedure gives the uncertainty in the dimensionless heat transfer coefficient of +8.4%, -14.1%.

Table F-3. Summary of Errors, Heat Transfer Measurement

Parameters	Bias	Precision
Solar reflectance $(1-\rho_s)$	±0.0005	--
Flux	-0.05 -0.096	--
Absorber temperature	±0.04	--
Salt temperature	±0.04	±0.024
Viscosity	±0.02	
Density	±0.007	--
Thermal conductivity	?	--

*Abernathy, R. B., et al., 1980, *Measurement Uncertainty Handbook*, revised, Research Triangle Park, NC: Instrument Society of America.

Table G-1. Experimental Data Used for Analyzing Film Stability

date	time	incident flux	salt flow	salt in	salt out	T19A	T19B	T19D	T19F	T19H	T19I
		W/cm^2	gpm	C	C	C	C	C	C	C	C
11/5	13:50	40.5	7.0	603	619	634	670	719	713	763	756.0
11/5	13:56	41.8	7.0	604	621	636	674	729	721	776	771.0
11/5	14:03	42.8	6.1	604	624	637	675	731	725	779	770.0
11/5	14:08	42.3	5.0	603	625	634	674	745	729	779	768.0
11/6	11:57	52.0	8.1	607	629	644	692	753	758	829	813.0
11/6	12:05	53.0	6.2	610	637	648	696	758	766	832	821.0
11/6	14:26	47.1	7.2	610	631	645	687	741	734	798	787.0
11/6	14:30	41.8	5.9	609	631	642	683	736	734	795	779.0
11/8	13:35	57.2	3.8	508	549	556	607	694	740	765	742.0
11/8	13:51	54.0	7.9	513	533	560	610	688	692	746	733.0
11/8	15:00	40.2	8.0	602	619	634	668	716	723	773	753.0
11/8	15:03	38.9	6.8	604	620	632	668	713	722	769	749.0
11/8	15:15	34.7	3.8	605	638	631	663	706	758	767	743.0
11/8	15:36	27.0	9.0	608	624	629	654	686	692	733	711.0
11/8	15:45	25.3	6.0	604	624	626	650	681	691	724	703.0
11/9	10:19	37.7	5.3	684	706	710	740	781	793	831	801.0
11/9	10:30	40.0	5.3	697	717	723	758	797	817	851	821.0
11/9	10:36	42.3	5.3	692	721	723	758	798	822	856	824.0
11/9	10:42	43.5	5.3	687	717	718	780	797	820	856	823.0
11/9	11:39	45.0	8.5	705	728	742	784	839	839	899	855.0
11/9	11:47	49.1	7.5	703	730	743	787	849	847	906	861.0
11/9	11:54	45.3	6.6	703	743	740	785	847	861	906	868.0
11/9	12:01	48.7	6.0	697	745	742	787	849	874	917	879.0
11/9	12:07	50.0	5.4	699	742	739	786	849	889	924	878.0
11/9	13:01	55.0	6.7	710	737	745	790	850	850	912	864.0
11/9	13:05	57.3	5.7	708	737	747	793	854	864	914	866.0
11/9	13:12	53.5	5.1	706	734	743	784	838	889	901	856.0
11/9	13:16	52.7	5.9	705	735	745	790	852	886	913	871.0

Table G-1. Experimental Data Used for Analyzing Film Stability (Concluded)

date	time	T19J	T19K	average salt temp	salt viscosit	surface tension	salt th cond.	Re	(Tf-Tsi) ------ (Td-Tsi)	Re	(Tk-Tso) ------- (Ti-Tso)
		C	C	C	kg/ms	N/m	W/mK	-	C	-	
11/5	13:50	762	789	611	.009	.226	1.98	627	.948	627	1.24
11/5	13:56	776	776	613	.009	.226	1.98	632	.936	632	1.03
11/5	14:03	777	844	614	.009	.225	1.98	555	.953	555	1.51
11/5	14:08	778	875	614	.009	.225	1.98	458	.887	458	1.75
11/6	11:57	819	823	618	.009	.225	1.98	758	1.034	758	1.05
11/6	12:05	832	935	624	.009	.225	1.98	599	1.054	599	1.62
11/6	14:26	796	815	621	.009	.225	1.98	682	.947	682	1.18
11/6	14:30	790	876	620	.009	.225	1.98	556	.984	556	1.66
11/8	13:35	764	933	529	.015	.231	1.98	218	1.247	218	1.99
11/8	13:51	733	738	523	.016	.232	1.98	433	1.023	433	1.03
11/8	15:00	759	773	611	.009	.226	1.98	720	1.061	720	1.15
11/8	15:03	757	809	612	.009	.226	1.98	618	1.083	618	1.47
11/8	15:15	759	866	622	.009	.225	1.98	363	1.515	363	2.17
11/8	15:36	720	733	616	.009	.225	1.98	833	1.077	833	1.25
11/8	15:45	715	759	614	.009	.225	1.98	550	1.130	550	1.71
11/9	10:19	827	830	695	.006	.220	1.98	708	1.124	708	1.31
11/9	10:30	849	857	707	.006	.219	1.98	744	1.200	744	1.35
11/9	10:36	850	875	707	.006	.219	1.98	743	1.226	743	1.50
11/9	10:42	850	896	702	.006	.219	1.98	729	1.209	729	1.69
11/9	11:39	892	864	717	.006	.218	1.98	1241	1.000	1241	1.07
11/9	11:47	902	855	717	.006	.218	1.98	1095	.986	1095	.95
11/9	11:54	900	900	723	.006	.218	1.98	989	1.097	989	1.26
11/9	12:01	913	939	721	.006	.218	1.98	892	1.164	892	1.45
11/9	12:07	916	1008	721	.006	.218	1.98	801	1.267	801	1.96
11/9	13:01	904	899	724	.006	.218	1.98	1006	1.000	1006	1.28
11/9	13:05	906	929	723	.006	.218	1.98	853	1.068	853	1.49
11/9	13:12	896	975	720	.006	.218	1.98	755	1.386	755	1.98
11/9	13:16	912	1004	720	.006	.218	1.98	874	1.231	874	1.98

Table G-2. Experimental Data Used for Analyzing Heat Transfer and Efficiency

date	time	incident flux	salt flow	salt in	salt out	T19A	T19B	T19D	T19F	T19H	T19I
		W/cm^2	gpm	C	C	C	C	C	C	C	C
11/5	13:50	40.50	6.95	603	619	634	670	719	713	763	756
11/5	13:56	41.80	6.95	604	621	636	674	729	721	776	771
11/5	14:03	42.80	6.05	604	624	637	675	731	725	779	770
11/5	14:08	42.30	5.00	603	625	634	674	745	729	779	768
11/6	11:50	49.80	8.05	603	623	640	686	741	748	805	800
11/6	11:57	52.00	8.10	607	629	644	692	753	758	829	813
11/6	12:21	52.30	7.00	616	642	656	705	764	771	840	837
11/6	14:26	47.10	7.20	610	631	645	687	741	734	798	787
11/8	13:51	54.00	7.90	513	533	560	610	688	692	746	733
11/8	14:15	49.40	7.30	527	546	565	612	686	686	739	723
11/8	15:36	27.00	9.00	608	624	629	654	686	692	733	711
11/9	10:19	37.70	5.30	684	706	710	740	781	793	831	801
11/9	10:30	40.00	5.30	697	717	723	758	797	817	851	821
11/9	10:36	42.30	5.30	692	721	723	758	798	822	856	824
11/9	10:42	43.50	5.30	687	717	718	780	797	820	856	823
11/9	11:39	45.00	8.50	705	728	742	784	839	839	899	855
11/9	11:47	49.10	7.50	703	730	743	787	849	847	906	861
11/9	11:54	45.30	6.60	703	743	740	785	847	861	906	868
11/9	12:01	48.70	6.00	697	745	742	787	849	874	917	879
11/9	12:49	56.20	7.00	696	723	733	776	830	830	887	841
11/9	13:01	55.00	6.70	710	737	745	790	350	850	912	864
11/9	13:05	57.30	5.70	708	737	747	793	854	864	914	866
11/9	13:12	53.50	5.10	706	734	743	784	838	889	901	856
11/9	13:16	52.70	5.90	705	735	745	790	852	886	913	871

Table G-2. Experimental Data Used for Analyzing Heat Transfer and Efficiency (Continued)

date	time	T19J	T19K	average salt temp	salt viscosit	salt sp. heat	salt th cond.	incident energy	absorbed energy	efficie
		C	C	C	kg/ms	Ws/kg K	W/mK	kW	kW	-
11/5	13:50	762	789	611	.0094	1798	1.98	29.81	25.86	.87
11/5	13:56	776	776	613	.0094	1799	1.98	30.76	27.49	.89
11/5	14:03	777	844	614	.0093	1800	1.98	31.50	28.17	.89
11/5	14:08	778	875	614	.0093	1800	1.98	31.13	25.61	.89
11/6	11:50	805	810	613	.0093	1799	1.98	36.65	37.47	(a)
11/6	11:57	819	823	618	.0091	1803	1.98	38.27	41.56	
11/6	12:21	840	853	629	.0086	1810	1.98	38.49	42.63	
11/6	14:26	796	815	621	.0090	1804	1.98	34.67	35.30	
11/8	13:51	733	738	523	.0155	1736	1.98	39.74	35.49	.89
11/8	14:15	729	743	537	.0143	1746	1.98	36.36	31.32	.86
11/8	15:36	720	733	616	.0092	1801	1.98	19.87	33.56	
11/9	10:19	827	830	695	.0064	1857	1.98	27.75	28.01	
11/9	10:30	849	857	707	.0061	1865	1.98	29.44	25.57	
11/9	10:36	850	875	707	.0061	1865	1.98	31.13	37.08	
11/9	10:42	850	896	702	.0062	1862	1.98	32.02	38.29	
11/9	11:39	892	864	717	.0058	1872	1.98	33.12	47.34	
11/9	11:47	902	855	717	.0058	1872	1.98	36.14	49.03	
11/9	11:54	900	900	723	.0057	1876	1.98	33.34	64.08	
11/9	12:01	913	939	721	.0057	1875	1.98	35.84	69.85	
11/9	12:49	881	869	710	.0060	1867	1.98	41.36	45.64	
11/9	13:01	904	899	724	.0057	1877	1.98	40.48	43.92	
11/9	13:05	906	929	723	.0057	1876	1.98	42.17	40.11	
11/9	13:12	896	975	720	.0057	1874	1.98	39.38	34.62	
11/9	13:16	912	1008	720	.0057	1874	1.98	38.79	42.91	

---

[a]Deleted efficiency values represent data points that were judged to be too unsteady for meaningful results.

Table G-2. **Experimental Data Used for Analyzing Heat Transfer and Efficiency (Concluded)**

date	time	ha	hb	hdf	hh	hijk	Pr	Re	Nu ave
		W/m^2 C	W/m^2 C	W/m^2 C	W/m^2 C	W/m^2 C	-	-	-
11/5	13:50	7496	3737	2643	2482	2485	8.56	627	.162
11/5	13:56	7515	3696	2546	2381	2507	8.50	632	.163
11/5	14:03	7560	3768	2567	2424	2273	8.44	555	.147
11/5	14:08	8103	3751	2350	2402	2133	8.44	458	.138
11/6	11:50	7756	3711	2595	2415	2517	8.48	734	.163
11/6	11:57	8176	3802	2589	2295	2523	8.28	758	.161
11/6	12:21	7682	3683	2578	2317	2380	7.88	691	.146
11/6	14:26	7836	3815	2751	2478	2566	8.19	682	.162
11/8	13:51	6490	3413	2223	2248	2468	13.61	433	.225
11/8	14:15	7438	3579	2270	2267	2451	12.59	435	.211
11/8	15:36	7708	3732	2518	2163	2525	8.36	833	.162
11/9	10:19	8828	4332	2784	2612	3010	5.98	708	.151
11/9	10:30	9235	4148	2728	2605	2907	5.71	744	.141
11/9	10:36	8447	4176	2765	2684	2957	5.72	743	.144
11/9	10:42	8740	2955	2763	2680	2814	5.82	729	.139
11/9	11:39	7109	3569	2508	2306	2879	5.51	1241	.136
11/9	11:47	7244	3691	2545	2432	3117	5.51	1095	.148
11/9	11:54	7793	3647	2334	2360	2759	5.38	989	.129
11/9	12:01	6869	3617	2331	2382	2617	5.42	892	.123
11/9	12:49	9053	4455	3173	2978	3617	5.66	993	.175
11/9	13:01	9437	4360	2961	2739	3285	5.37	1006	.153
11/9	13:05	8778	4279	2859	2813	3185	5.39	853	.149
11/9	13:12	8660	4374	2544	2781	2785	5.44	755	.131
11/9	13:16	7881	3948	2412	2570	2460	5.44	874	.116

SELECTED DISTRIBUTION LIST

Acurex Solar Corporation
485 Clyde Ave.
Mt. View, CA 94042
Mr. Don Duffy

Allied Chemical Company
P.O. Box 1021R
Morristown, NJ 07960
Mr. Robert Armburst

Arizona Public Service Company
P.O. Box 21666
Phoenix, AZ 85036
Mr. Eric Weber

Babcock and Wilcox
91 Sterling Ave.
Barberton, OH 44203
Mr. Paul Elsbree

Black & Veatch Consulting Engineers
Advanced Tech. Projects
1500 Meadow Lake Parkway
Kansas City, MO 64114
Dr. Charles Grosskreutz

Dr. Melvin Bowman
Consultant
360 Andanada
Los Alamos, NM 87544

Brookhaven National Laboratory
Dept. of Applied Sciences
Bldg. 701
Upton, NY 11973
Dr. William Wilhelm

Dr. Tom Brumleve
Consultant
1512 N. Gate Road
Walnut Creek, CA 94598

Burns & McDonnell
P.O. Box 173
Kansas City, MO 64141
Mr. Peter Steitz

Combustion Engineering
900 Long Ridge Rd.
P.O. Box 9308
Stamford, CT 06904
Jerry Kandas

DFVLR
Fur Technische Thermodynamic
Farschungsbereich Energetik
7000 Stuttgart 80
F.R.G.
Dr. Reiner Köhne

El Paso Electric
P.O. Box 982
El Paso, TX 79960
Mr. James E. Brown

Electric Power Research Institute
P.O. Box 10412
Palo Alto, CA 94303
Dr. E. A. DeMeo

Entech, Inc.
P.O. Box 612246
DFW Airport, TX 75261
Mr. Walter Hesse

Farmland Industries
P.O. Box 69
Lawrence, KS 66044
Mr. John Prijatel

Flow Industries
P.O. Box 806
La Canada, CA 91011
Mr. John Becker

Foster Wheeler Solar Development Corp.
12 Peach Tree Hill Road
Livingston, NJ 07039
Mr. Robert J. Zoschak
Dr. S. F. Wu

Georgia Institute of Technology
Atlanta, GA 30332
Mr. Bob Cassanova

Hughes Aircraft Company
Electric Optical Data Systems Group
El Segundo, CA 90245
Dr. Frank Ludwig

LaJet Energy Company
P.O. Box 3599
Abilene, TX 79604
Mr. Monte McGlaun

3M Corporation
3M Center Buildings, 207-1W-08
St. Paul, MN 55101
Mr. Burton A. Benson

Martin Marietta
P.O. Box 179
Denver, CO 80201
Mr. Tom Tracey

McDonnell Douglas Astronautics Co.
5301 Bolsa Ave.
Huntington Beach, CA 92647
Mr. Jim Royan

NASA Lewis Research Center
21000 Brookpark Road
Cleveland, OH 44135
Dr. Dennis Flood

National Bureau of Standards
Building 221, Room 252
Gaithersburg, MD 20899
Mr. Joseph Richmond

Olin Corporation
315 Knotter Drive
Cheshire, CT 06410-0586
Mr. Jack Rickly

Power Kinetics, Inc.
1223 Peoples Ave.
Troy, NY 12180
Mr. Bob Rogers

Purdue University
Mechanical Engineering Dept.
West Lafayette, IN 47907
Prof. Raymond Viskanta

Rockwell International
8900 De Soto Ave.
Canoga Park, CA 91304
Mr. Tom Springer

SPECO
P.O. Box 91
Morrison, CO 80465
Mr. Tibor Buna

Sanders Associates
95 Canal Street
Nashua, NH 03010
Dr. Daniel J. Shine

Sandia National Laboratories
Solar Energy Department 6220
P.O. Box 5800
Albuquerque, NM 87185
Mr. John Otts

Sandia National Laboratories
Solar Department 8453
Livermore, CA 94550
Dr. J. C. Swearengen

Sandia National Laboratories
Solar Tech. Program Integration Office
Division 8454
Livermore, CA 94550
Dr. Joe Iannucci

Science Applications, Inc.
10401 Roselle Street
San Diego, CA 92121
Dr. Barry Butler

Solar Kinetics, Inc.
P.O. Box 47045
Dallas, TX 75247
Mr. Gus Hutchison

Southern California Edison
2244 Walnut Grove Avenue
Rosemead, CA 91770
Mr. Joe Reeves

Southern Research Institute
2000 9th Avenue South
P.O. Box 53305
Birmingham, AL 35255
Dr. John W. Gibson

Southwest Research Institute
6220 Culebra Road
San Antonio, TX 78238
Mr. Danny M. Deffenbaugh

Universität Stuttgart
Pfaffenwaldring 6
D-7000 Stuttgart 80
F.R.G.
Dr.-Ing. Erich W. P. Hahne

University of Arizona
Dept. of Electrical Engineering
Tucson, AZ 85721
Dr. Roger C. Jones

University of Arizona
College of Engineering
Tucson, AZ 85721
Dr. Kumar Ramohalli

University of California
Lawrence Berkeley Laboratory
1 Cyclotron Road
Berkeley, CA 94720
Dr. Arlan Hunt

University of California
Dept. of Mechanical Engineering
Berkeley, California 94720
Prof. R. Seban

University of Hawaii at Manoa
Hawaii Natural Energy Institute
Holmes Hall Room 246
2540 Dole Street
Honolulu, HI 96822
Dr. Mike Antal

University of Houston
4800 Calhoun
106 SPA Building
Houston, TX 77004
Dr. Alvin Hildebrandt

University of Houston
Department of Chemical Engineering
4800 Calhoun
Houston, TX 77004
Prof. A. E. Dukler

University of Illinois
Dept. of Mechanical and Industrial
  Engineering
1206 W. Green Street
Urbana, IL 61801
Dr. Art Clausing

University of Kansas Center for
  Research
2291 Irving Hill Drive
Lawrence, KS 66045
Mr. David Martin

University of Minnesota
Dept. of Mechanical Engineering
Minneapolis, MN 55455
Dr. Edward Fletcher

University of New Hampshire and
College of Engineering and Physical
  Sciences
Kingsbury Hall - 260
Durham, NH 03824
Dr. V. K. Mathur

University of Utah
Department of Mechanical and
Industrial Engineering
MEB3008
Salt Lake City, UT 84112
Prof. Robert Boehm

Document Control Page	1. SERI Report No. SERI/TR-252-2884	2. NTIS Accession No.	3. Recipient's Accession No.
4. Title and Subtitle Direct Absorption Receiver Experiments and Concept Feasibility			5. Publication Date October 1986
			6.
7. Author(s) O. D. Asbell, C. T. Brown, M. S. Bohn, H. J. Green, G. Yeagle, J. Siebarth			8. Performing Organization Rept. No.
9. Performing Organization Name and Address Solar Energy Research Institute A Division of Midwest Research Institute 1617 Cole Boulevard Golden, Colorado 80401-3393			10. Project/Task/Work Unit No. 5112.21 & 5122.21
			11. Contract (C) or Grant (G) No. (C) (G)
12. Sponsoring Organization Name and Address			13. Type of Report & Period Covered Technical Report
			14.
15. Supplementary Notes			

16. Abstract (Limit: 200 words)

This report presents the results of recent experiments on the direct absorption receiver (DAR) concept using molten salt as the working fluid. These experiments were aimed at determining whether the DAR concept is technically feasible and were carried out at the Advanced Components Test Facility, Atlanta, Ga. Results are based on several days of operating with solar flux ranging up to 50 W/cm^2 and also on a numerical model capable of predicting the thermal performance of the DAR salt film. Issues relating to thermal efficiency, absorber-to-salt heat transfer, and salt film stability are addressed.

17. Document Analysis

a. Descriptors Advanced Components Test Facility ; Heat Transfer ; Molten Salts ; Solar Flux ; Solar Receivers ; Thermal Efficiency

b. Identifiers/Open-Ended Terms

c. UC Categories

62a

18. Availability Statement National Technical Information Service U.S. Department of Commerce 5285 Port Royal Road Springfield, Virginia 22161	19. No. of Pages 143
	20. Price A07